FINAL REPORT

SECA Coal-Based Systems – LGFCS

May 7, 2014

WORK PERFORMED UNDER AGREEMENT

DE-FE0000303

(period of performance Sept. 1, 2009 through Jan. 30, 2014)

SUBMITTED BY

LG Fuel Cell Systems Inc.
6065 Strip Ave. NW
North Canton, OH 44720

PRINCIPAL INVESTIGATOR

Richard Goettler
330-491-4821 (phone)
330-491-4808 (fax)
richard.goettler@lgfcs.com

SUBMITTED TO

U. S. Department of Energy
National Energy Technology Laboratory

Patcharin Burke
Patcharin.Burke@netl.doe.gov

Disclaimer:

TABLE OF CONTENTS

1.0 EXECUTIVE SUMMARY

LGFCS is developing an integrated planar (IP) SOFC technology for mega-watt scale power generation including the potential for use in highly efficient, economically competitive central generation power plant facilities fuel by coal synthesis gas. This Department of Energy Solid-State Energy Conversion Alliance (SECA) program has been aimed at achieving further cell and stack technical advancements and assessing the readiness of the LGFCS SOFC stack technology to be scaled to larger-scale demonstrations as a path to commercialization. Significant progress was achieved in reducing to practice a higher performance and lower cost cell technology, identifying and overcoming degradation mechanisms, confirming the structural capability of the porous substrate for reliability, maturing the strip design for improved flow to allow high fuel utilization operation while minimizing degradation mechanisms and obtaining full scale block testing at 19 kW under representative conditions for eventual product and meeting SECA degradation metrics. The SECA program has played a key role within the overall LGFCS development program in setting the foundation of the technology to justify the progression of the technology to the next level of technology readiness testing.

Major technical advances during the course of the program have been:

<u>System and Stack Design:</u>

1. A system cycle has been designed for an IGFC SOFC power module that closely matches that of LGFCS' natural gas distributed generation system cycle allowing market penetration and acceptance of a 1MW-scale product prior to adoption into a 100 MW scale centralized plant fueled by coal synthesis gas. SOFC and operational specifications were established for meeting the DOE target of >60% efficiency.
2. A detailed activity based cost model, excluding learning curves, was established for cost estimation of the IGFC SOFC power model at future the high volume production rates. The audited cost model predicts stack costs at $172.1/kW and a system cost of $505.8/kW based on a peak power calculation ($2007).
3. Strip components were optimized to obtain improved fuel flow uniformity throughout the strips and to provide design for easier manufacturing by powder pressing processes rather than injection molding.
4. Substrate specifications were refined to be based on a functional permeability factor to minimize diffusive resistance ASR contributions and to insure minor elevation of steam to ratios locally within the anode to limit degradation mechanisms.
5. A next generation substrate from the key vendor, achieving improved properties and lower cost, was qualified. Mechanical property characterization involving Oak Ridge National Laboratory revealed the $MgO\text{-}MgAl_2O_4$ substrate to have promising toughness/damage tolerance and slow crack growth characteristics providing favorable design for reliability. The substrates exhibit strength retention after SOFC operation including under high fuel utilization conditions.

<u>Cell Development:</u>

1. A cell-technology stage was selected and validated for carrying forward into the metric block tests. The average ASR of what LGFCS terms the "epsilon" cell technology under system relevant conditions is 0.29 ohm-cm^2 and is sufficient to meet efficiency targets for early product demonstrations. Through the course of the program power densities have improved by ~73%. The improvements have allowed a reduction in the peak stack temperature from 970C to 910C and has been a main contributor to extending the service life from that present before the SECA program.

2. A next stage of cell technology was developed that based on subscale and full-tube testing at relevant conditions provides an ASR reduction down to 0.25 ohm-cm^2 and provides for cost reduction of planned commercial products. Even lower ASR cell technology to <0.22 hm-cm^2 has progressed, based on newer nickelate cathodes, for consideration for mature products in later years after further optimization and validation.
3. The ASR of the primary interconnect has been reduced ~50% and a key degradation mechanism that was initially evident within 2000 hours was mitigated and PIC ASR has shown good stability to 16,000 hours of testing.
4. Studies of the moisture effect on LSM-based cathodes have been conducted and showed a strong temperature dependency that is guiding the product block design/specifications. Alternate cathode chemistries were identified that show less sensitivity to the ambient moisture levels.
5. Through subscale testing to over 16,000 hours under system relevant conditions (temperature, pressure, fuel utilization) LGFCS has identified the key degradation mechanisms present in the active electrodes of its epsilon technology, and which exhibits a service life around 1.5 years while meeting system efficiency requirements. Cathode polarization increases dominate with anode materials migration/coarsening a factor at high temperatures and high fuel utilization conditions. Alternate cathode chemistries show an avoidance of the densification along the electrolyte seen for the epsilon cathode at test times over 8,000 hours and the higher block operating conditions. A next generation anode shows very favorable long-term durability and microstructure stability at extreme, aggressive operating conditions. Tests underway at the end of the program point to technology with the service lifetimes trending towards greater than 2 years with just a cathode modification.

Metric Stack Tests:

1. The Phase 1 test comprised of 2 strips for 7.6kW initial power ran for 2135 hours and exhibited a power degradation rate of 0.5%/1000 hours.
2. The Phase 2 test comprised of 5 strips for 18.8 kW ran for 3043 hours and exhibited a degradation rate of 1.1%/1000 hours under load. The higher degradation rate compared to the Phase 1 test was a result of a printing defect combined with a higher operating temperature for strip 5 caused by a wider block operating temperature range. The printing feature was corrected and degradation improvement validated in a bundle test.
3. Strips for a third block test (4 strips) were fabricated and the testing is to proceed on a follow-on program.
4. The step in testing of the epsilon to block scale revealed issues on manufacturing quality/yield and interconnection between substrates and from strips-to-busbars resulting in some delays to the block tests. The root cause activities associated with those events have served to improve the technology and establish improved designs and specifications to carry into the next stage of technology readiness testing.

2.0 MILESTONE STATUS

The Milestone Log shown in Table 1 represents that included in the Program Management Plan (PMP) for Phase 2.

Table 1 – Milestone Log

Phase 1										
Milestone Description	BP1 (preaward+FY2010)					BP2 - FY2011				Actual End Date
	Q1	Q2	Q3	Q4	Q5	Q6	Q7	Q8	Q9 ext.	
Conduct Kick-Off Meeting	X									4/22/09
Submit Updated PMP		X								10/22/09
Select design for 2nd generation stack		X								12/9/10
Select 2 PICs for durability quailification		X								12/17/09
Submit Stack Element Cost Report			X							1/31/10
Receive qualified 2nd Gen. Stack components				X						4/23/10
Perform Bundle Test at 3.0 bara					X					8/26/10
Fuel distribution optimized for block scale-up					X					8/25/10
Perform 5-cell durability test (3000 hr)						X				11/26/10
Prepare Technical Topical Report									X	11/10/11
Select active layer technology for block test						X				10/13/10
Perform 5-cell durability test (>5,000 hr)							X			2/26/11
Prepare Test Plan								X		6/9/11
Block test stand elect. commissioning completed									X	11/3/11
Perform bundle test at 6.5 bar									X	12/3/11
Demonstrate average cell ASR<0.3							X			3/11/11
Initiate Block Testing									X	3/21/12
Prepare Factory Cost Report							X			
Phase 2										
Milestone Description	BP1 - FY2012									Actual End Date
	Q1	Q2	Q3	Q4						
Kick-off meeting	X									10/7/11
Updated Project Management Plan	X									10/7/11
Start printing for Ph II preliminary block test	X									12/7/11
Initiate Ph I Metric Test		X								3/21/12
Manifold supplier demonstrates orifice tolerance	X									12/1/11
Select next-gen LSM cathode for EIS qualification		X								Feb
Phase I Factory Cost model update										
Select candidates anodes for 3000 hr durability test		X								2/10/12
Freeze cell materials for Ph II block test		X								3/27/12
Start printing for Ph II Metric Test		X								3/27/12
Next-gen parts ready to manufacture				X						7/26/12
Initiate preliminary Phase II Metric Test			X							
Submit Ph II Test Plan		X								3/30/12
Complete press. bundle 3000 hr test Ph II matl's					X					11/9/12
Phase 2B										
Milestone Description					BP1 - FY2013				extension	Actual End Date
					Q1	Q2	Q3	Q4	Q1 2015	
Phase IIB Kick-off					X					12/13/12
Qualify GEN2 substrates					X					12/21/2012
Complete 2000 hour Phase I test and peak power					X					12/21/12
Phase I Factory Cost model update							X			4/30/2013
Submit final Phase I test report						X				3/29/2013
Submit Phase II Topical Report								X		8/14/2013
Begin printing for Phase IIB block							X			5/1/2013
Submit Phase II Metric Test 1500 hour Report									X	10/23/2013
Submit Test Plan for Phase IIB block test on PNG									X	11/5/2013
Select cell technology for final 2-yr EIS screening							X		X	5/1/2013 + 11/1/13
Begin Phase IIB Block Test										on DE-FE0012077
Start low cost zeta bundle test for Ph. 2 cost metric									X	11/13/2013
Submit Phase II Factory Cost Report (Draft)									X	1/29/2014
Complete 5000 hour Phase II test								X		8/23/2013
Submit final Phase II test report									X	10/23/2013
Submit Phase IIB Metric Test 1500 hour Report										on DE-FE0012077
Identify alternate substrate supplier meeting spec.									X	1/30/2014
Validate structural reliability models at bundle scale									X	1/30/2014
Identify/quantify remaining degradation mech.								X		9/30/2013

3.0 PROJECT DETAILS

Activities and technical progress on the individual tasks with the LGFCS SECA program are described in this section.

Task 1.0 - Project Management

Approach - The purpose of this task is to manage and direct the project in accordance with the Project Management Plan to meet all technical, schedule and budget objectives and requirements and ensure that project plans, results, decisions, etc. are appropriately documented and project reporting and briefing requirements are satisfied

Results and Discussion –LGFCS has participated in semi-annual technical reviews, the Annual SECA Workshop, Core Technology Reviews and SECA Program Peer Reviews.

Task 2.0 - System and Cost Modeling

System Modeling:

Approach – It is the objective of the process modeling task to develop an IGFC power plant that integrates the LGFCS design while achieving SECA program objectives. The primary program objectives assessed through the process modeling task are included in Table 2. The net electrical efficiency target of 60% will require challenging process conditions at high fuel cell fuel utilization (Uf) and low area-specific resistance (ASR). It also assumes the eventual commercial availability of an advanced coal gasification plant that generates a clean synthesis gas from coal at 90% efficiency on a higher heating value basis. Modifications to the LGFCS plant design would be required to enable sequestration of CO_2 effluent of greater than 95% purity. Since the power block cost is based on peak power, this will necessitate a power plant design with a significant turndown**.** SimSci-Esscor Pro/II Simulation Modeling is applied to assess fuel cell power plant configurations that yield high efficiency while satisfying numerous operational constraints that include coal as a fuel source and CO_2 as a purified product stream. The process simulations close an energy and material balance around a plant that uses an advanced high-efficiency coal gasification process that yields a high-methane content coal-derived synthesis gas.

Table 2. Primary SECA Program Objectives Assessed with Process Modeling

Efficiency	**≥60%**
Plant Anode Off-gas Effluent	**> 95% pure CO2**
Peak Power Density	**0.52 watt/cm2**
Cost FC Power Block (FC Stack)	**$700/kW ($175/kW)**

Results and Discussion - The current LGFCS natural gas (NG) fired power plant is shown in Figure 1. employs a dry cycle. The cycle includes three loops: cathode recycle, anode recycle and an auxillary loop. The auxillary loop recovers the heat from the off-gas burning (OGB) of the unspent fuel from the fuel cell into the cathode air indirectly using an auxiliary heat exchanger (HX) very similar in design to the internal reformer. The auxiliary heat exchanger is placed at the fuel cell inlet to boost inlet temperature to the required operating value. The auxillary ejector is driven with a slipstream of the plant's compressed feed air, the bulk of which feeds the cathode ejector. Furthermore, the main cathode air exits the process by passing through the auxiliary ejector's flow loop. Therefore, these loops are in series. All of the process mass flow must exit the process through the auxiliary loop.

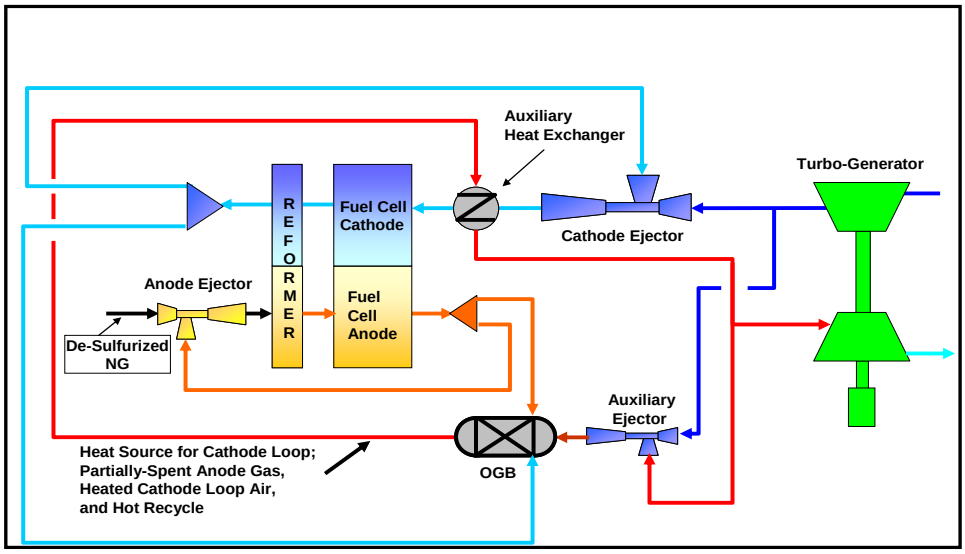

Figure 1. LGFCS plant configurations for natural gas

The process steps that blend spent air with spent fuel in the LGFCS NG-fired Power Plant module to yield a single plant exhaust stream must be avoided in the IGFC cycle in order to yield a highly-concentrated CO_2 product gas. Therefore, the main cathode air must exit the process separately through an expander. Furthermore, the auxiliary loop must avoid the use of the nitrogen-laden air as its motive fluid by employing a slipstream of the sequestered CO_2 and cryogenically-derived oxygen as shown in Figure 2. Sufficient oxygen is added to the motive fluid to avoid a large excess after burnout. The oxygen addition yields a 1% excess after complete oxidation of the spent anode gas, the same assumption made in a DOE study (DOE/NETL 40/080609) that assessed multiple approaches for the coal gasification island integrated with a Fuel Cell Power Plant (IGFC). There will be a slightly increased plant parasitic power demand in this approach associated with the use of an additional slipstream of partially pressurized CO_2 from the sequestration train.

LGFCS went through two iteration cycles on the design of an IGFC power plant fuel cell module. The originally proposed IGFC cycle employed a coal-derived synthesis gas from humidified warm-gas cleanup in conjunction with a single pass arrangement (i.e. no anode recycle) through the power module's fuel cell stack. Anode recycle is normally required to supply steam to the integrated internal reformer. However, the humidified warm synthesis gas from the coal gasification plant already retains sufficient steam for the reforming of the methane component. In this case, additional anode recycle would only dilute reactant concentration, reducing fuel cell performance. Therefore, the original plant concept proposed reforming the synthesis gas in a centralized reformer outside of the LGFCS power module, and would be considered part of the coal gasification island. The heated flow stream used for a centralized external reformer would have been generated by a centralized auxiliary ejector. Therefore, the components in the auxiliary loop's flow path, which include the ejector, the OGB, and the reformer are not integrated into each power module repeat unit. The motive fluid to the auxiliary ejector would comprise a slipstream of the plant's highly–concentrated CO_2 and purified oxygen from the Air Separation unit (ASU). In this layout, the auxiliary loop would be designed with large-scale components. The cost of a centralized reformer would be offset by a simplified LGFCS plant design. Since the heat absorption from internal reforming inside the fuel cell repeat unit would be absent, the auxiliary heat

exchanger would also not be necessary to reach the required fuel cell operating temperature. Therefore, the multiple LGFCS repeat units that would be integrated together to form the large-scale IGFC power plant would be simplified. The pressurized fuel cell power module would have comprised a simplified cathode loop through the fuel cell stacks along with a single pass fuel feed system distributed to the power modules from the centralized reformer. This was referred to as the single-pass IGFC plant concept shown in Figure 2. The anode exhaust from each power module would also need to be collected through a manifold system to pass the unspent product gas to the centralized OGB, to elevate the temperature of the auxiliary ejector's re-circulating flow loop so that it can effectively heat the centralized external reformer.

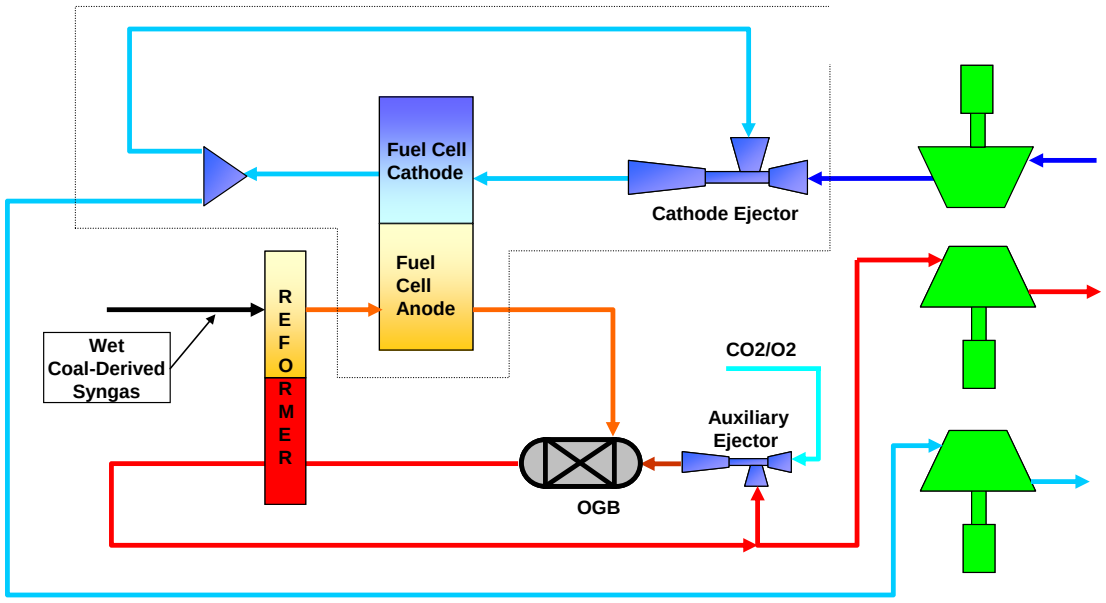

Figure 2. Initial LGFCS Power Module Single-pass IGFC Plant Configuration

Despite the potential simplifications described above, there were several disadvantages that eliminated the adaptation of the single pass approach. The increased complexity of the coal gasification island that would have resulted was not view favorably. In addition, an advanced next-generation IGFC plant may ultimately move toward internal on-cell fuel reforming, completely eliminating the need for a separate reformer. Therefore, cycles that retain an internal reforming function in the LGFCS repeat unit would provide a more simple transition to on-cell reforming. Moreover, the heat balance in the original single-pass cycle showed that it would not be practical to operate at ultra-high fuel utilization (U_f), an important operational requirement for facilitating the achievement of the 60% efficiency targets. The original cycle only allowed maximum U_f of slightly less than 80%. The relatively large balance of unspent fuel was required to provide sufficient heat external to the LGFCS repeat unit for exchange with the internal reforming process, and therefore, achieve a suitable product gas temperature exiting the external reformer. Therefore, although the power module cycle was relatively simple, and perhaps more cost effective from an overall plant perspective, the 60% efficiency target could not be met with this approach.

A second adaptation to the initial cycle shown in Figure 3 incorporates the auxiliary loop and its associated components into the power module, like the NG-fired LGFCS design. When heat recovery and internal reforming are integrated directly into the cathode flow loop as part of the fuel cell repeat unit,

much higher U_f are attainable, while remaining within the fuel cell operational constraints. By altering cathode ejector operating conditions (i.e. primary flow and recycle ratio) the internal reformer can be sustained at the required operating temperature while maintaining the fuel cell within the required operational temperature window. Since the modified cycle could be operated at ultra-high U_f , higher IGFC electrical efficiency was possible.

Anode recycle was applied in place of the original single-pass anode-side approach. The final down-selected cycle is shown in Figure 3 and is very similar to the natural gas LGFCS power module cycle. It was assumed that a dry coal-derived synthesis gas would replace the warm wet coal–derived synthesis gas because it results in a stack exit condition that is less susceptible to anode degradation caused by overly high p^2_{H2O}/p_{H2} ratios at the desired fuel utilization ratios required for the efficiency targets. With the dry feed, anode recycle was required to supply the required steam for the internal reforming**.**

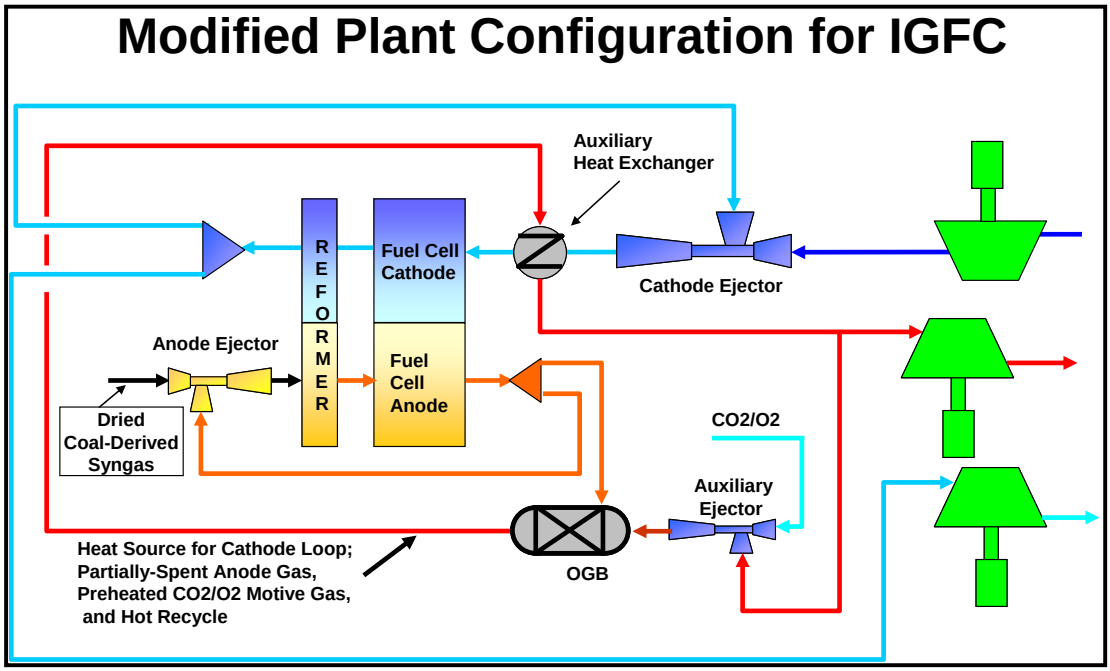

Figure 3. Final Modified LGFCS Plant Configuration for IGFC.

Table 3 compares the anode exit compositions for IGFC systems run with the warm gas clean-up (wet feed) versus a low temperature clean-up (dry feed) for different U_f. At an overall U_f of 90%, the wet synthesis gas from warm gas clean-up would have exit flammables of only about 6.8% with a relatively high steam content of 63.8%. By comparison, the dry synthesis gas which employs anode recycle shows an exit flammables concentration of about 9.5%, and a relatively low steam content of 47.9%.

Table 3. Impact of fuel type and U_f on fuel cell stack exit flammables and steam content.

Cycle	NG_dry	IGFC, Dry Feed	IGFC, Dry Feed	IGFC, Wet Feed	IGFC, Wet Feed
U_f (Species)*	80.0%	80.0%	90.0%	80.0%	90.0%
U_F (HHV)*	74.4%	76.0%	88.0%	76.0%	88.0%
Anode Exit Composition					
H2	16.30	9.55	4.75	8.98	4.48
CO	8.92	9.34	4.70	4.58	2.30
Total Flammables	25.22	18.89	9.45	13.57	6.78
H2O	47.41	43.14	47.94	59.28	63.78
CO2	23.06	37.53	42.17	26.87	29.15
x^2_{H2O}/x_{H2}	1.38	1.95	4.84	3.91	9.08

Coal Gasification Plant - The coal gasification island considered two variations on an advanced gasification plant published by DOE NETL. The advanced gasification island generates a synthesis gas rich in methane, hydrogen, and carbon monoxide at an efficiency of approximately 90% using a low-temperature catalytic gasifier that combines catalyst, coal, steam, and a limited quantity of cryogenically-derived oxygen that yields the required gasification temperature. Additional oxygen is also generated for the burnout of spent anode off gas exiting the FC power plant. In the DOE study, two synthesis gas clean-up trains were developed that include an advanced humidified warm-gas clean-up approach, and a conventional dry cold gas clean-up approach. As described in Section 2.2, the early IGFC cycles used the synthesis gas clean-up train that generated warm humidified synthesis gas, however, the final down selected cycle used the cold gas clean-up approach. Figure 4 shows the high-level process steps for each approach which was laid out in the DOE study. It was the task of LGFCS to ensure that the back end heat recovery from the LGFCS power module would be sufficient to satisfy the steam-generating requirements of the coal gasification island in a cycle with an over-all electrical efficiency of 60%. In addition, sufficient low-grade heat must remain available for the ancillary equipment needs of the coal gasification island, such as coal drying.

The subsequent process modeling work used the synthesis gas composition that resulted from this DOE study as the feed stream to the RRFCS plant. The following Table 4 shows the assumed coal-derived synthesis gas composition for the warm-gas and cold-gas clean-up streams. Only the early work, described in the preceding section used the warm-gas approach. The cold-gas approach use more conventional low-temperature sulfur removal processes that also knock-out the bulk of the H_2O.

Table 4. Coal Derived Synthesis Gas Composition to LGFCS Power Module

Component	Cold Gas Clean-up	Warm Gas Cleanup
H2	25.17%	15.15%
H2O	0.53%	38.50%
CO	9.11%	5.62%
CO2	35.98%	22.40%
CH4	28.52%	17.84%
N2	0.66%	0.41%
Ar	0.03%	0.02%

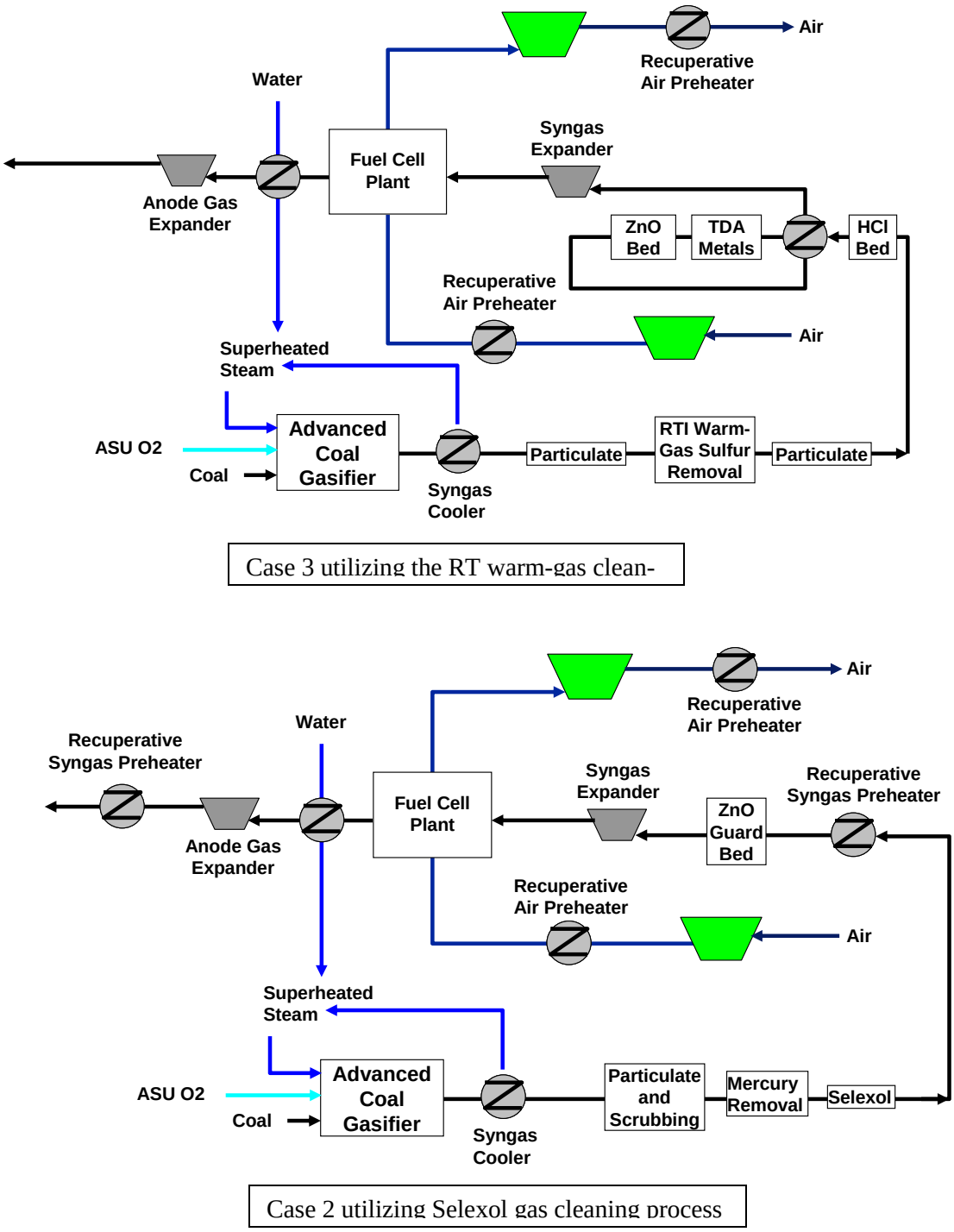

Figure 4. Conceptual schematics of the two IGFC gasification island approaches following from the NETL study (DOE/NETL 40/080609). Case 2: Selexol process, Case 3: RTI warm-cleanup.

The dry synthesis gas from Table 2 requires 0.566 g/s of slightly superheated steam per gram of synthesis gas generated. The DOE study indicates that about 55% of the steam generation must use heat recovery from the backend of the RRFCS power module. A suitable source for this heat recovery was upstream of the anode gas expander in the cycle. The bulk of the heat downstream of the cathode side expander was recovered by increasing the preheat temperature of the cathode ejector primary as it enters the power module. The percentage of power consumed parasitically for the case 2 plant auxiliary

components from the DOE study were used to calculate efficiency. However, the parasitic power required to sequester CO_2 was increased by about 40% to account for the additional CO_2 that must be re-circulated to drive the auxiliary ejector in the LGFCS power module.

Process Simulation of the Down-Selected Cycle: Provision II (PROII) process modeling software from Invensys Systems, Inc was used in this assessment. The model incorporates customized reformer and fuel cell models that are integrated into the process simulation. The fuel cell model is simplified to represent a single surface operating at average cell conditions. The model solves the energy and material balance on inlet and outlet streams, with the split between heat energy and electrical energy determined by both the thermodynamically limiting performance, and the estimated average electrical resistance of the fuel cell at an average condition. Correction factors are applied to predict the average cell resistance while accounting for the primary environmental variables that impact cell resistance. These variables include temperature, pressure, fuel-side hydrogen concentration, and air-side oxygen concentration. The impact of these variables on the relative cell resistance is calculated using a separate more fundamental differential cell model (FDCM) that yielded curve fits that were included in the Provision Model.

The FDCM represents activation loss, mass transfer resistance, and electrolyte resistance across a differential fuel cell surface at a single process condition (T, P, x_{O2}, x_{H2}). The FDCM was set-up to represent the LGFCS cell geometry. Using the correct parameters that include (anode porosity, anode tortuosity, ionic conductivity, molecular diffusion coefficients, etc.) the FDCM reasonably represents experimental cell data. A calculated relative resistance of one represents resistance at a typical average operating condition (i.e. 860ºC, 6.4 bara, 12.5% O2, 30% H_2) used in laboratory testing, and currently corresponds to a value of about 0.3 ohm-cm^2. This value includes an added resistive estimate of electrical interconnects that will exist in the stack design.

To estimate cell resistance as conditions vary from the reference condition, curve fits were generated from the FDCM model and employed in the PROII process simulation model. The curves fits in the PROII fuel cell model are integrated between the inlet and outlet stream values of the dependent variables to derive the scale factor for each environmental variable. Multiplied together they represent an overall correction factor to the currently achievable cell resistance value of 0.29 ohm-cm^2 at the average set of environmental conditions around the stack. An additional ASR technology scale factor (TSF) represents future improvements to the current technology and is an important parameter in estimating the required improvement to achieve a targeted efficiency goal while simultaneously accounting for the environmental effects that exist around the cell in the real process operating at the high efficiency condition. The approach outlined above represents a reasonable and efficient estimate of cell performance without resorting to more computationally intensive and complicated one-dimensional and two dimensional fuel cell models that would be difficult, and perhaps impractical to incorporate into the Provision II process simulation.

Simulation Results: LGFCS Power Plant Process Pressure: One means to boost IGFC power plant efficiency would be to operate at high pressure. Fuel cell performance is known to increase at high pressure. Reaction rates and molecular diffusion rates increase with pressure. In addition, the thermodynamic limiting efficiency also increases with pressure. However, the process simulations indicated that the overall impact on system efficiency for the hybrid system was quite small. In addition, there are factors related to ejector design which would likely favor the operation on the lower end of the simulated pressure range.

To show the effect of pressure on performance, the process simulation model was operated at three pressures; 25 bar, 10 bar, and 5 bar. In all cases, a LGFCS power module repeat unit was simulated with a constant fuel cell surface (85.4 m^2) and a constant U_f (85%). A constant U_f was achieved by holding the current constant at a constant fuel feed rate. For the LGFCS power module repeat unit, a coal feed a

thermal input of 600 kW on a higher heating value basis was required. This corresponds to a coal-derived synthesis gas feed rate of 540 $kW_{thermal}$ from the advanced coal gasification island (at 90% gasifier efficiency). As Figure 5 shows, increasing pressure yields a significant decrease in the predicted ASR, and a slight increase in reversible voltage occurs. However, the degree to which fuel cell performance improved with pressure was significantly lessened by a trend toward lower oxygen concentration with increasing pressure on the cathode side of the fuel cell. This effect is depicted by the ASR scale factor representing oxygen concentration in Figure 5. As the pressure increased, the expansion ratio on the turbine expanders also increased, yielding more cooling of the exhaust gas exiting the turbines. Therefore, less heat is available for heat recuperation, and in order to maintain the required fuel cell inlet temperature, the relatively cool air feed is reduced in combination with higher cathode recycle flow. The designed temperature change from fuel cell inlet to outlet was also maintained by sustaining a roughly constant total flow through the fuel cell. At the constant fuel feed and total current, the reduced air flow in combination with higher recycle yields a significant drop in the average oxygen concentration with the resulting negative effect on ASR. The reduced oxygen concentration also diminished the positive impact of pressure on the reversible voltage.

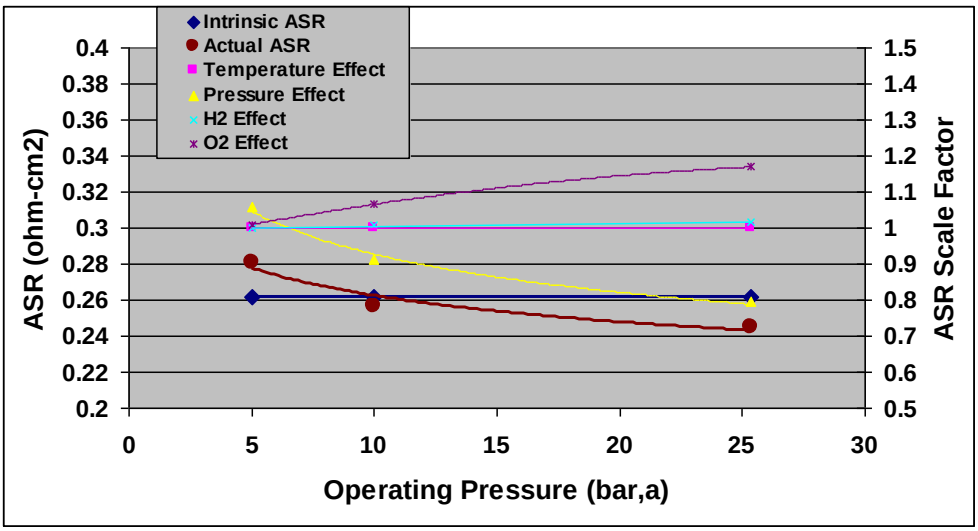

Figure 5. Impact of pressure on ASR. The assumed cell performance at reference conditions was approximately 0.26 ohm-cm^2.

The three pressure sensitivity simulations peak at an efficiency near 58% (Figure 6). The roughly a 2% improvement in fuel cell efficiency shown as a 12 kWe increase in power output over the simulated pressure range (2 to 25 bar), however, the fuel cell power increase was partly offset by a decrease in net turbine expander power owing to the compression work required to achieve a constant pressure ratio of 1.26 for driving the cathode ejector. The number of inter-cooled compression stages for the compressed air was held constant at three. Therefore, the net effect of pressure on system efficiency was very slight, showing a maximum improvement of about 1% at an intermediate value in pressure. In fact, design constraints on the cathode ejector may negate the small predicted efficiency gain at an intermediate pressure. Subsequent simulations will show that a U_f (species) near 90% would be required to reach an overall net electrical efficiency of 60%.

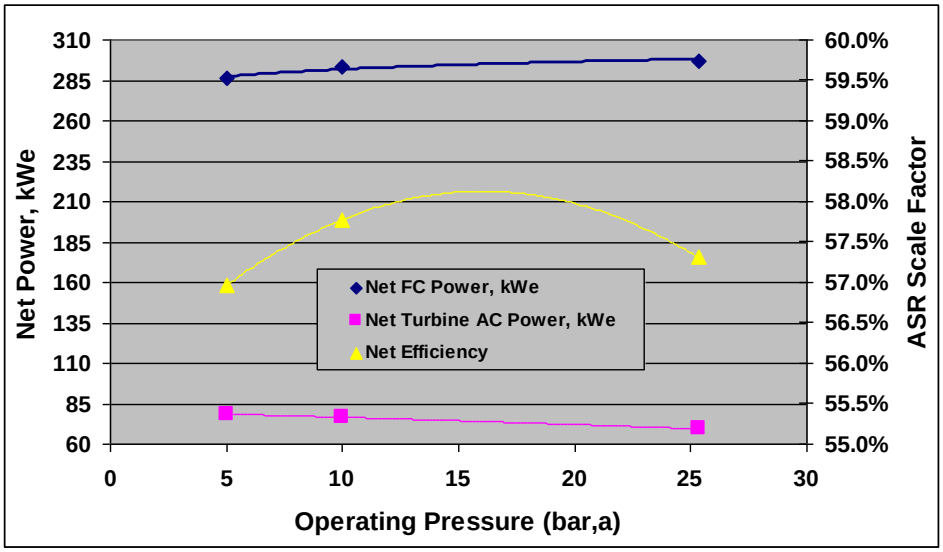

Figure 6. Net impact of elevated pressure at constant cathode ejector pressure ratio.

Another factor to consider for higher pressure operation is the methane thermodynamic equilibrium concentration in the gas exiting the internal reformer. Unconverted methane from an assumed 830C reformer exit temperature increases from 1.5% to 20% on a change in pressure from 5 to 25 bar. This would result in a significant increase in the degree of on-cell reforming forced to occur downstream of the internal reformer. A fuel cell design would be required to accommodate the thermal stresses and avoidance of carbon deposition associated with on-cell reforming.

Simulation Results: On-Cell Reforming: On-cell reforming was considered for its potential benefits on the stack thermal management. The implementation of on-cell reforming would eliminate an internal reformer, potentially simplifying the system and reducing cost. By employing on-cell reforming, the heat release associated with fuel cell power generation is partly offset by heat absorption associated with the internal reforming of methane. Therefore, less air is required to sustain a given stack temperature gradient. Alternatively, for the same air flow, the stack temperature profile can be compressed toward the upper portion of it range to minimize ASR or the stack temperature shifted downward to benefit degradation. The impact of a reduced ASR on system efficiency was evaluated.

The fundamental differential fuel cell model (FCDM) was modified to simulate the gradual consumption of methane through the fuel cell anode. The assumptions on which the model is based are depicted in Figure 7, and can be described as perfect on-cell reforming. The revised model actually includes the molecular diffusion of methane in the calculation of the mass transfer activation loss in the anode layer. Methane comprises a significant fraction of the synthesis gas composition on the inlet side of the anode flow passage. As the gas passes over the fuel cell anode surface, methane reforms on the nickel-rich anode surfaces as it diffuses through the anodes porous structure toward the electrolyte interface. The main assumption in the model is that the reforming reaction is relatively fast, and therefore, the consumption of methane is a diffusion-controlled process in the anode layer. Perfect reforming would assume that the diffusion rate is sufficiently fast to consume all of the methane out of the anode flow passage by the time the gas reaches the exit side of the anode.

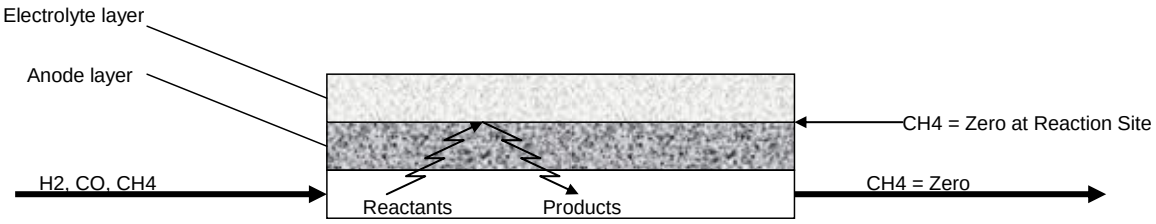

Figure 7. Description of conditions for on-cell reforming

Table 5 shows PRO/II process simulation modeling of the impact of on-cell reforming on the thermal balance by the compression of the stack temperature profile as internal reforming was shifted from an upstream integrated internal reformer to an on-cell reforming process (constant 6.4 bar, 600kW coal feed, U_f=85%). On-cell reforming was controlled by setting the methane conversion on the internal reformer model to 100%, 50%, and 0%. The simulations were constrained to yield a constant ejector recycle ratio (CRR) of six to ensure that this component could be designed while allowing for reasonable cathode loop pressure drops. The constraint of constant CRR yielded a significant reduction in primary air flow as the fuel cell temperature profile was contracted to a higher average temperature. At constant CRR and constant stack exit temperature (900ºC), the primary air was reduced to achieve the higher FC inlet temperature via the auxiliary heat exchanger. Therefore, the net heat released in the fuel cell and the total flow through the fuel cell both decrease as on-cell reforming increases. The simulation results show a significant decrease in ASR with on-cell reforming due to increasing temperature. However, the improved ASR was offset by a corresponding decrease in the reversible voltage, with the net effect of yielding very little increase in fuel cell power, and therefore, no net efficiency gain was achieved. There is still a potential benefit to fuel cell reliability by the potential exposure to a decreased temperature gradient that results with on-cell reforming as long as carbon formation is avoided. LGFCS is examining stack technology with on-cell reforming as a means for cost reduction (elimination, minimizing reformer costs) and increasing volumetric power density for the block (more strips/block).

Table 5. Impact of On-Cell Reforming on Performance

On-Cell Reforming Results				
% On-Cell Reforming		0	50	100
Power	kWe	284	284	283
Fuel Cell Operation				
Model ASR		0.387	0.350	0.303
Vreversible	volts	1020	1003	977
Vop	Volts	841	842	837
Current	amps	1.21	1.21	1.21
Current Density	ma/cm2	427	427	427
Air-Side Conditions				
Air Inlet Temperature	deg. C	800	817	836
Air Outlet Temperature	deg. C	900	900	900
Air Inlet Flow	g/s	268	251	233
Cathode Recyle Ratio		6	6	6
Fuel Cell Anode In				
H2	mole %	26.25	18.31	9.49
CO	mole %	23.49	18.38	11.26
CH4	mole %	0.22	4.55	9.82
Fuel Cell Anode Out				
H2	mole %	7.24	7.05	6.81
CO	mole %	6.93	6.91	6.85
CH4	mole %	0.00	0.00	0.00

The most significant operating parameters that effects achievement of the 60% efficiency target is U_f and ASR and extremes of these will be required to reach the overall plant efficiency target of 60%. U_f can be defined in two manners; one based upon the heating value of the fuel mixture that enters and leaves the anode loop, the second based on the percentage of the total reactant species that are consumed on the fuel

cell. The second definition is directly proportional to current. The single-pass U_f is based on the inlet and outlet feeds to the fuel cell, and the overall U_f is based on the inlet and outlet feeds to the anode loop. With anode recycle employed, the single-pass U_f is smaller than the overall U_f. Without anode recycle, they are equal. The relationship between the two definitions (HHV and Species) is shown in Table 6 for coal-derived synthesis gas.

Table 6. Comparison of the overall U_f values based upon heating value and reactant species

Heating value	**70**	**76**	**82**	**88**
Reactant Species	**75**	**80**	**85**	**90**

Table 7 shows predicted increase in plant efficiency as U_f is increased. The table indicates that a U_f (species) of about 90% and a technology scale factor on ASR of about 55% are required to achieve the overall plant efficiency target of 60%. The reported power values in the Table are based on a coal thermal input of 1000 MW for an entire plant on a higher heating value basis. The first column represents current fuel cell technology operating at an 85%(species) U_f. Current technology corresponds to a TSF of one, or and ASR of approximately 0.32 ohm-cm^2 at the nominal cell operating condition.

Table 7. Efficiency predictions as a function of U_f and ASR (5 bar operation).

Efficiency Table (based on 1 MW thermal Input)		Current Fuel Cell Technology	Advanced Fuel Cell Technology	Advanced Fuel Cell Technology	Advanced Fuel Cell Technology
ASR (TSF)	ohm-cm2	0.318 (1.0)	0.284 (0.9)	0.298 (0.9)	0.194 (0.55)
Leakage current loss	%	2.33	0.00	0.00	0.00
FCFU(species)	%	85.0	85.0	90.0	90.0
Advanced Coal Gas Efficiency	%	90.0	90.0	90.0	90.0
Fuel Cell DC Power, with Inverter Loss (97%	kWe	474.4	485.9	497.0	525.0
Turbine Power*		134.4	129.8	124.7	113.0
Syngas	kWe	25.6	25.6	25.6	25.6
Fuel Cell Air Compression	kWe	-91.6	-87.4	-80.6	-68.3
Fuel Cell Air Expansion	kWe	156.5	148.0	135.1	111.1
Anode Exhaust Expander	kWe	44.0	43.6	44.6	44.6
Total Gross AC Power	kWe	608.9	615.8	621.7	638.0
Parasitic Power Loss w/o CO2 (3.82%)	kWe	39.0	39.0	39.0	39.0
CO2 Compression Loss (3.66%)	kWe	37.4	37.4	37.4	37.4
Efficiency without CO2 Compression	%	57.0	57.7	58.3	59.9
Efficiency with CO2 Compression	%	53.2	53.9	54.5	56.2

*** Adiabatic Isentropic Efficiency of 88% for Expansion, and 86% for Compression**

The ASR must also be significantly improved to reach the 60% target. All the model simulations set a constant fuel cell surface for the LGFCS repeat unit. This is based on the approximate peak power densities required to reach cost targets for the system. Therefore, as the U_f of the nominal power condition increases, current density will also increase. In order to achieve the required increase in nominal power density at higher current density, ASR must also decrease to keep the output voltage elevated. Furthermore, high U_f depletes the fuel gas of reactant species, reducing the average ASR, and average reversible voltage. This is depicted in Table 7 when U_f is increased from 85% to 90% for cells yielding the same performance at reference conditions (TSF=0.9). The ASR increased from 0.284 to 0.298 due to environmental factors. Therefore, the intrinsic ASR (the ASR at reference conditions) of the cells achieved must decrease to compensate for these environmental effects. LGFCS has demonstrated cell technology approaching the 0.2 ohm-cm^2 level with advanced mixed electronic and ionic conducting nickelate cathodes and when combined with optimization of other cell layers such as lower resistance single layer anodes and primary interconnect design and materials with lower ohmic losses. This stage of cell technology requires further optimization and durability testing, especially at the high fuel utilizations required for IGFCS efficiency targets. Investigations are also underway to reduce the leakage/parasitic currents of the LGFCS integrated planar cell/stack technology.

Hybrid natural gas co-fired IGFC cycle: A near-term IGFC plant could be configured to integrate conventional coal gasification technology that sequesters CO_2 upstream of the fuel cell power plant. The conventional coal gasifier would establish a base load, using co-firing of natural gas to boost performance at elevated load. The abundant supply of natural gas in the US as well as its relatively benign environmental impact might foster this approach while permitting the countries abundant energy stores in coal to also be used as an energy source. Given the challenges associated with commercializing an advanced coal gasification plant, the conventional coal gasification plant may provide a more practical near-term approach. The integration of the fuel cell power plant with a base load conventional coal gasification plant with the capability of co-firing natural gas will have advantages that include:

- Operating a complex gasification plant at a single base load that could lead to,
  - a less expensive gasifier plant due to a reduction in load,
  - reduced coal gasifier downtime due to operation at a single load, and in a gasifier downtime event,
  - the plant can still produce power operating on 100% natural gas.
- Operating the fuel cell power plant in its natural gas configuration which,
  - no longer requires careful control of differential pressure between cathode and anode since the streams can mix in a common exhaust, and which,
  - no longer requires separate streams of O_2 and CO_2 used for controlling the burnout and heat recovery of spent anode off-gas.
- Operating the fuel cell at relatively low current density at the base load to help offset the reduced plant efficiency operating on 100% coal-derived synthesis gas.
- Achieving a high load, high efficiency case that can reach 60% without operating at ultra-high fuel cell fuel utilization of 90% which may represent technical challenges related to fuel cell durability. A high efficiency plant using natural gas co-firing is achieved by,
  - reducing the fuel penalty by reducing the impact of the relatively low efficiency coal gasification process on overall fuel feed,
  - reducing the impact of the high parasitic power loses from the coal gasification plant on overall plant efficiency, and
  - displacing hydrogen fueling of the fuel cell with methane, a more efficient fuel.

The integration of the fuel cell power plant with a base load conventional coal gasification plant with the capability of co-firing natural gas will have disadvantages. The plant would have overall lower efficiency and CO_2 capture rates, estimated at 50% when operating on only coal-syngas (88% CO_2 capture) and hitting 60% efficiency when using a 50:50 blend of coal and natural gas. At an assumed median load condition of 66:33 coal to natural gas the efficiency is estimated at 57% with 70% CO_2 capture.

Conclusions - An IGFC SOFC power module cycle has been selected that duplicates very closely that of the nearer-term commercial opportunity for a natural gas distribution power generation SOFC system. This means that initial smaller (1MW) LGFCS SOFC distributed energy systems can provide the technology demonstration and market acceptance for a future larger-scale (>100MW) and more aggressive IGFC application of the SOFC technology. Achieving the publicized 60% IGFC plant efficiency targets will require further ASR improvements in the LGFCS SOFC technology, proven durability at required 85-90% fuel utilizations, demonstration of a catalytic gasifier and proven pressure control management between the separated air and fuel streams. System modeling showed that neither higher pressure operation of the SOFC power module nor on-cell reforming provide significant efficiency benefits. A pressurized hybrid coal-syngas plus natural gas fired system using currently available gasifier technology is proposed that could achieve a high percentage of carbon capture but at a somewhat reduced efficiency level.

Cost Modeling:

Approach – An activity based Stack Cost Model was prepared for costs up through assembly of the fuel cell block that was initially designed as a seven strip block for a 1MW natural gas distributed power generation system in which the block would achieve an ~27kW power rating at normal operating conditions. The cost model does not utilize any learning curve assumptions. Raw material costs are based on recommended values provided by the DOE in the Minimum Requirements Document where possible. Otherwise, high volume cost estimates are requested for raw materials/components and cost analyses performed for high volume substrate and components. Ultimately the strip and block size may be increased for coal-based system and the cost model will then be modified. Factory Cost Model Reports are submitted that includes the balance of plant components of the SOFC module (anode protection gas system, turbogenerator, power electronics, control system, and packaging) along with the stack costs. Probablistic analysis was also added to the cost analysis through the use of Crystal Ball software to run Monte Carlo simulations. Variables chosen for the Monte Carlo runs were those that ranked high in their contribution to the overall cost and which had greater risk for cost increase or potential for cost reduction. Probabilities were assigned to a range of projected costs for those variables/components. The SECA cost metric targets in Phase 2 were <$700/kW for the IGFC SOFC power module and with <$175/kW of the cost being that associated with the SOFC stack. (all in 2007 dollars).

Results and Discussion – LGFCS submitted a Phase 2 Cost Report based on the audited cost model developed during Phase 1. Since Phase 2 had a stack cost metric in addition to the overall system cost, the model was altered to provide the cost of the stack configuration as shown in Figure 8. Changes from the Phase 1 analysis include the lower cost anode technology, accounting for some reclamation of materials, the larger sized substrates and a more efficient printing operation. The cost model predicted an average stack costs of $172.1/kW with a 93.4% confidence level within ±25% of the mean. The predicted system cost is $505.8/kW with a 100% confidence level of within ±25% of the mean (Figure 9). These analyses used the 530 mW/cm^2 peak power level achieved in the Phase 1 test.

Figure 8. Stack unit for the Factory Cost Model

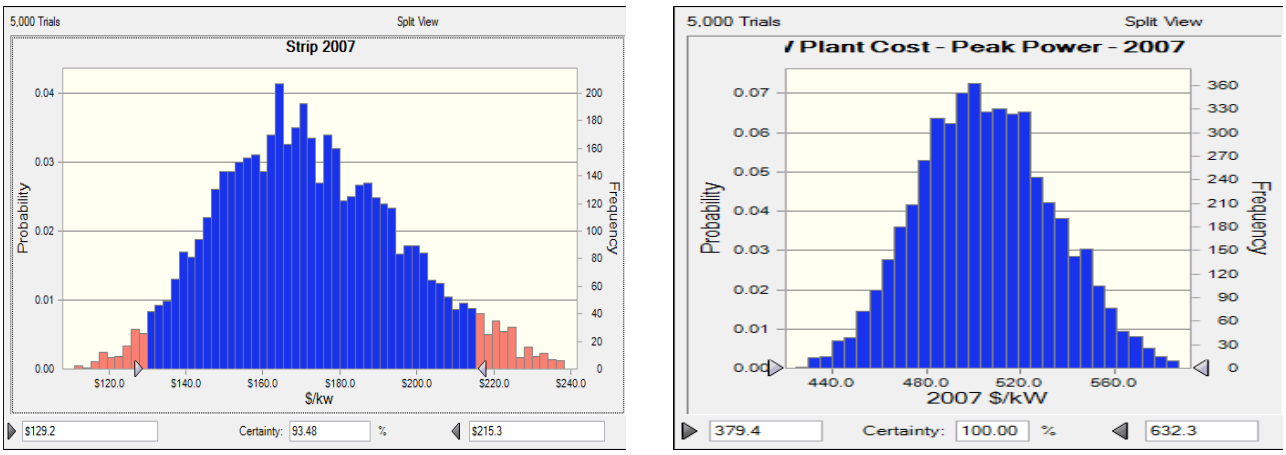

Figure 9. Monte Carlo results for stack and system costs

Conclusion- The Phase 2 Factory Cost Model shows the ability of a LGFCS IGFC SOFC power module to meet the $700/kW system cost target and the associated stack cost of <$175/kW. Further cost reductions (based on normal operating conditions) will be achieved through the lower ASR cell technology being validated for entry-into-service product and through block design changes allowing higher current/power densities for the cells and higher volumetric power densities for the blocks.

Task 3.1 – Strip Optimization

Approach – The LGFCS stack technology was evaluated for changes to improve performance, electrochemical durability and cost. Analysis of the current stack design was performed to extend the understanding of fuel distribution and pressure drop throughout the ~4 kW strips (at normal operating condition) which make up the LGFCS fuel cell system. Fuel manifold components that distribute fuel into and out of the 12 parallel bundles of each strip are designed/optimized to achieve improved flow uniformity across all bundles and across the width of the substrates making up each bundle (a bundle consists of 6 substrates with series connection of electrical current and fuel flow). Design options are evaluated by 1-D network and computational fluid dynamic modeling with validation of the modeling results achieved through gas chromatography, tracer gas techniques

The LGFCS stack consists of a block containing 5 strips (Figure 10). Each strip contains 72 porous Magnesia Magnesium Aluminate (MMA) substrates onto which the fuel cell layers are printed. These substrates are converted into a sub-assembly by attaching dense MMA components to each end of the substrate using a glass-ceramic material. These substrates are then built up into a bundle which contains six of each of these sub-assemblies. The bundle is essentially the smallest sub unit in terms of the functioning of the stack, each bundle has a fuel inlet and outlet substrate, and 12 bundles combined to form the strip. The strip is connected to the fuel system using metallic elbows connected to the strip via a metal ceramic joint to feed the fuel into and out of the stack. Bundles within the strip are in parallel with respect to fuel flow. Inside an LGFCS strip, there are three types of fuel connectors:

- Pipes: main fuel lines that feed all twelve bundles and remove the excess fuel out of the strip.
- Manifolds: connectors between pipes and bundles. These components distribute fuel from the fuel pipes into the first substrate of the bundle and connects the sixth substrate of the bundles into the outlet pipe.
- End-caps: substrate connectors within a bundle. There are 5 pairs of end-caps in a bundle, each pair connects two substrates.

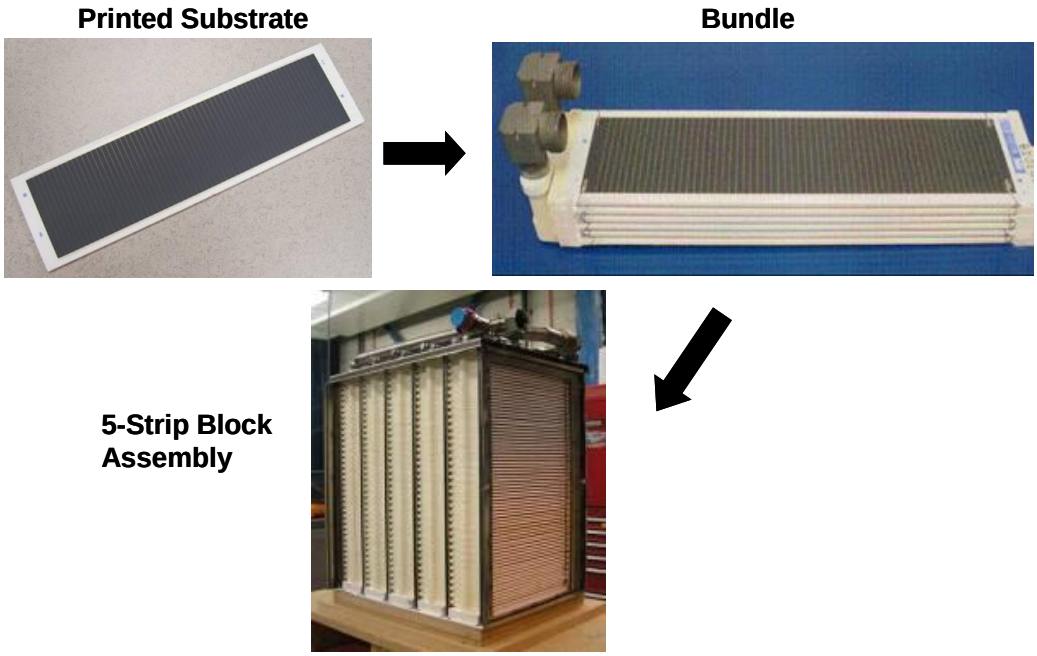

Figure 10. Building blocks of the LGFCS stack

Status of Fuel Distribution Pre-SECA Program: Experiment and CFD analysis had shown that the alpha stack design (pre-SECA design) was providing an uneven flow of fuel to the bundles in the strip, Figure 11. This resulted in the potential for fuel starvation within the stack, particularly in the outlet substrates of each bundle. Fuel starvation is known to not only decrease the overall output of the fuel cell stack but also to increase the degradation of the anode. It was deemed necessary therefore, that to meet the SECA durability targets, the fuel distribution would need to be modified in order to supply equivalent quantities of fuel to each bundle.

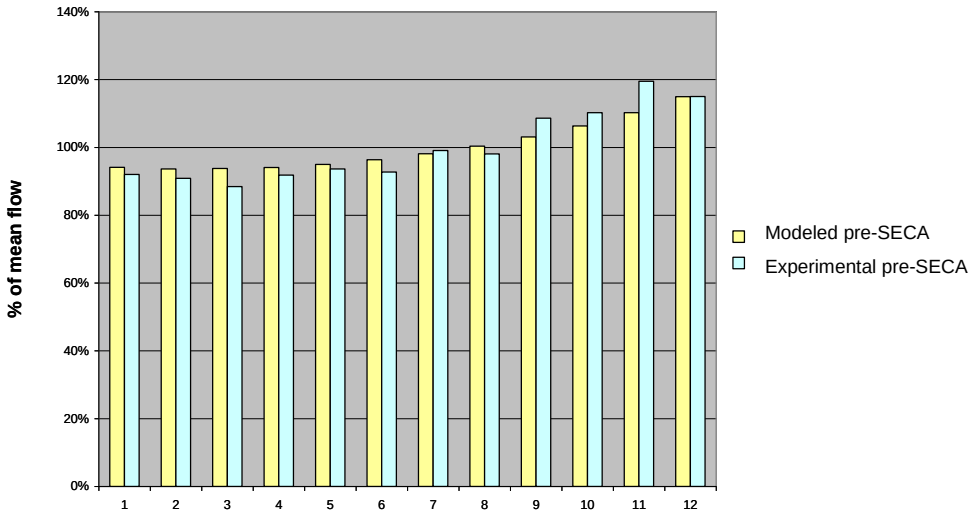

Figure 11. Bundle to bundle fuel flow distribution in alpha (pre-SECA) strip

In addition to the unfavorable bundle-to-bundle distribution, the earlier alpha design exhibited fuel maldistribution within the substrates with a variation of 60% of the mean flow between the highest and lowest channel flows (Figure 12). Combining the maldistribution for the worst alpha bundle and the worst channel of a mid-bundle substrate, a deficient mean flow of only 70% is achieved.

Strip component redesign – Stage 1: The first stage of redesign was aimed at minimum changes to the strip components that could be made in time to impact the Phase 1 and Phase 2 block-scale tests. The fuel flow within the stack is primarily controlled by the pressure drop within the structure which effectively provides a resistance to the fuel flow in different sections of the strip. In order to manipulate the pressure drop effectively a large budget is desirable and, due to the pressure drop restrictions imposed on the stack by other components of the anode loop, the first step in the re-design of the stack was to reduce the pressure drop across the strip. Computational fluid dynamics (CFD) analysis of the pre-SECA alpha design showed the main contributor to the pressure drop to be the end-caps which transition the fuel from substrate-to-substrate within the bundle. The decision was taken to re-design the end-caps to reduce the pressure drop and, at the same time, to attempt to reduce the cost of manufacture by reducing the complexity. The intention was to make it possible to die press the parts rather than requiring powder injection molding and lost-core technology for inner flow features. Die pressing of ceramic components can reduce the tooling cost, cycle time (both forming and processing) and results in higher yields, i.e. less scrap.

The conceptual design for the new end-caps (termed the epsilon technology stage) were analyzed using CFD and the results showed that the new design reduced the pressure drop between substrates from 85Pa to 4Pa. To validate this data, stereolithographic end-caps of the new design were produced in order to construct a model of the new bundle. The bundle test piece was subjected to various flow checks to establish the pressure drop within the structure and the results were shown to be in good agreement with the CFD results and the total bundle pressure drop was reduced by about 50% (confirmed experimentally). A key benefit of the end cap change was an improved channel to channel fuel distribution across the individual middle substrates of the bundle as shown in Figure 12 (the T prefix refers to substrate number).

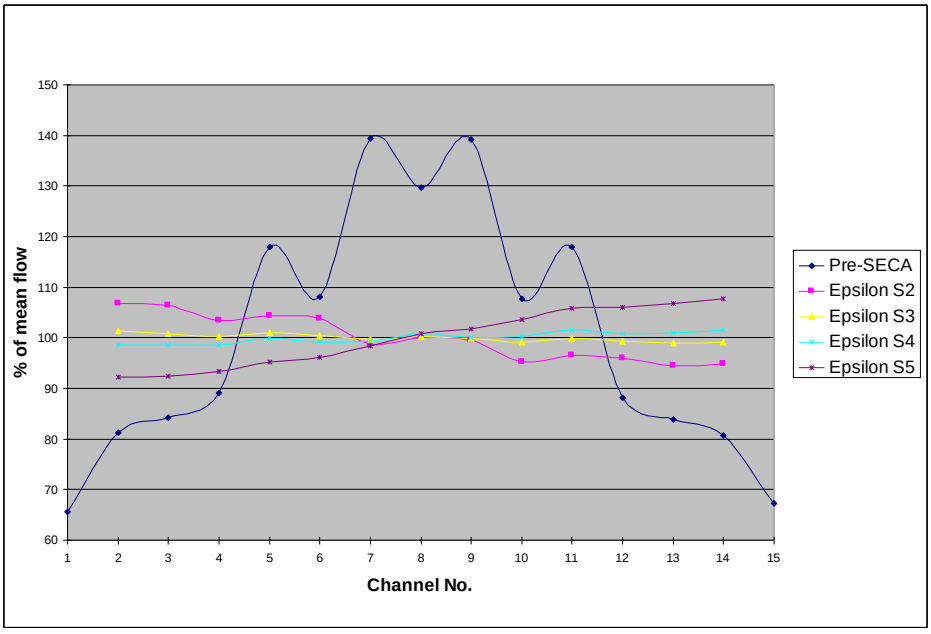

Figure 12. CFD modeling results of fuel distribution across the middle substrates

The reduction in the pressure drop provided by these new end-caps allowed some design space to exploit for improving the bundle-to-bundle fuel flow distribution for the strip as well as improving the channel-to-channel distribution in the outlet substrates, which did not benefit from the end-cap changes. The options available to achieve this were either a complete re-design of the inlet and outlet bundle manifolds or an intermediate solution using a supplemental dense MMA component during bundle assembly to contribute the necessary flow control features. The intermediate design solution option was chosen for the benefits offered, such as flexibility (many designs could be tested if necessary), cost (no expensive tooling involved) and speed (components could be acquired in weeks rather than months). The timing factor was the most important as it was necessary to incorporate these features into the stacks for the metric test. Once this concept was accepted as the credible way forward, CFD modeling commenced to investigate the optimum design. By minimizing the design changes to the manifold, this also meant that the alpha fuel pipe design would be retained for the first stage of redesign.

Within the LGFCS stack, the substrates are grouped in collections of six termed a bundle. Any fuel maldistribution within the inlet substrate resulting from the asymmetric design of the inlet manifold is not a concern because of the low fuel utilization for that substrate. Any inlet substrate maldistribution is alleviated downstream during mixing on fuel transport substrate-to-substrate through the end-caps. The greatest concern for bundle fuel distribution is the outlet substrate where the average fuel utilization is already high with reduced hydrogen and CO content and elevated steam levels. Any maldistribution within the outlet substrate could lead to localized cell regions experiencing fuel starvation thus increasing ASR/concentration losses and causing locally higher degradation rates. The asymmetry in design of the bundle outlet manifold necessitated by the overall strip fuel manifold induced maldistribution with the outlet substrate even with the end-cap redesign. To improve the flow distribution between the 13 channels of the outlet substrate, an additional MMA component was placed between the outlet of the substrate and the fuel manifold to balance the fuel distribution. CFD analysis (Figure 13) shows the improvement in the channel-to-channel distribution for the outlet substrate for the Stage 1 redesign.

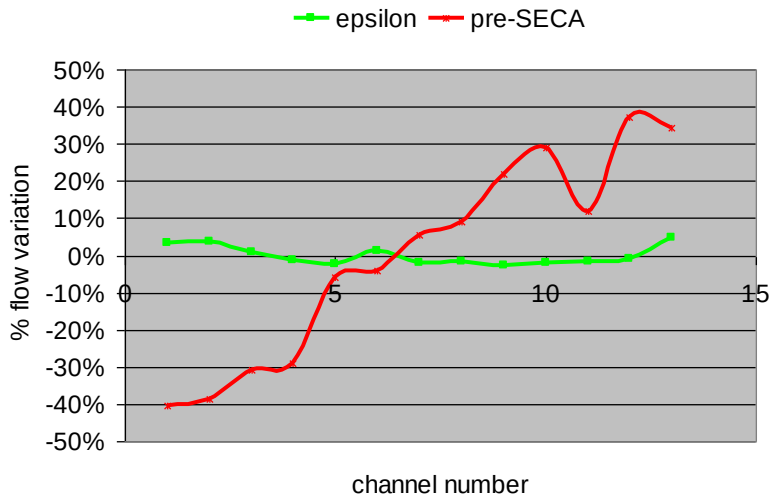

Figure 13. CFD Channel-to-channel fuel distribution result for the bundle outlet substrate

The channel distribution modeling results were validated in two ways, by flow visualization using clear stereolithographic components and by an electrochemical bundle test. The flow visualization results showed a clear improvement for the new design, but this was primarily a qualitative assessment. A bundle test was run to high current densities to induce fuel depletion effects in the outlet substrate (tube 6 in Figure 14). The good correlation with the electrochemical model developed around single-cell and 5-cell test articles having very uniform distribution provides additional evidence of the flow uniformity achieved in the epsilon bundle.

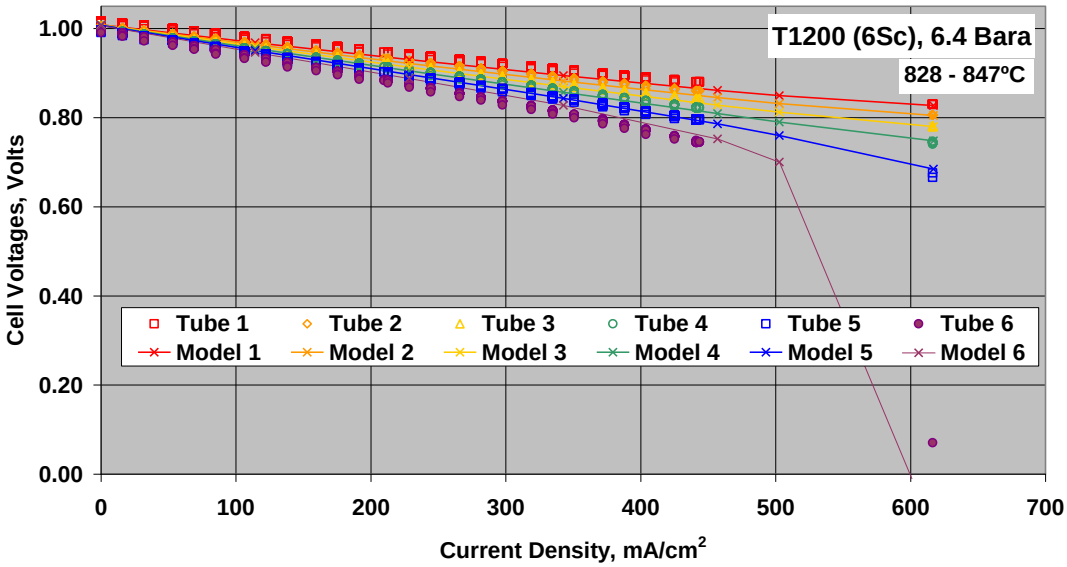

Figure 14. VI curve from bundle with substrate outlet orifice plate

The fuel into and out of the 12-bundle strips occurs at the top of the strip. In the pre-SECA design, this arrangement tended to benefit the bundles at the top of the strip, because these are located closer to the fuel supply and would receive more fuel than the ones situated further away. With the aim of achieving a better bundle-to-bundle distribution within a strip, the inlet manifolds were similarly amended as the outlet manifolds for pressure drop management bundle-to-bundle within the strip – separate components were bonded between the inlet manifolds and substrate 1 inlet. As shown in Figure 15, the bundle-to-bundle flow distribution of ±3% about the mean flow for each bundle. Some experiments were performed to validate the CFD estimates experimentally using gas chromatography and analysis of transient times for gas injections/flows. This provided some collaboration of the selected design.

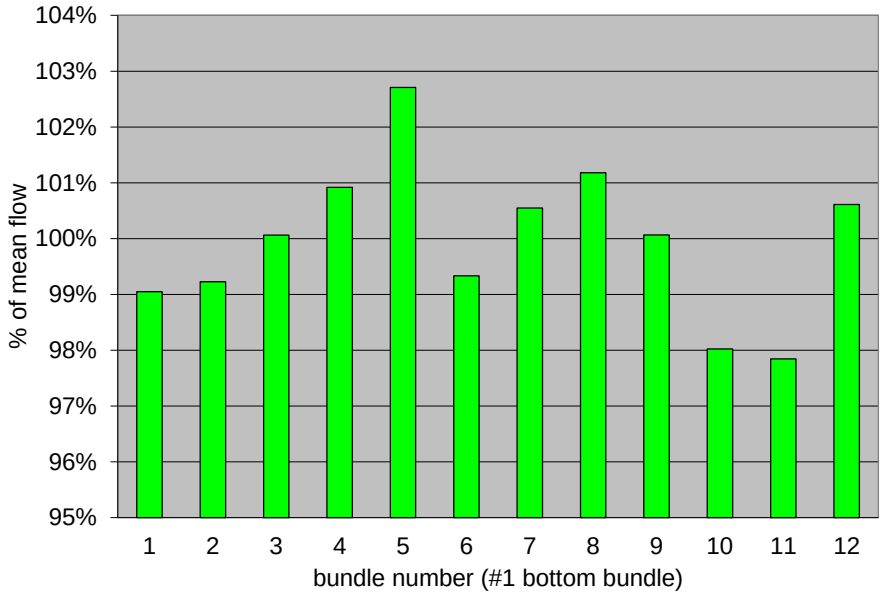

Figure 15. CFD comparison bundle-bundle fuel distribution in a strip

Strip component redesign – Stage 2: The interim design changes chosen for Stage 1 was not suitable for scale-up to large production volumes. The main issue was the new components added between the manifolds and the tube to control pressure drop created additional manufacturing components and also caused unique pressure drops for 7 of the 12 bundles and thus unique bundles to be tracked during production and assembly. The primary design change for Stage 2 was an increase in the cross sectional area of the fuel pipes providing the fuel into and out of the 12 in-parallel bundles. The lower pressure drop through the fuel pipes was the key design change that allowed common bundle designs with uniform pressure drops and this simplified strip assembly and inventory control. The lower pressure drop through the fuel pipe also allowed/required the increase of pressure drop within the bundles, and this was achieved by minor design changes to the pressed end-cap designs. The pressure drop of the manifolds was also optimized, maintaining the basic overall geometry, but with the fuel-pipe to manifold socket area suitably increased. With these changes, the bundle-to-bundle flow distribution predicted by CFD (Figure 16) was a minimum of 98% of the mean flow. The minimum channel flow of the outlet substrate across all bundles is estimated at 97.7% for bundle position 1 (bottom bundle within the strip). The fuel distributions can be combined to give a worse cast scenario for the strip within bundle 3 at ~95% of the mean flow. Supply of the Stage 2 redesigned components was in time for the Phase 2B block build.

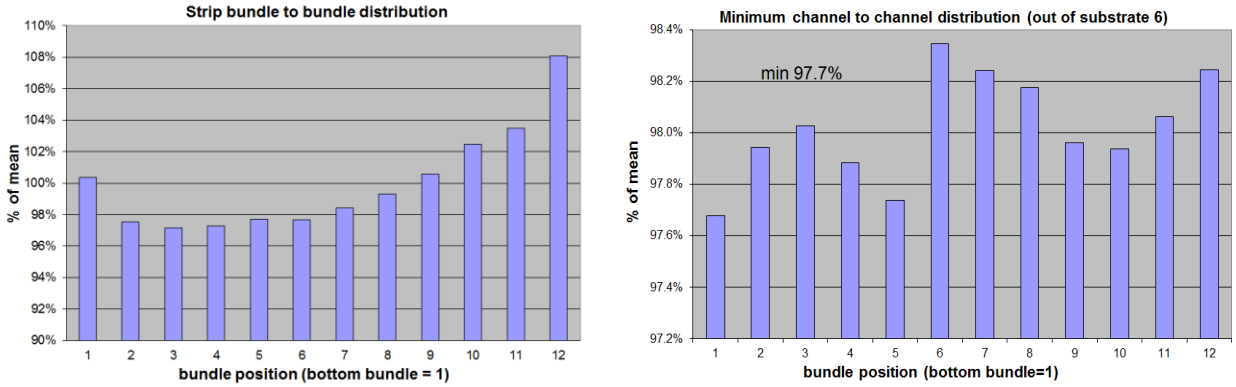

Figure 16. Bundle-to-bundle and minimum channel-to-channel flow distributions for the Stage 2 strip redesign

Tube Specification Development: Key requirements for the substrate are the thermal expansion appropriately matched to the printed layers, sufficient permeability for reactant fuel and product diffusional transport, mechanical properties to provide a structurally reliable fuel cell stack and the ability to fabricate at an appropriate cost that will support commercialization. As described in the subsequent section of the report, the $MgO+MgAl_2O_4$ substrate exhibits favorable strength and Weibull properties and the dual-phase nature of the material allows tailoring of the thermal expansion by adjustment of the volume fraction of the low and high CTE phases. Thermodynamic calculations by NASA Glenn Research Center under the range of fuel reformate composition and representative temperature and pressure conditions have predicted low volatility for species from the substrate. Testing and analysis to date supports the specification of MMA as a suitable substrate material.

During the Phase 1 period of the program LGFCS established a more fundamental understanding of the permeability requirement of the substrate. Prior to the SECA program, the porous structure of the substrate was specified by an overall porosity and mean pore radius. The specification for the substrate's microstructure is now given by a permeability factor (an outcome of the theoretical governing equations

for multicomponent diffusive flow through a porous medium) of porosity/tortuosity^2 (ε/τ^2) and the mean pore radius, with the permeability factor being the dominant specification given the typical pore sizes of the substrate (Knudsen flow can be ignored). An insufficient permeability can result in high levels of steam at the exterior surface of the substrate arising from differences in the diffusion resistance of reactant and product species across the substrate thickness. Local elevated steam levels, especially at high temperatures and bundle outlet fuel compositions can create conditions for accelerated volatility of $Ni(OH)_2$ from the anode layers since its partial pressure is proportional to p^2_{H2O}/p_{H2} and a tube of insufficient permeability will drive this ratio to high values at the substrate exterior during fuel cell operation. LGFCS has developed an electrochemical model, validated experimentally, that uses a theory for multi-component diffusive flow through a porous substrate to predict ASR and provides guidance on substrate permeability requirements to minimize diffusion resistance and the p^2_{H2O}/p_{H2} ratio. The model results of Figure 17 at bundle outlet conditions (80% system fuel utilization) shows that at the nominal current density (~400 mA/cm^2) for the LGFCS system a permeability factor of (ε/τ^2) greater than 0.035 can minimize diffusional resistance and there is diminishing returns for ASR levels for (ε/τ^2) exceeding 0.06. Based on such analyses, LGFCS has refined its tube specification to include a permeability factor of 0.05±0.005.

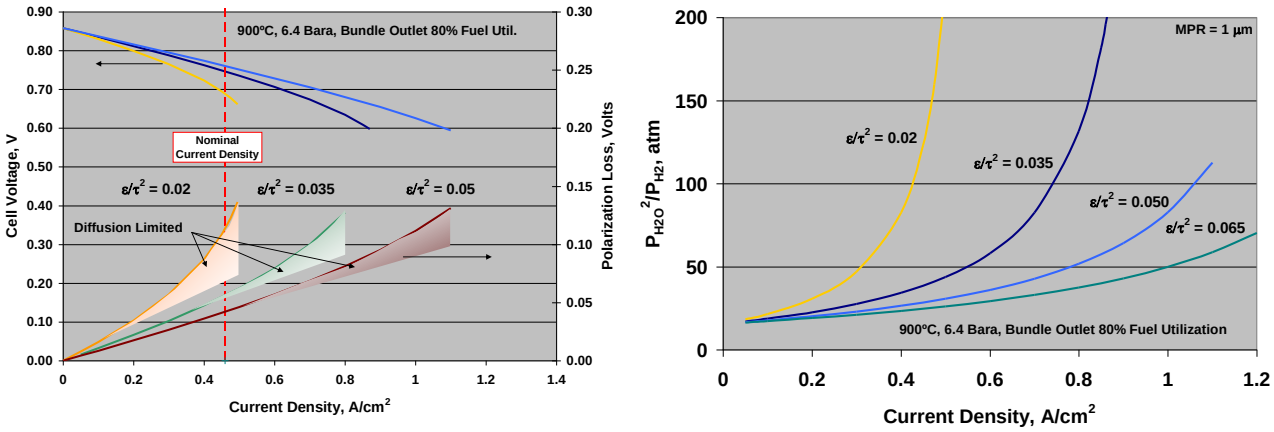

Figure 17. Cell VI, diffusion resistance, p^2_{H2O}/p_{H2} versus permeability and current density

Another reason for not pushing to overly high permeability factors is to conserve strength of the substrate for structural reliability considerations. The primary substrate vendor has consistently met the 0.05±0.005 permeability specification and the >29 MPa strength specification over more than 10,000 substrates. An alternate substrate vendor (as potential secondary source for supply security) has also shown an ability to meet the combined permeability and strength specification.

Finite element stress analysis: Insuring the structural reliability of the all-ceramic strip is critical for commercial introduction and success. LGFCS has supported stress analysis of system components, including the ceramic SOFC strip, through its internally funded development program. This program's Phase 2B effort has addressed the accuracy and validation of the FEA tools, as the material property data for those models has been generated in part by the mechanical testing under this program. It is important to have confidence in the stress analysis predictions generated for strips under system operating conditions (steady-state through transient). LGFCS has taken the approach of validating the FEA predictions by starting at simple components (bare substrates) under a controlled 4-point flexure stress and working up to ever more complicated SOFC structures and loading conditions to compare the experimental load, strains, displacements to the model estimates. Figure 18 shows the similarity in the FEA predicted failure stresses and the K_{max} (maximum load/center point deflection) for bare tubes, fully glassed tubes (to assess residual stress assumptions) and printed tubes – values all within ±10%. Note that deflection measurements were unable to be obtained for the 850C tests. In parallel with the validation

activities, validation of the CARES modeling was performed. The 63.2% probability of failure was matched for the FEA+CARES analysis build upon the Weibull data input for the bare substrate. We now have confidence to perform analysis of larger scale cases (bundles and strips) at various boundary conditions to predict probability of failures. The multiphysics bundle/test stand models can be used to identify extreme thermal boundary conditions generated by reduced air flow and high current density to lead to high stresses and test the predictive nature of the FEA/CARES analysis.

Bare Substrate

	Experimental		FE Model		Ratios (Exp./FE)	
	Failure stress (MPa)	Kmax (N-mm)	*Failure Stress (MPa)	Kmax (N-mm)	Failure Stress (MPa)	Kmax (N-mm)
Room Temp.	41.5 (from lot 45-80)	1804±151	41.55	1777.6	0.99	1.01
Elevated Temp. (850C)	55.7 (from lot 61 only)	--	51	2171.6	1.08	--

Glassed Substrate (~120 micron thick glass)

	Experimental		FE Model		Ratios (Exp./FE)	
	Failure stress (MPa)	Kmax (N-mm)	*Failure Stress (MPa)	Kmax (N-mm)	Failure Stress (MPa)	Kmax (N-mm)
Room Temp.	46.3 (from lot 65 only)	1831±45	48.33	2102.5	0.96	0.87
Elevated Temp. (850C)	69.2 (from lot 65 only)	--	53.35	2537.6	1.3	--

Printed Substrate

	Experimental		FE Model		Ratios (Exp./FE)	
	Failure Stress (MPa)	Kmax (N-mm)	*Failure Stress (MPa)	Kmax (N-mm)	Failure Stress (MPa)	Kmax (N-mm)
Room Temp	57 (from lot 46 only)	2504±234	55.97	2726.5	1.02	0.92
Elevated Temp. (850C)	74.5 (from lot 45 and 49 only)	--	77.87	3628.3	0.96	--

Figure 18. Comparison in failure stress and K_{max} predictions versus experimentation for bare and printed tubes at root temp. and 850C

Conclusion: Two stages of strip redesign were performed to achieve improved flow distribution throughout the strips. The first redesign provided components for the Phase 1 and Phase 2 metric tests, whereas the latest redesign supported the fabrication of strips for the Phase 2B block test. Uniform flow distribution is important for running blocks at high design point utilization to meet efficiency targets and avoiding high cell degradation that can occur if there were localized regions of fuel starvation. The tube permeability spec was also matured during the program to likewise affect the ability to run at high fuel utilization. The program supported the generation of mechanical properties as input into finite element analysis and confirmed that the finite element analysis matches well the experimental results for first-stage validation exercises. Specified substrate mechanical properties are met at the permeability requirements.

Task 3.2 - Substrate Reliability

Approach – Detailed mechanical property characterization of the substrate has been performed by Oakridge National Laboratory (ORNL) and LGFCS through a CRADA. Characterizations include strength, modulus, fracture toughness, creep and slow crack growth of the initial and a next generation substrate from the primary LGFCS substrate supplier. The Gen2 substrate offer cost reductions at high volumes as a result of material and processing changes including: tunnel versus batch firing, lower purity raw material and fewer machining steps. Quality improvements are also realized based on improved uniformity of extrusion feedstock that reduces the occurrence of elongated pores observed in Gen1 tubes. In addition to the substrate, mechanical properties of the dense ceramic manifold components, the glass-ceramic based joints with the dense ceramics and the active layer cell materials have been measured. These measurements are important as inputs into stress finite element analysis.

Results and Discussion – At the start of the program there was considerable experience with the MgO-$MgAl_2O_4$ (MMA) substrate and dense fuel distribution components through several years of internally funded SOFC development including build and testing up to 100kW-scale test articles. The limited database for the MMA provided confidence in its use during the earlier development program, but it was realized that more detailed understanding of the materials was required to gain confidence in the long-term reliability of SOFC components fabricated from the MMA. The following describes the understanding of the MMA material, the glass-ceramic joints and the active layer materials gained throughout this program and the impact on designing for reliability.

Basic MMA Properties: ORNL has performed some basic material property measurements for the substrate from the new vendor selected around the start time of the project. The Gen1 substrate material from that vendor shows an increase in strength at temperature (Figure 19), similar as observed for an earlier substrate supplied to LGFCS indicating a representative feature of the MMA. The strength increase from room temperature to 800-950C is from 42.3 to 50 MPa (18% increase) for 4-point flexure samples extracted for the edges of substrates; a strength increase of ~30% has been observed for Gen2 substrates (full substrate testing). The fracture toughness of the porous substrate also increases with temperature, and a similar increase in the strain energy release rate versus temperature provides evidence that the increased toughness is real and not an artifact of the higher elastic modulus with temperature that exists with this material. The microcracking results from the thermal expansion mismatch and grain differences of the MgO and $MgAl_2O_4$ phases.

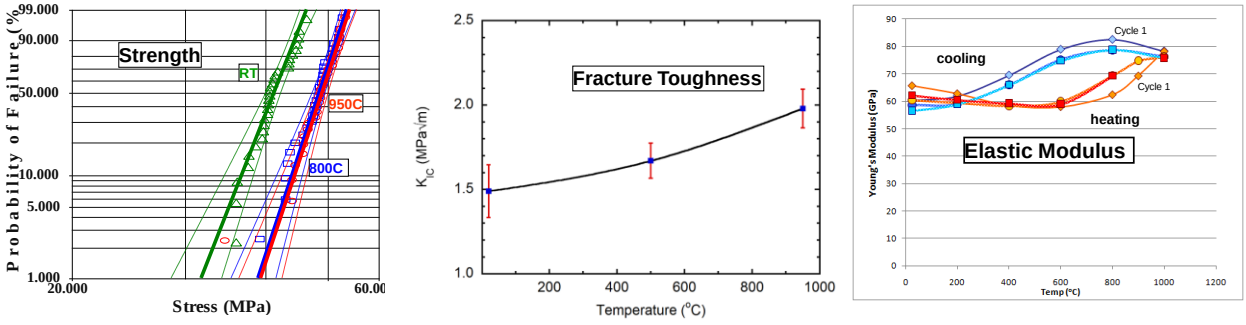

Figure 19. Strength and fracture toughness of Gen1 substrate material

The reliability of ceramic components/structures depends critically on the uniformity in the quality of ceramic components since the strength is a function of flaws, defect sizes. The strength specification for the substrate is a room temperature 4-point strength of a full-scale substrate test article of >29 MPa (based on modulus of rupture at 63.2% probability of failure) and a Weibull modulus over 15. The

Weibull plots in Figure 20 show the good consistency in the strength properties of both the Gen1 and Gen2 tubes over multiple lots of tubes. The Gen2 substrates have a slightly higher allowance for CaO and silica content, but electrochemical durability testing has shown no adverse impact on the power degradation rate. To insure high quality of substrates entering the printing line, absent any specified processing defects, LGFCS has adopted a 100% x-ray inspection protocol for incoming tubes. This requirement arose from a period during 2011 in which extrusion defects were prevalent in substrates, and which caused a delay in the fabrication of the strips for the Phase 1 and Phase 2 test. The vendor resolved the processing issue, and for a recent order of 10,000 substrates by LGFCs there has been a yield loss from x-ray inspection of only 1% for all unacceptable defect populations.

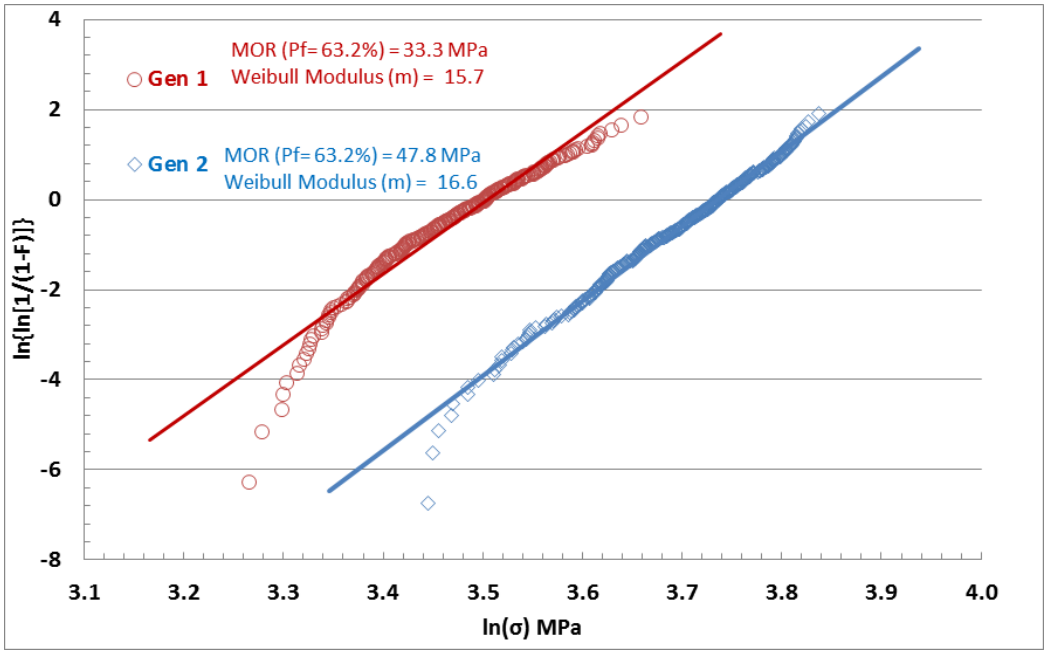

Figure 20. Weibull strength distribution comparison of Gen1 and Gen2

The room temperature Weibull characteristic strength (63.2% probability of failure) of the dense MMA of the strip fuel distribution components is ~240MPa and has room temperature and 900C fracture toughness of ~3.7 MPa$\sqrt{m}$ (little change with temperature) , both substantially higher than that of the of the porous MMA substrate, and thus the detailed mechanical characterization has emphasized the substrate. The finer microstructure results in a material that doesn't show microcracking tendency with the elastic modulus decreasing slightly from 275 GPa to 250 GPa from room temperature to 800C.

Slow Crack Growth Properties: LGFCS considers both infant mortality and lifetime reliability. Infant mortality is related to fast fracture of components caused by a component/structure design unable to withstand stress levels arising during normal operating conditions or transient/upset operating conditions. Thorough stress analysis including Weibull/CARES of the designs under the full range of boundary condition imposed by the steady-state and transient operating modes can insure a given probability against infant mortality events for given stress levels and material properties. The more difficult aspect of reliability prediction involves time-dependent mechanisms that reduce the mechanical properties of the ceramics. Of particular interest is the slow crack growth (SCG) behavior of the substrate under the moist fuel environment as it is well known that ionic oxide ceramics can be very susceptible to this time-dependent failure mechanism. Slow crack growth can lead to extension of flaws to the point at which they lead to fracture of the component under the applied stress state. ORNL has experience in SCG

testing of porous ceramics has developed an initial database for the MgO-$MgAl_2O_4$ substrate under several environments:

- Air (room temp., 900C)
- 3.5% H_2O, 3.5% H_2, 93% N_2 (800C, 900C)
- 48.5% H_2O, 1.5% H_2, 50% N_2 (800C, 900C)
- 48.5% H_2O + air (800C, 900C)

SCG measurements are performed using a double cantilever specimen and measuring load relaxation during crack growth. Reduction of the data results in plots of crack velocity versus the applied stress intensity per the relationship $v=AK_I^n$. The higher the slow crack growth exponent n, the less susceptible is the material to crack growth, and the preference is for a material with a high critical stress intensity factor (i.e., fracture toughness) such that the SCG exponential curves are shifted to high a stress intensity allowing component design to be at as low a fractional stress intensity as possible. The general SCG data for ceramics falls into 3 regions as shown in Figure 21. Region I is a threshold, region II is linear and region III enters instability and fast fracture.

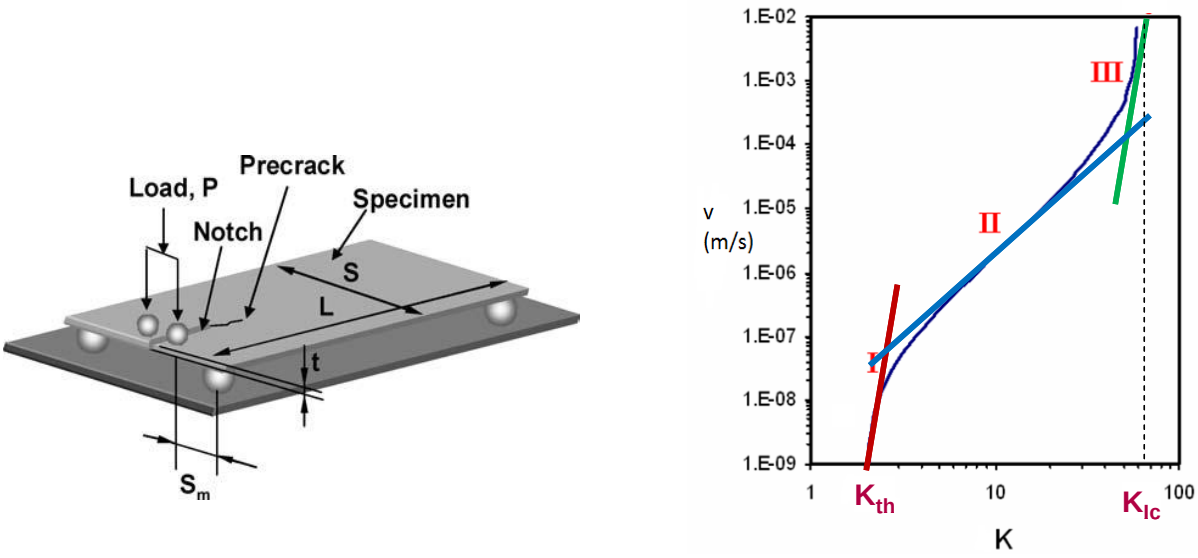

Figure 21. ORNL test specimen for SCG and theoretical regions of slow crack growth of ceramics

The most pertinent SCG tests performed thus far are under the 48.5% H_2O, 1.5% H_2, 50% N_2 (800C, 900C) condition as this is a low oxygen partial pressure and at a moisture level ~50% representative of that present at the outlet of LGFCS stacks (Figure 22). The SCG exponent "n" from the regression is 36 at 900C versus a value of >100 at room temperature. An "n" value of 36 is moderate for a ceramic, but what is quite encouraging is some evidence of a threshold at ~1.6 MPa$\sqrt{m}$. Further testing will be performed after this program under actual reformate fuel compositions and the range of block operating temperatures to investigate the SCG threshold stress intensity for the porous MMA substrate material. The importance of a threshold at a high percentage of the critical stress intensity (fracture toughness) means that components could be designed well below stress levels where slow crack thus avoiding a life limiting strength degradation mechanism. As the 850C unit volume (mm^3) characteristic strength at a low probability of failure of just 0.02% is in the range of 49 MPa and with the threshold: K_{Ic} at ~0.72 this implies a high allowable stress for the design.

Limited SCG testing has performed for the dense MMA, but a value of 38 for the SCG exponent was measured at 900C in air. The higher strength and fracture toughness of the dense MMA means that at design stress levels the actual crack velocities for slow crack growth will be very low, even assuming no threshold.

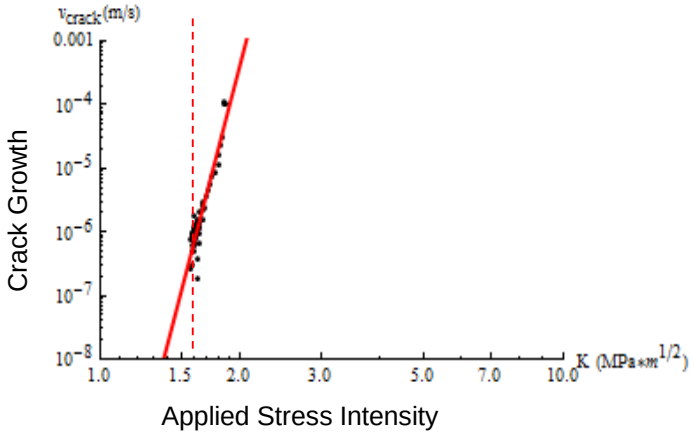

Figure 22. SCG behavior of substrate in 48.5% H_2O, 1.5% H_2, 50% N_2 (900C)

The SCG measurement technique by ORNL requires specially prepared specimens and pre-notching that is not typical of the substrates put into service. LGFCS has investigated an alternate technique to obtain SCG data by an ASTM technique (ASTM C1368-10) based on taking ceramic article to fracture under a range of constant stress rates. Lower strengths are obtained for low stress rates since slow crack growth can occur during the loading of the specimens. Figure 23 shows a typical result obtained for room temperature SCG in air by 4-point flexure testing (n=61); a similar value of "n" is obtained as that by the ORNL technique (3 tests with n average of 43).

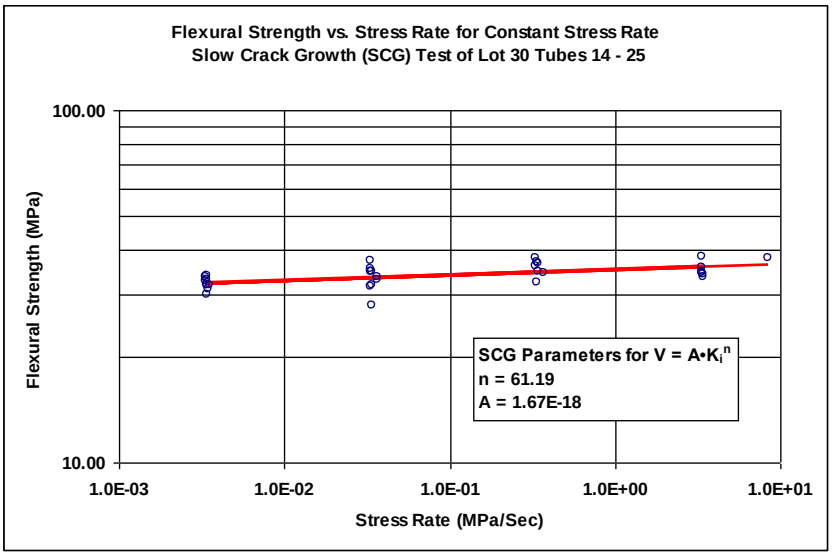

Figure 23. SCG parameters obtained at room temp. by ASTM technique of constant stress rate

RRFCS and ORNL have worked to develop a methodology for lifetime prediction built upon the fundamentals of fracture mechanics combined SCG versus stress intensity relations with the Weibull statistics for the substrate at the SOFC operational temperatures. An equation is thus available that allows a time to failure predictions as a function of the substrate properties (SCG, Weibull strength and fracture toughness) and dependent on the volume of material under stress in the article, the design stress of the article and the desired probability of failure. Estimates of the time to failure can be made as shown in Figure 24 for illustrative purposes only. The reliability of the MMA substrate is most influenced by the SCG exponent (n), the Weibull modulus (the higher the better for both) and through designs that minimize the operational stresses on the tubes. LGFCS is seeking sufficient stack reliability for 5 year life.

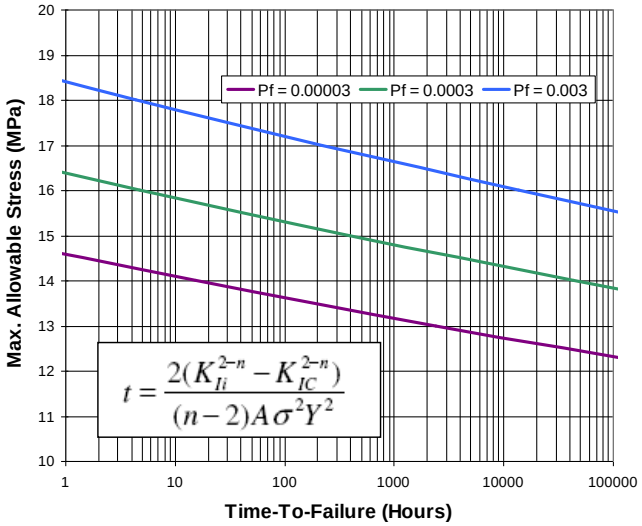

Figure 24. Illustration of substrate lifetime prediction being explored based on SCG mechanism

Validation of the reliability predictions methodology has been first pursued doing simple flexure testing of substrates in air. We find that the samples last 3-4 orders of magnitude longer than expected indicating some flaws in our methodology, but we also see that failures can be generated at 90% of failure loads in reasonable times, but at 85% of failure loads, failures just have not occurred. ORNL also did not experience failures in their 900C/air attempts at SCG validation. This may indicate the presence of a threshold stress intensity factor at play. An interesting yet unexplained result is that the strength of the substrate following the SCG testing in which SCG failure did not occur exhibiting statistically significant difference in strength. The strength increase varied with the temperature of the SCG test and the level of stress applied during the test. We will continue to investigate this feature of the material.

The other time-dependent failure mechanism being examined is creep/creep rupture. ORNL has performed limited creep testing of the substrate material. The testing to date does not suggest that creep is a factor for the material at the 800-900C operating temperatures.

Active layer property determination: The integrity of the active cell layers printed on the substrate is also very important to the reliability of the stack and system. The fuel-air boundary is a ~10 micron electrolyte held onto the substrate by the anode-side layers. Accurate elastic properties and thermal expansion of the active cell layers is required for FEA analysis. ORNL initially measured elastic properties from bulk specimens but it was determined that in-situ properties are most preferred. ORNL developed a technique of obtaining elastic properties by extracting a 175 micron section of substrate from a series of samples provided by LGFCS in which the SOFC was printed/fired up to each layer (Figure 25). The thin multilayer samples were tested in a micro-tensile machine. The progression in the measured elastic

properties for sequential layers can be deconvoluted to yield the elastic properties of an individual layer (Figure 25). ORNL finds some non-linearity in the stress-strain curves but that the initial modulus from the stress strain curve is a fairly close match to the modulus determined by the Resonance Ultrasound Spectroscopy (RUS) technique.

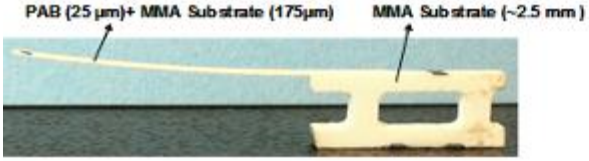

Test #	Active Layer	E (microbeam bending) (GPa)	E (microbeam bending) (GPa) using initial data points at the origin	E (nano-indentation) (GPa)	E (bulk RUS) (GPa)
A	Substrate	52.1	72.2	250.83	72.0
B	PAB	58.98	49.2	63.35	
C	ACC	52.6	102.4	--	
D	Anode	129.74	63.31	66.52	98/193
E	Electrolyte	422.6	224.38	69.84	
F	Cathode	87.67	124.25	43.58	143
G	CCC	73.96	99.14	43.49	129

Figure 25. ORNL technique and results for layer elastic property determination.

Glass-ceramic Joint Strengths: Towards the end of the program ORNL began some initial characterization of the strength of the joint formed between dense MMA components using a glass-ceramic sealant. Figure 26 shows the location of joints formed between adjacent dense MMA end-caps and/or manifolds, where the joints are formed using a glass-ceramic sealant, the same as that used to seal the inactive regions of the porous substrate support. ORNL has performed room temperature tests of as-fabricated joints and joints following 4000 hours of testing within a bundle. High quality test data has been obtained per an ASTM procedure. As fabricated joints have strengths of 15.8 ± 2.4 MPa and the 4000 hours exposed joints have a strength of 19.7 ± 3.2 MPa at room temperature, but these strengths are expected to be low given the residual stress arising from the CTE and elastic modulus differences. As-fabricated joints show a shear strength of ~40 MPa at 850C but with a high degree of scatter. The stress state of the joint is low at operating conditions and the worst stress state is sitting at room temperature from the residual stresses. LGFCS has not observed failure of joints during operation but has seen occasional joint failures for assembling strip components. Further optimization of the glass CTE is planned to minimize residual stresses in as-manufactured strips and sub-assemblies to avoid yield losses. Strip joint designs and component and material specifications are also planned to be optimized to favor compressive residual stresses on the joints.

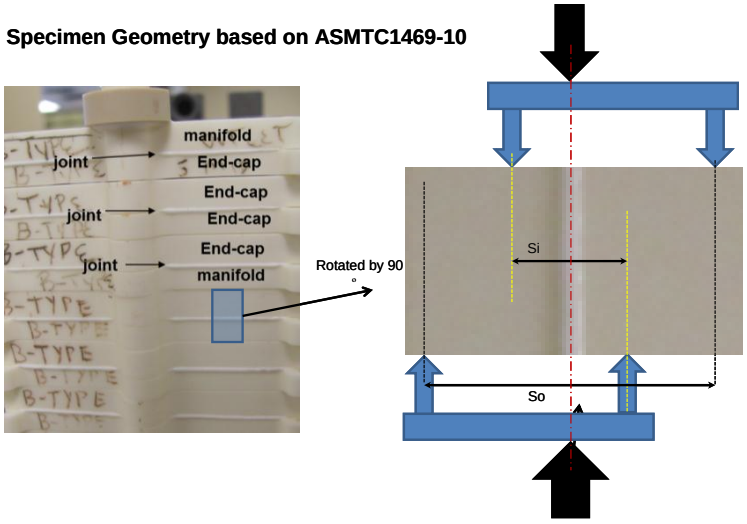

Figure 26. Approach for shear testing of joints

Conclusion – Given that roughly 15,000 active substrates will constitute a 1MW system, a detailed understanding of substrate mechanical properties is necessary to ensure long-term structural reliability of the SOFC modules. Data generated thus far on the ORNL FWP/CRADA supports the selection of MgO-$MgAl_2O_4$ (MMA)as a suitable substrate material, and in fact the MMA shows very encouraging SCG resistance in simulated fuel environments – future testing will include actual reformate environments. LGFCS has been emphasizing the mechanical characterization of the porous substrate material since it is the lowest strength ceramic component within the strip and constitutes the greatest volume of ceramic within the strip. The dense MMA have strengths ~ 4X that of the substrate and do not represent a strength and reliability risk at operating conditions. As the block operating temperature is only ~200C lower than the glassing temperature for the joint, the residual stresses on the joints during operation is low and also do not pose a reliability risk.

The program has provided a foundational database of the mechanical properties of the strip component materials that provides a high level of confidence in the basic strip technology and the ability to design for reliability. The database will be expanded beyond this program to gain a more detailed understanding of the properties and micromechanics of the materials, in particular the unique properties observed for the microcracked substrate material. Understanding the slow crack growth time dependent failure mechanisms for all materials within the strip, and their threshold levels, is important for developing a life prediction methodology. Equally important is the measurement of residual properties of the strip components following long-term testing.

Task 3.2.2 - Substrate Sealant Development

Approach – The objective of this task is to develop a new, or select a pre-existing glass ceramic to be used to seal the inactive area of potential future higher thermal expansion substrates and for bonding these substrates to similar expansion dense fuel manifold components. LGFCS has collaborating with PNNL on this task through a FWP. Detailed studies of the long-term stability with the substrate is performed using x-ray diffraction and SEM/EDS analysis. Higher CTE substrates (by adjusting the MgO content) are of interest for future stages of cell/stack technology for allowing the evaluation and potential qualification of higher CTE active layer materials to boost performance and long-term durability.

Results and Discussion – A small activity was funded during Phase 1 for PNNL to select 6 glasses from its data bank of sealant compositions they have examined over the years as potentially suitable for the LGFCS application. The best candidates for the CTE range of interest were within the YSO family (Y_2O_3-SrO-CaO-B_2O_3-SiO_2). Two compositions exhibited the most favorable wetting characteristics. Both glass-ceramics showed minimal reactivity with the substrate, and the interface chemical profile for the YSO12 sealant is shown in Figure 27. The selected YSO compositions exhibited rapid crystallization and one glass exhibited poor overall density, attributed to the rapid crystallization kinetics. Further investigations of the applicability of the YSO glass-ceramics to the LGFCS substrate is required, but this relatively small FWP at PNNL has shown initial promise for use with higher CTE substrates.

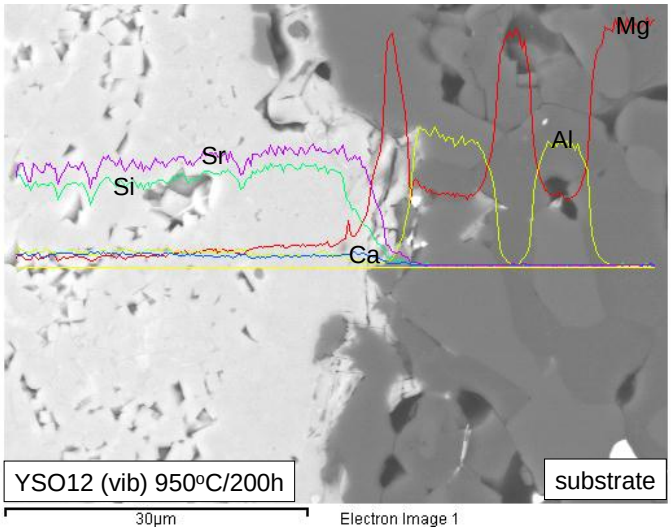

Figure 27. Chemical profile across YSO12 and substrate interface following 950C/200 hour aging

During Phase 2 the sealant studies emphasized investigations of the baseline LGFCS sealant glasses and minor modifications to increase the thermal expansion. Evolution of the glass-ceramic crystallinity and the CTE was studied over several firing cycles to match cycles during substrate sealing and throughout interconnect application and strip build, and accounting for repair firings as might be necessary. Depending on temperature of the firing, the phases and CTE did not lock in until several firing cycles (Figure 28).

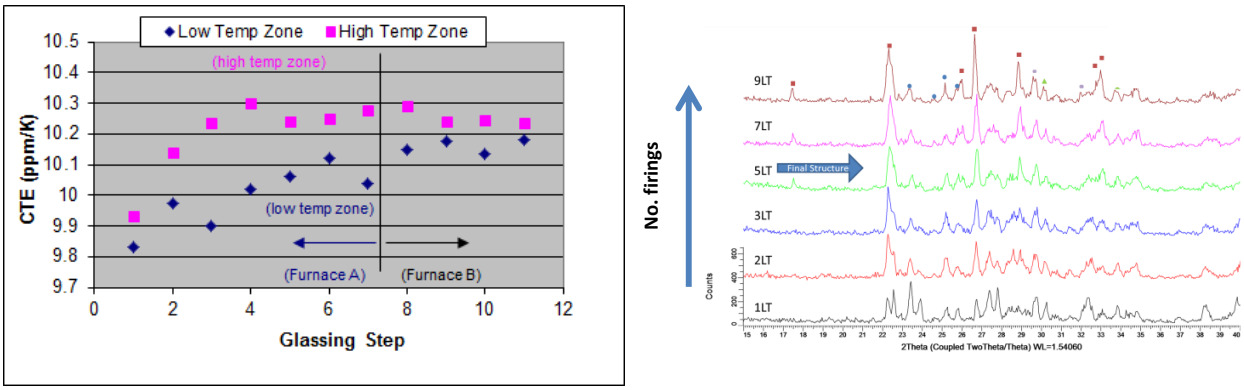

Figure 28. Evolution of phases and CTE for baseline sealant

Modification to the glass and ink were made to affect the CTE on the initial glass firing cycle. It was determined that a minor 1% addition of a selected phase was able to achieve a marked increase of ~0.5 ppm/K in the glass with minor effect on the flow characteristics of the glass (Figure 29). Additions over 2% had a very significant impact on viscous flow.

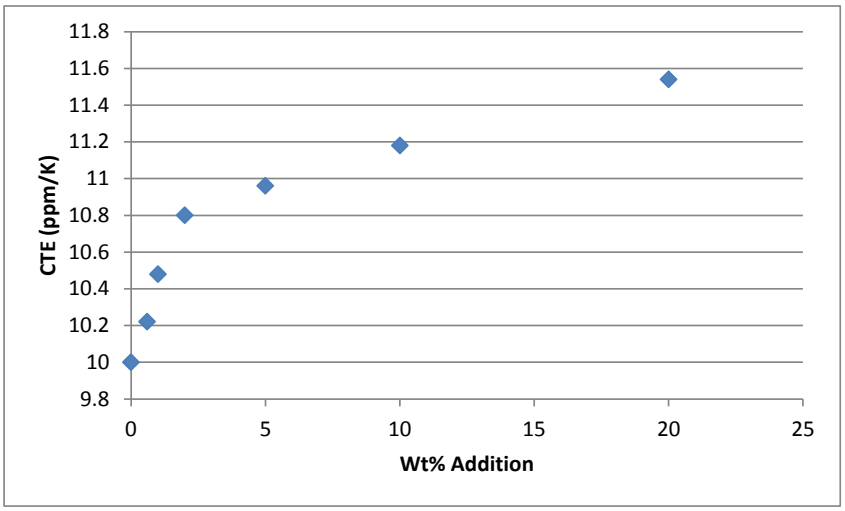

Figure 29. Impact of minor phase addition on CTE of crystallized glass-ceramic sealant

Conclusion – LGFCS' current glass-ceramic composition has been tested as sealant and joining material for a maximum of roughly 16,000 hours at representative block temperatures without issue, meaning no occurrence of sealant or joint failure. As ultimate stack lifetimes of 40,000 hours are required further understanding of the evolution of the baseline glass-ceramic CTE and phase composition is required. The detailed XRD and TEM analysis by Case Western Reserve University for sealant tested to 12000 hours provides confidence in the glass-ceramic for baseline cell/stack technology. As reported in the Cell Development subtasks, there is promising next-generation cell technology of somewhat higher thermal expansion (single layer anodes, nickelate cathodes). For high manufacturing yields, avoidance of electrolyte cracking and layer delamination, slight adjustment in the CTE of the substrates have to be made. Along with the substrate CTE changes, some adjustment of the CTE of the glass-ceramic sealant/joining glass is expected. Promising approaches for slightly modifying the baseline glass-ceramic have been demonstrated. LGFCS also continues to evaluate alternate glass-ceramic technologies from other glass vendors as part of its supply-chain activity; these vendors are options for next generation stack technology with the slightly altered CTE requirements. Multiple vendors have promising glasses showing potential for meeting CTE and flow requirements.

4.0 CELL DEVELOPMENT

During the Phase 1 program, the cell development objectives were to demonstrate performance levels (ASR) and costs suitable for an entry into service technology and to improve degradation rates sufficient to meet SECA degradation target levels and to advance the durability to levels required for initial products. During Phase 1 LGFCS completed the reduction to practice of the 60-cell pitch design which has been instrumental in lowering the ASR for the LGFCS integrated planar technology (60-cell was designed and first demonstrated prior to the SECA program). The earlier technology was a 30-cell pitch design, in which the larger cell pitch and longer cell-to-cell interconnection distance contributed to an overall higher ASR from ohmic losses through the current collecting layers and primary interconnect. The 30-cell design relied in part on precious metal conduction layers to minimize the ohmic resistances. In the 60-cell pitch design, both the interconnect length and cell pitch were reduced by ~50%, and when combined with the lower substrate current (similar current density over smaller active area) achieved a markedly lower ASR while also allowing the use of low-cost materials with lower conductivity. Accomplishments for the specific cell layers are highlighted in the following subtask sections.

The progression in the cell performance is shown in Figure 30 for single cells (no primary, cell-to-cell interconnection) tested at atmospheric pressure. Alpha technology is the pre-SECA 30-cell pitch technology with the higher cost active cell layers and epsilon-minus is the pre-SECA initial 60-cell pitch results using the lower cost cell materials. The epsilon technology that is included in the Phase 1 metric tests has a lower ASR from the adoption of a ScSZ electrolyte. Epsilon-plus technology represents an optimized LSM-based cathode formulation, and the 1 bar and 6.4 bar data shows the ~0.05 ohm-cm^2 average performance improvement achieve with pressurized operation. The zeta technology shown in the graph includes benefits from the MEIC nickelate cathode, and is a longer-term cell technology candidate for commercially mature SOFC products.

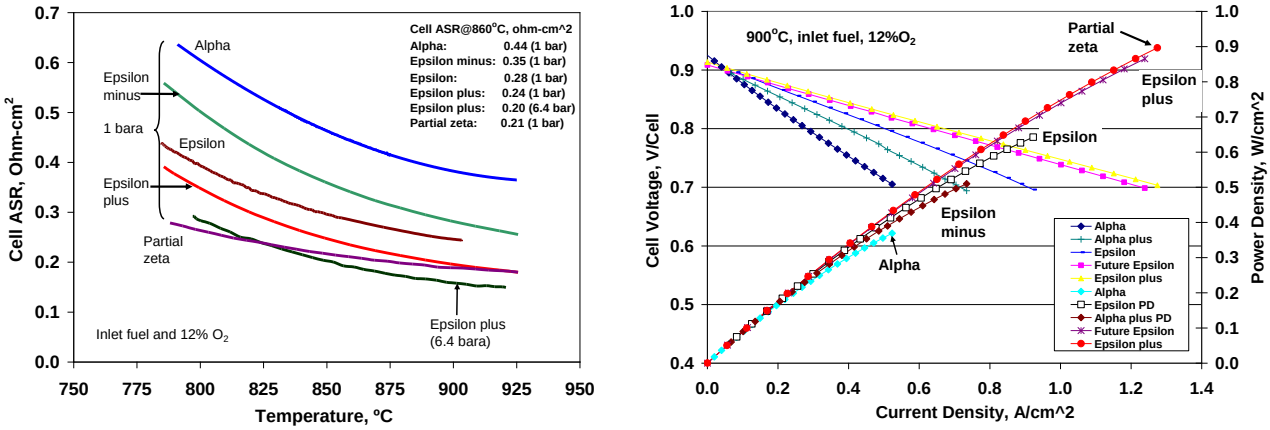

Figure 30. Cell performance improvement during the Phase 1 program

Task 4.1 - Interconnect Development

Approach – In the RRFCS technology, the primary interconnect (PIC) connects two adjacent cells to form the integrated planar (IP) SOFC design on a porous ceramic substrate. Interconnect materials must meet the following requirements: dense/impermeable, conductive, exhibit chemical compatibility with adjacent fuel cell materials, stable in both reducing and oxidizing environment, and exhibit long term stability under fuel cell operating conditions. In the IP-SOFC technology, unique designs within the PIC region facilitate meeting the above requirements. A via design is preferred for the PIC to minimize stack cost while continuing to use a precious metal cermet. By implementing electronic packaging design features within the IP-SOFC, the combination of vias and dense ceramic layers can improve the gas tightness of the PIC area, thus maintaining high fuel utilization. The current baseline interconnect is a precious metal cermet, in via form, selected based on its low ASR contribution. Refinement of this baseline approach addresses maintaining low resistance interfaces between the via and the Ni-based active anode materials and optimizing the PIC materials and designs to avoid fuel loss.

Ceramic-based primary interconnects are being developed as the next generation primary interconnect to achieve further cost reductions and improved long-term durability for 4-5 year service lifetimes. The greatest challenge to adopting a ceramic-based interconnect is achieving sufficient density in a constrained sintering condition. Dilatometry is used to study ceramic interconnect sintering and densification. Dry pressed bar and printed films coupons are used to evaluate ceramic interconnect conductivity in both air and forming gas in the furnace with controlled oxygen partial pressures. SEM and EDS are used for routine post-test analysis for microstructure change and materials migration during long term durability test. In addition to single layer interconnects of chromites and other perovskites, alternate designs, such as bi-layers of n-type and p-type conductors are being explored.

Results and Discussion - Precious metal based cermet via designs had already been demonstrated pre-SECA to deliver the required ASR levels, but long-term durability was inadequate. Post-test analysis revealed the presence of a significant degradation mechanism within the PIC region related to materials interdiffusion issues that routinely limited lifetimes to <2000 hours, as shown in Fig.1. This subtask has been very successful during Phase 1 with the selection of a new precious-metal cermet primary interconnect design and materials set that overcame this degradation mechanism. On-going durability testing continues to validate the design solution out to longer test times, but Figure 31 shows the improvements achieved through 8,000 hours of testing. The alignment of cell layers within the PIC region is important for maintaining long-term stability and screen patterns have been altered to insure this requirement.

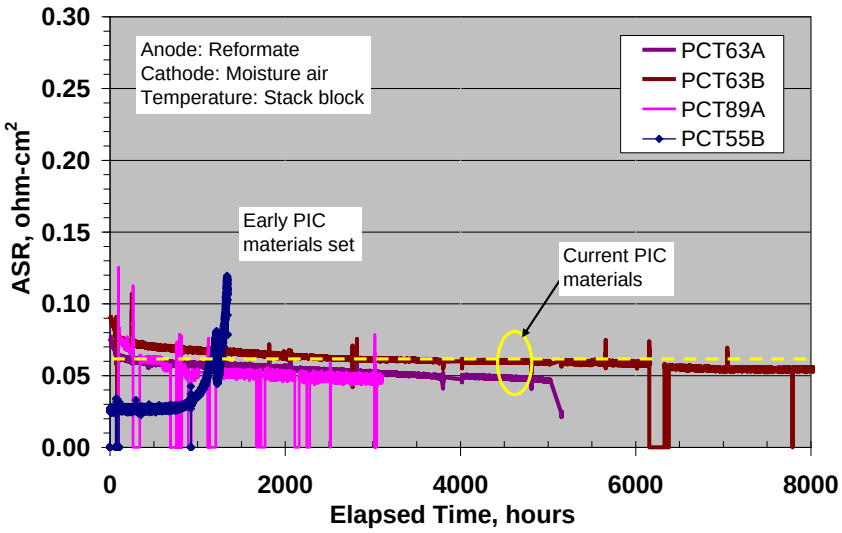

Figure 31. Primary interconnect (PIC) ASR long-term trends to date (precious metal via design)

During Phase 2, durability test of new selected precious metal cermet PIC materials and design continues. 5-cell subscale tests had been tested for 16,000 hrs at 860°C (PCT63) and 800°C (PCT89B), respectively (Figure 32). The two tests generally have good repeatability. In both tests, the PICs have initial ASR of about 0.07-0.08 ohm-cm^2. During testing, PIC ASRs improves with time and reached 0.05-0.06 ohm-cm^2 after one year testing, then slightly increased to the original value and leveled off. Based on long term durability test results, the precious metal cermet vias (epsilon PIC) can meet minimum two-year service life for the fuel cell systems we are developing. Post-test analysis of similar vintage of cells relates the PIC degradation during the second year to materials migration across PIC layers caused by some misalignment issues or pinholes/microcracks formed during cell printing or operating. Processing optimization and further mitigation of materials diffusion will help to eliminate or reduce PIC degradation to achieve longer service life of the fuel cell system.

Another activity for precious metal cermet based primary interconnect development is to further lower its ASR contribution. There are two approaches to reduce PIC ASR: 1) using high conductive via materials and cathode current collecting material (CCC) since CCC extends into the PIC area to transport electrons, and 2) modify PIC design to reduce resistance in specific local area. Higher conductive via materials evaluation was initiated in SECA phase 1. The volume fraction of the metal phase was altered with due to consideration of the cost impact with the objective of exploring where overall cost benefits could be achieved by balancing raw material cost inputs with ASR gains.

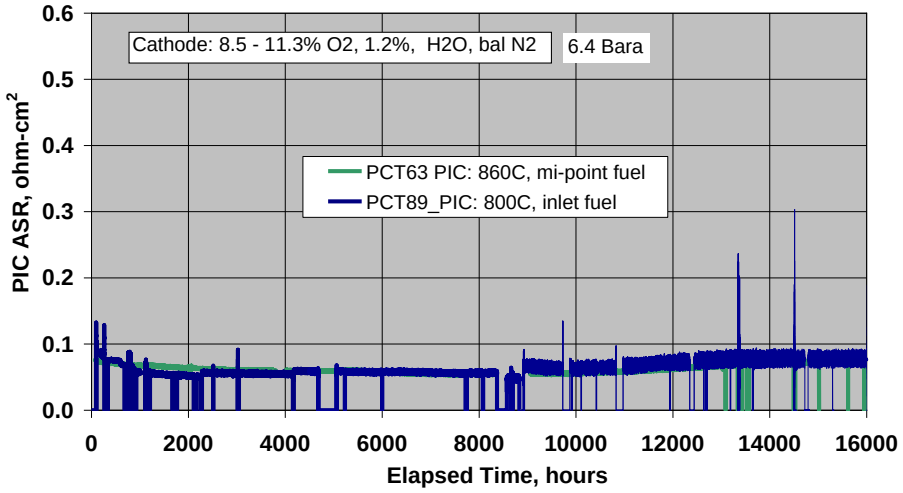

Figure 32. PIC ASR of 5-cell subscale long term durability (PCT63: 860°C, mid-bundle fuel, PCT89: 800°C, bundle inlet fuel)

Figure 33 is an example of ASR improvements demonstrated to date through use of the higher volume fraction of metal (~ 0.02 ohm-cm^2 benefit) and most favorably through combination with the higher conductance cathode current collecting (CCC) layers used in combination with the zeta nickelate cathodes. Additional durability data for the optimized cermet via plus advanced CCC layer shows PIC ASR levels falling below 0.03 ohm-cm^2 (Figure 34).

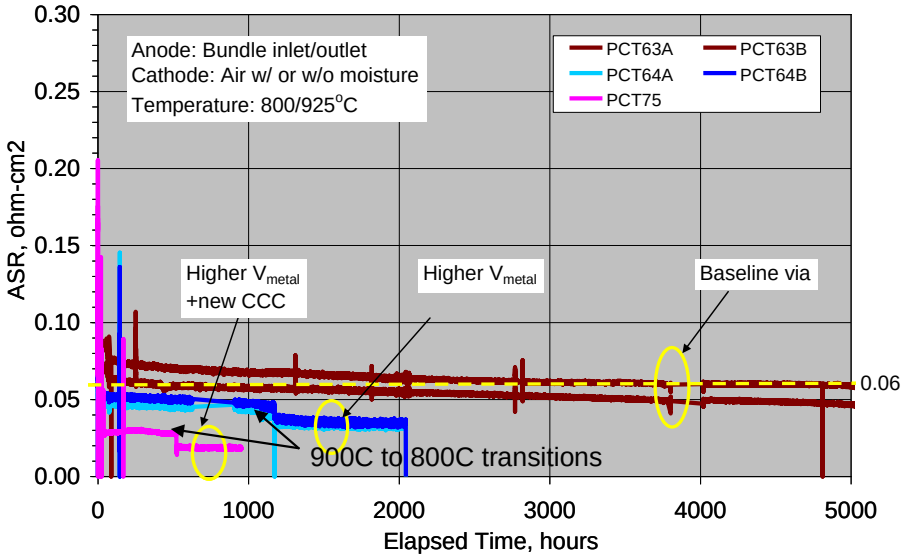

Figure 33. PIC ASR improvements with higher volume fractions metal phase

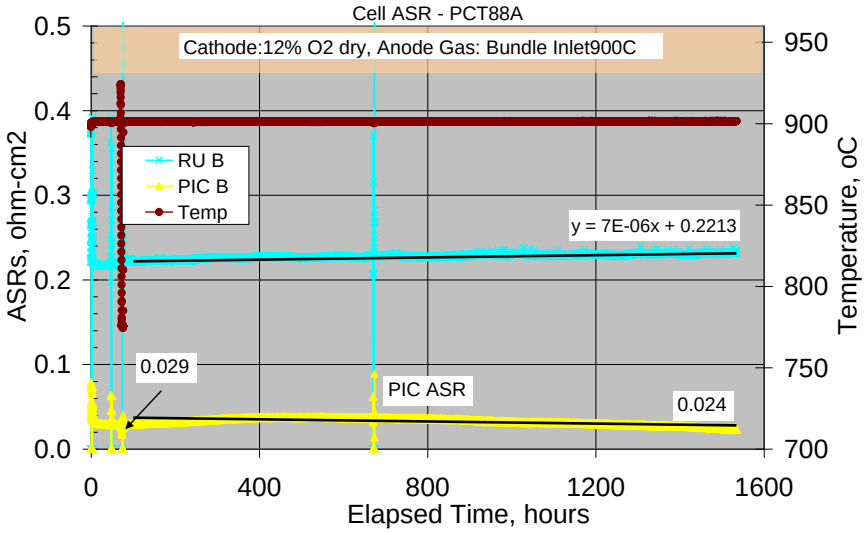

Figure 34. Additional long-term data for optimized precious metal + CCC interconnect ASR

A more substantial redesign of the primary interconnect was considered as a means to potentially reduce the PIC ASR for epsilon and zeta technology to <0.02 ohm-cm^2. The drive for this is to reduce overall cell ASR to allow a reduction in the peak operating temperature to improve long-term overall cell durability. The PIC redesign started at the modeling stage where PIC ASRs with different design were calculated and compared to that of the epsilon design. The principal of the redesign is to reduce PIC ASR while not significantly increasing printing area to keep materials consumption, thus cost low. Model calculations (Figure 35) indicates the epsilon PIC design has ASR of ~0.044 ohm-cm^2. For a non-via, full strip design, which has biggest printing area, a PIC ASR as low as 0.01 ohm-cm^2 is predicted. However, it will significantly increase materials cost. When PIC design of Case IVE is used, the PIC ASR can be reduced from 0.044 ohm-cm^2 to 0.022 ohm-cm^2 with the printing area is only increased slightly. The model calculated ASRs are lower than that actually measured. The reason is there is interface resistance effect in the real cells that the model did not take into account. By comparing the model calculation and the measured results, interface effect accounts for about 0.02 ohm-cm^2 contribution.

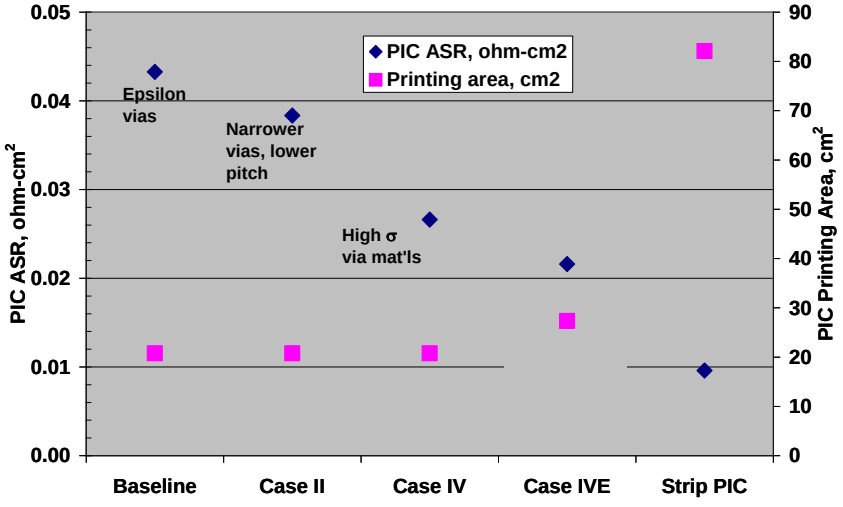

Figure 35. Calculated PIC ASR of different design based on the model

To understand the lowest PIC ASR achievable for this technology, 5-cell subscale test articles were prepared and tested. Figure 6 summarizes durability results of two subscale cells using the non-via, strip design with one cell using lower conductivity material and another using higher conductivity material. Up to 1800 hrs of testing under simulated system gas conditions, both cells have low and stable PIC ASR, 0.03 to 0.035 ohm-cm^2. PIC material conductivity did not have a significant impact with this design. The PIC ASR value is above the model predicted value of 0.02 ohm-cm^2, caused by the interface resistance between layers of the PIC; this is an area for further ASR reduction. More repeat tests of 5-cell subscale articles with long strip PIC design were performed, which showed even lower PIC ASR, 0.025 to 0.03 ohm-cm^2.

The PIC utilized in the Figure 36 test represents the most extreme shift in design from what has been our standard precious metal cermet via design. The modeling activity indicated other design options in between those cases that provide an optimum balance in ASR improvement and cost. One optimized design (Case IVE) was selected in Phase 2. Durability testing of 5-cell subscale test articles has been completed. Figure 37 compares the optimized PIC to the standard epsilon PIC demonstrating a ~0.03 ohm-cm^2 lower ASR and improved stability.

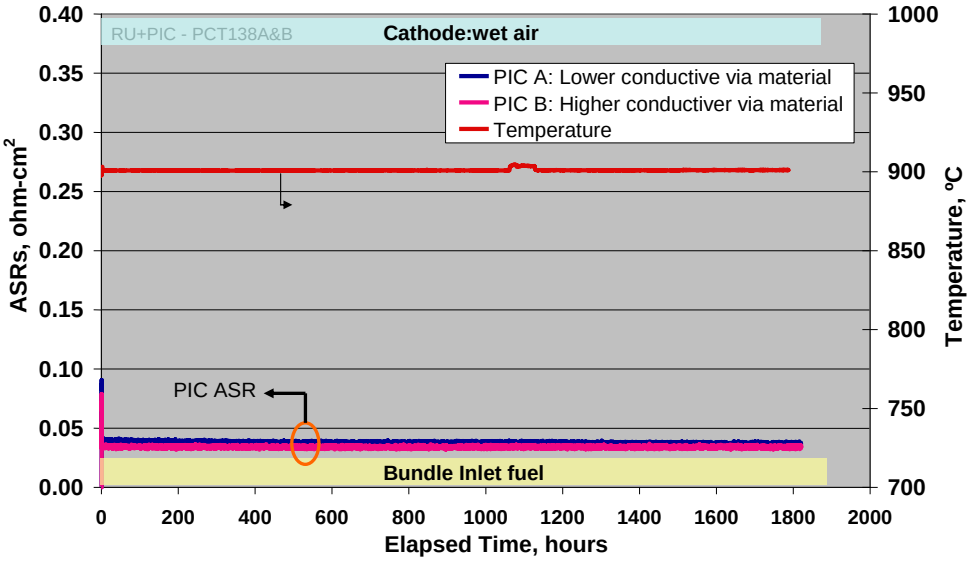

Figure 36. Lower primary interconnect ASR obtained with new interconnect design

In applying the epsilon PIC technology to zeta anodes, it has become apparent that the CTE of an important layer within the PIC region needs some adjustment downward to improve the yield/quality of the interconnect region and to provide a greater degree of freedom for combining this current interconnect technology with a range of anodes that are being explored for improved long-term durability. In addition, we've observed materials interactions between the zeta anode and the interconnect layers causing ASR issues. During Phase 2 alternate primary interconnect materials were screened first for compatibility with zeta anode. Screening tests include printed layer sintering and thermal ageing studies for compatibility studies and conductivity measurements.

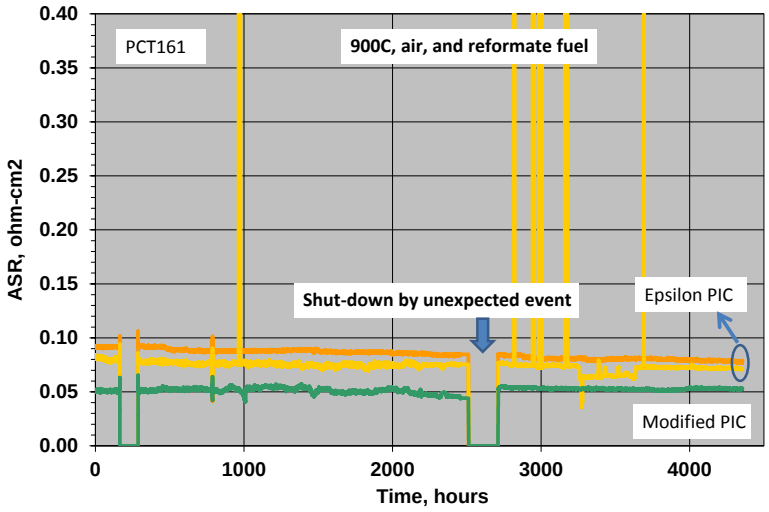

Figure 37. ASR benefits of modified PIC design Case IVE versus the epsilon PIC

Solutions to minimize the interactions between the zeta anode and the interconnect layers were identified. Alternate primary interconnect materials for pairing with zeta anodes were tested at the 5-cell scale, screened for compatibility with zeta anode. As shown in Figure 38, the two primary interconnect candidates show improving ASR, although still higher than the target. The rapid initial improvement for PIC B is related to its chemistry and reduction kinetics. Additional modifications are being considered to lower the ASR level.

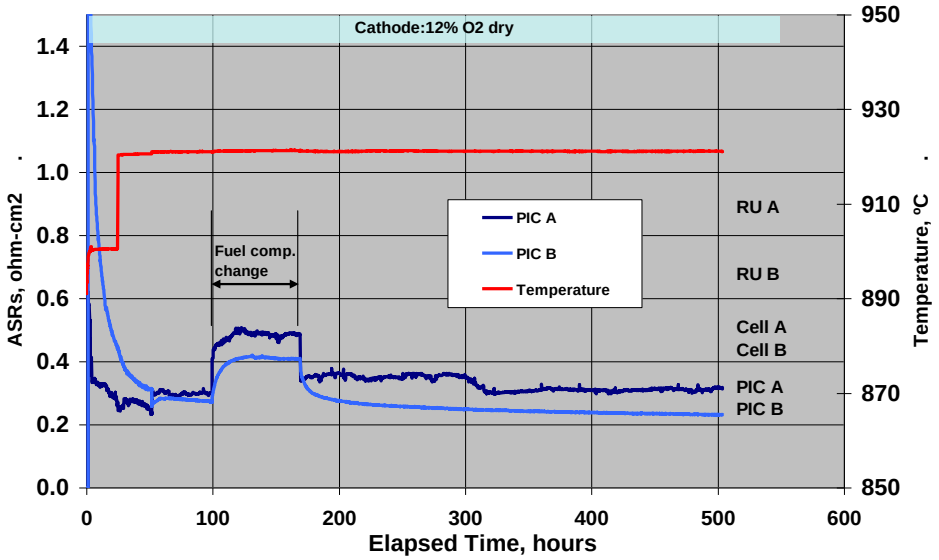

Figure 38. Initial ASR results for modified primary interconnect combined with zeta anode

Further testing of solutions to minimize the interactions between the single layer anode and the primary interconnect layers was then performed. Two modifications to the primary interconnect, design and materials, were evaluated and applied to cells also having an optimized single layer anode that has shown improved microstructure stability compared to the current baseline epsilon bi-layer anode technology (active anode plus anode current collector layers). Figure 39 shows that PIC ASR levels as low as 0.06 ohm-cm^2 have been obtained now when paired with a single layer anode technology. 5-cell subscale test articles, showing no degradation trend after 3500 hrs of testing (modified PIC 2) under simulated system

fuel composition, was shut down for post-test analysis to investigate whether any materials interactions exist, but that have just not shown up yet as an increase in ASR. Note that these test are with the original via baseline PIC design, hence ASR levels still in the 0.07 ohm-cm^2 range.

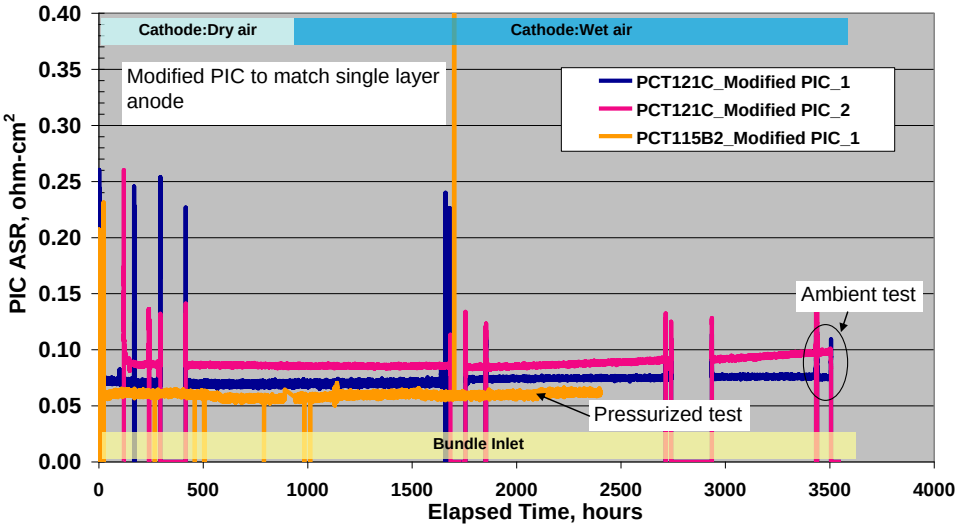

Figure 39. PIC ASR results (900C) for modified PIC combined with a single layer anode

LGFCS has been looking at further changes to the alloy composition of the PIC cermet via to seek even further cost reduction. Figure 40 summarizes a pentacell subscale test including results for what we consider our Gen2 alloy compositions (being used in the Block 2B test) versus 2 candidates, in which the concentration of lower cost conductive metal is increased. Candidate alloy A shows substantial ASR increases during testing at 800C whereas Candidate B maintains performance. Repeat testing is required for statistical comparison of ASR levels for the Gen2 and Candidate B alloy. This test is for the baseline PIC design, and future testing will include comparisons based on the lower ASR design Case IVE.

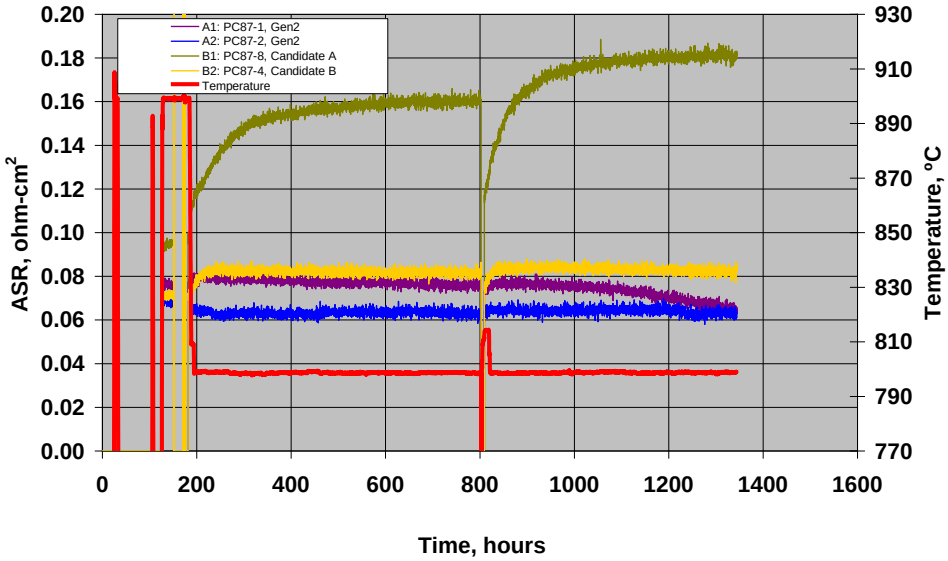

Figure 40. ASR trends for vias with alternate alloy compositions for the cermet seeking lower cost

Ceramic Interconnect: LGFCS has maintained an effort on ceramic interconnect development. A ceramic-based primary interconnect is not necessary for meeting SECA nor internal business cost targets, rather the interest is the availability of an alternate approach to evaluate for the ultimate 5 year service life desired at full commercialization. Three approaches to a ceramic interconnect are being pursued (1) traditional chromites, (2) n- plus p-type bilayered designs and (3) single layered non-chromites.

Several candidates resulted from this screening and 5-cell subscale articles have been processed. These solutions are being applied to primary interconnects based on the precious metal cermet vias. Screening of ceramic interconnect materials has continued with the identification of several compositions having suitable electronic conductivity over the range of pO_2 experienced during fuel cell operation. Constrained sintering experiments are still required.

To assess the PIC performance of a ceramic interconnect, a two dimensional model of the interconnect region was established (Figure 41). The ceramic interconnect is a strip across the substrate width direction, to maximize cross-sectional area for the lower conductive material, in contrast to the series of isolated precious metal vias that minimized materials and cost. The top layer is the extended CCC from the left cell and the bottom layer is the extended ACC from right cell. The model includes three ASR portions: 1) CCC layer in which current flows in-plane, 2) ceramic interconnect in which current flows through the thin layer, and 3) ACC layer in which current flows in-plane again. From the design where current flows through only thin ceramic interconnect layer, the ASR contribution is minimized. Fig.41b lists estimated PIC ASR levels for a ceramic interconnect conductivity ranging from 0.1 to 10 S/cm. The PIC ASR is acceptable if the ceramic interconnect material has a conductivity in the use environment of ≥ 1 S/cm, and therefore most chromites are potential candidates for LGFCS' segmented-in-series fuel cell.

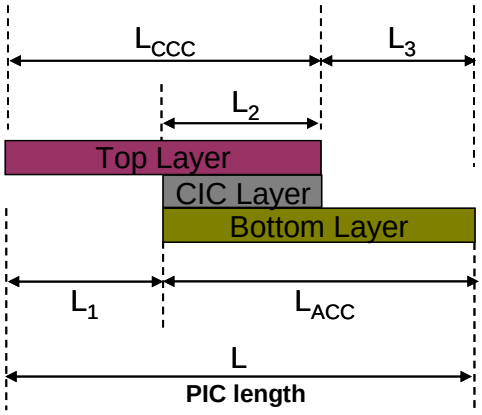

(a) PIC design with CIC (top layer: CCC, bottom layer ACC)

PIC ASR

CIC conductivity, S/cm	10	1	0.1
PIC ASR, ohm-cm^2	0.028	0.036	0.11

(b) Calculated PIC ASR

Figure 41. CIC design model for ASR contribution

LGFCS initiated preliminary evaluation of doped lanthanum chromites because of its high conductivity and stability under a wide range of pO_2 conditions. With proper doping on both the A- and B-site, the chromite pellets were fired to near 100% of theoretical density for several compositions using standard sintering temperatures for the LGFCS cells. However, when chromite inks prepared from these compositions were printed on the porous ceramic substrate and fired under constrained conditions, adequate densification of the film has proven difficult. Processing techniques such as low pO_2 firing to reduce Cr-species volatility and overprinting/sealing for improved densification have been tried with no success.

The alternative approach for ceramic interconnect development is to have a PIC design with a bi-layer structure (Figure 42), which consists of a n-type layer exposed to anodic gas (fuel), such as doped

strontium titanate, and a p-type layer exposed to cathodic gas (air), such as LSM. The advantage of a bilayer structure is less stringent requirements for the materials selection, either stable in lower pO_2 for layer 1 or stable in higher pO_2 for layer 2, and therefore more materials options that could also exhibit improved constrained sintering characteristics compared to the chromites.

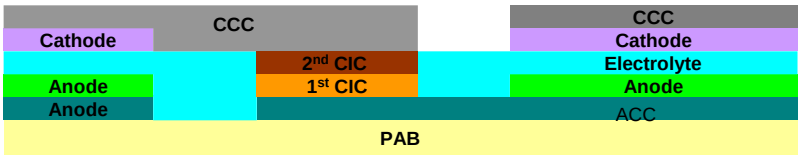

Figure 42. PIC design with bilayer ceramic interconnect

In this approach, the key task is to control the pO_2 at 1st layer and 2nd layer interface to make sure both n-type and p-type conductor are stable, which is feasible by controlling the layer thickness of the layers, and through selection of materials with good stability over wider pO_2 ranges.

This bi-layer concept was demonstrated in SECA Phase 1 using selected materials combination resulting in a PIC ASR of 0.12 ohm-cm^2 demonstrated at 900^{o}C, but with the ASR considerably higher at the low-end stack temperature of 800^{o}C.

Development work over the SECA Phase 2 related to ceramic interconnects investigated fuel-side material set for bi-layered interconnects. The technical challenge has been achieving a material that meets the conductivity requirements and that can be adequately densified in a constrained sintering condition (as printed layer on the LGFCS substrate). Figure 43 shows the conductivity trends for a favored composition. Key is reaching conductivities of >2 S/cm within a short time period at 900C. This composition shows excellent sinterability in pellet/bar form, benefiting from sintering aids.

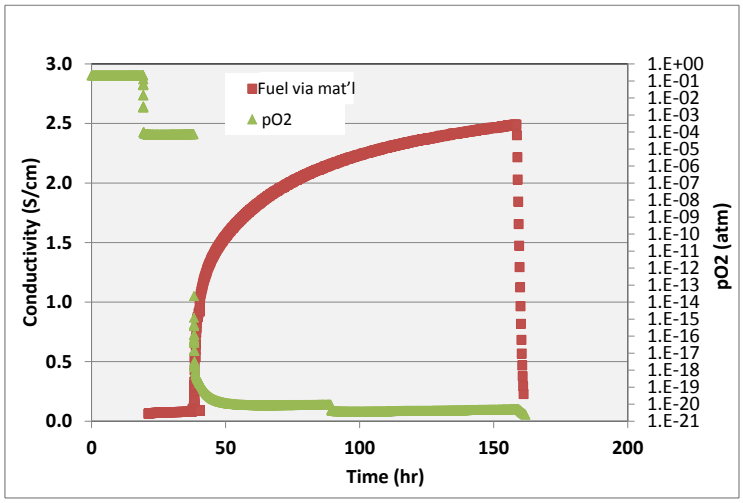

Figure 43. Conductivity of a fuel-side material for bi-layer ceramic interconnects

Constrained sintering experiments followed. Candidate bi-layer materials were selected for film sintering study under constraint conditions. This activity extended into a subsequent DOE-funded program where constrained sintering has now been achieved for both the anode-side and cathode-side layers and this latest bi-layer ceramic interconnect technology is now going into cell testing.

Conclusion – The cermet primary interconnect of the epsilon technology has been demonstrated at two year service life (~16,000 hours) under representative system conditions using the 5-cell platform with low degradation rate; this was the PIC technology used within the SECA Phase 1 and Phase 2 metric testing. Post-test analysis reveals some continued degradation mechanisms at play but technical solutions being pursued is expected to allow the cermet via interconnects to reliability meet service life's of greater than 3 years. Design changes to the cermet via design are being tested to lower the ASR associated with the primary interconnect but maintaining material combinations identified for achieving the targeted service lifetimes. The optimization of the PIC layers appear compatible with the next generation single-layer anodes (zeta) in testing up to 3500 hours under this program. Ceramic interconnects remain an option for long-term PIC stability, but is a longer development path. The bi-layer approach is showing the most promise with the ability to densify the candidate materials for those layers versus the challenges experienced for chromite-based ceramic interconnects.

Task 4.2 - Anode Development

Approach - Anode development efforts are focused on the CTE control, cost reduction, performance, and microstructure stability for durability. Primarily two anode designs have been developed during the SECA program. First, CTE matched, high in-plane conductance and cost reduction were the focus of development for the standard anode-ACC epsilon design (primarily Phase I activity). The second design has been the focus of the Phase II effort and is guided by further cost reduction and improvement in anode microstructure stability for long term durability. Development activities utilize subscale single and penta-cell with detailed instrumentation to separate ASR contributions by AC impedance and post-test analysis us performed to guide further developments.

Results and Discussion

Epsilon anode development: At the start of the SECA program, a revised anode current collecting (ACC) layer had been selected that represented a significant cost improvement over the original (alpha) anode technology. Final adjustment of the thermal expansion of this epsilon ACC was made by replacing part of metal phase with ceramic resulting in a decrease in thermal expansion from 11.7 to 11.2 ppm/K and matching better with the substrate while retaining sufficient in-plane conductance. Following initial screening tests of this modified ACC, it was ultimately selected for the cell technology to carry forward into the more extensive durability testing conducted prior to the Phase 1 metric test to give confidence in the ability of meeting the 2%/1000 hour degradation target. This epsilon cell technology has demonstrated degradation rates well below the 2%/1000 hour target of Phase 1 period and further testing was demonstrated to achieve the Phase 2 target (<1.5%/1000 hrs).

The epsilon anode development extended to Phase 2 mainly focusing on long term durability performance testing with subscale and bundle scale architecture. The standard epsilon anode completed 16,000 hour durability testing using a 5-cell article at mid-bundle fuel conditions and mid-block temperature (860^{o}C) with good durability trends (<1% power degradation per 1000 hours). A pressurized bundle test with epsilon anode shows very similar durability performance for 4,000 hours with less than 1% power degradation/1000 hour. Post-test SEM analysis of the anode+ACC layers following testing at the full system pressure condition (6.4 bar) and representative mid-range and peak operating conditions of temperature and fuel utilization is shown in Figure 44. The finer active anode microstructure is desirable for electrochemical activity. During operation some degree of microstructure coarsening is observed within the anode and ACC layers and there is materials migration affecting the nature of the anode-to-ACC interface. These are rather qualitative assessments, and quantification of the compositional changes across the anode+ACC was performed under a separate program. Initial results support the hypotheses

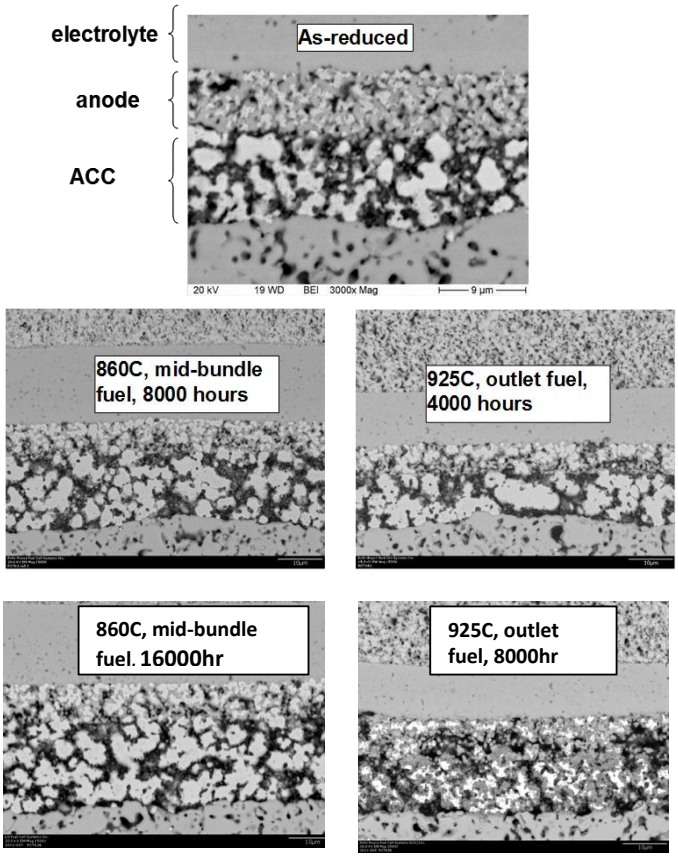

Figure 44. Evolution of anode-side microstructure under system mid-point and most aggressive block operating conditions

of metals volatility, $Ni(OH)_2$, at higher temperatures and fuel utilization. High permeability tubes help to mitigate such losses by minimizing the local p^2_{H2O}/p_{H2} ratio within the anode. Although the standard epsilon anode achieved adequate microstructure stability to meet the overall durability targets of the program, microstructure stability at high end system temperature (~900^{o}C) where steam partial pressure is also high and metal depletion between anode and ACC was deemed a risk for the targeted service lifetimes.

The SECA long-term objective is demonstration of cell technology capable of providing a 40,000 hours of operation, and this is consistent with LGFCS' eventual target for a commercial fuel cell system offering to the distributed power generation market. Further optimization of the anode layers, combined with lower system operating temperatures and higher permeability tubes, are driven by meeting the 40,000 hour of service life. LGFCS has pursued two approaches to improve anode durability, which are considered candidate zeta-technologies. The first approach is a bi-layer design continuing with separate anode and ACC layers to provide some degrees of freedom for engineering in both the activation and ohmic resistance requirements of the anode side. The second approach is a single layer anode which is functioned as both anode and anode conductive layer. The advantage of this approach is elimination of anode/ACC interface which is prone to degradation over time due to increased ohmic resistance resulted from materials migration away from interface. The weak interface also increases a mechanical reliability risk.

First bi-layer approach was selected to improve poor interface issue for epsilon anode. With the bilayer structure, one can print a thinner functional layer for catalytic function, which shows good microstructure

stability, and a separate thicker layer as ACC for in-plane conduction. A single cell had been tested at 900°C/950°C in ambient test rig for ~2150 hrs, showing stable performance (Figure 45). The cell was then transferred to a pressurized test rig for another ~1300 hrs of testing at 6 bara and 900C showing no sign of degradation. This test was under bundle inlet conditions but using a low permeability tubes. Initially during the phase 1 period, both single-layer and bi-layer approaches have experienced challenges when scaling up to 5-cell and full test articles as the interaction of these layers with the standard epsilon primary interconnect design has resulted in higher ASR for primary interconnect (PIC) region. Metal depletion at anode/ACC interface was also identified in this bi-layer design, similar to what has been observed in the epsilon anode cases. This observation influenced a focus on single anode development during the Phase 2 period.

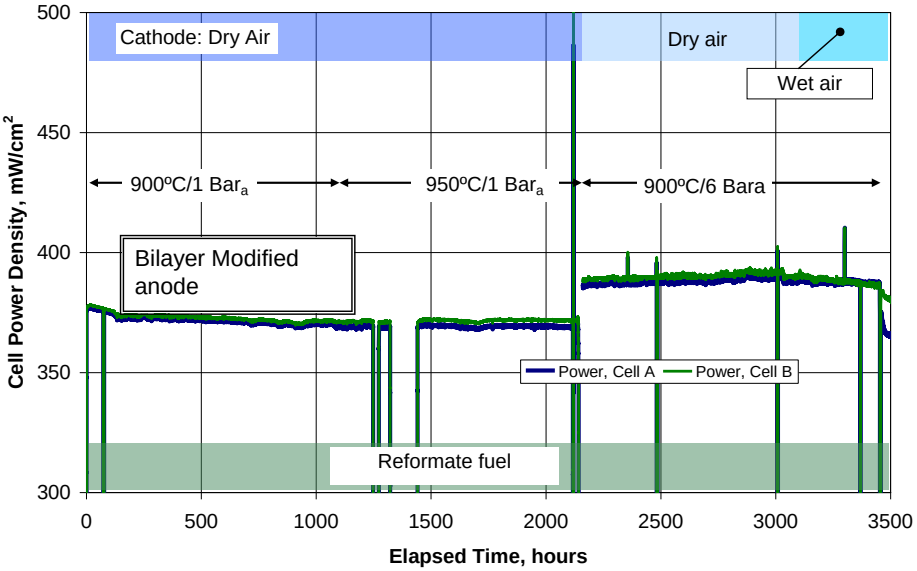

Figure 45. Durability trend for a bi-layer anode design.

Single layer (zeta) anode: To eliminate the poor interface due to metal migration at anode and ACC interface, a single layer (zeta) anode development was pursued. The preliminary test of zeta single layer anode during the SECA Phase 1 period showed similar performance levels as the epsilon anode materials sets. Initial degradation testing of the single layer anodes was under 0.5%/1000 hours for ~2300 hours under aggressive testing conditions of 925°C and bundle outlet fuel (80% system fuel utilization). The EIS analysis before and after durability confirmed minor change in total cell ASR and Rp.

Post-test analysis of the zeta single layer anode after ~2500 hrs of testing at 925°C and 20% flammable bundle outlet condition is shown in Figure 46. More uniform microstructure was maintained after long term operation. However, the single layer anode does show greater risk in terms of CTE and modulus match with the substrate. Since single layer functions as both active anode and conductive layer, the composition has to be balanced to meet multiple requirements: 1) good electrochemical performance for lower ASR; 2) enough conductance for in-plane conduction; 3) microstructural stability; and 4) matched CTE with the substrate and electrolyte. Optimization of the layer composition is being explored to avoid too high thermal stress between anode and electrolyte/substrate. Third phase, inactive fillers, has been added to reduce the CTE with no adverse effect on performance. Thermal expansion match to the substrate to avoid mechanical failure was a critical area for the optimization for successful transition of the zeta single layer anode from small subscale cell to a full tube mass production with high yield. Conductance measurement was conducted using different screen mesh for a selected single layer anode

composition. A mesh size of 230 or 200 is desired to achieve target anode side conductance, 1 S, as shown in Figure 47.

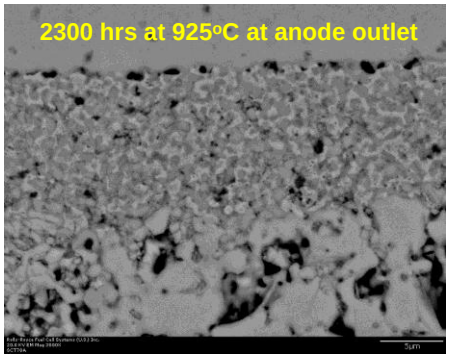

Figure 46. SEM of single-layer anode tested for 2300hr at 20% flammable bundle outlet and 925C

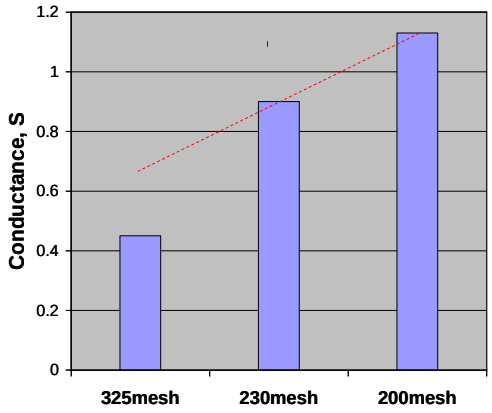

Figure 47. Conductance trends for single layer anode with screen mesh

LGFCS established a database correlating thickness of selected single layer composition and conductance. However, at such a thickness, or 200 mesh, we periodically observed issues due to CTE mismatch. To optimize the CTE relationship between single layer anodes and the substrates, LGFCS is investigating modification of single layer anode compositions and also adjusting the CTE of substrate. The higher CTE substrate can allow application of higher conductance anode layers to provide some reduction in ASR. The further reduction of cell ASR is important to improve system long term durability by lowering average operating temperature.

LGFCS reported in Phase I some difficulty in matching epsilon PIC technology to both zeta bi-layer and single layer anodes to achieve low and stable PIC ASR values. During Phase II, more effort was performed to modify epsilon PIC for compatibility with zeta anode technology. Significant progress has been achieved allow the durability testing of the single layer to be extended to 5-cell subscale test articles. Figure 48 shows side-by-side durability test of epsilon bilayer anode and a single layer anode under simulated aggressive system conditions, bundle outlet fuel, 925C, and 4 bars. Within ~3000 hrs of net testing time, modified epsilon anode and single layer anode showed similar repeat unit power density and degradation rates confirming the functionality of the PIC with the single layer anode.

During the Phase II period, the key objective was further validation of the single-layer technology. Based on limited statistical data (Figure 49), the three different anode technologies (epsilon, modified-

epsilon and single layer) may have similar initial cell ASR and degradation rate over the time periods thus far tested. Although the standard epsilon anode has shown reasonable durability results based on subscale cell (5-cell) tests, the post-test examination revealed significant microstructure change that raised concern if the bi-layer anode plus ACC epsilon anode technology can achieve five year life required by commercial product.

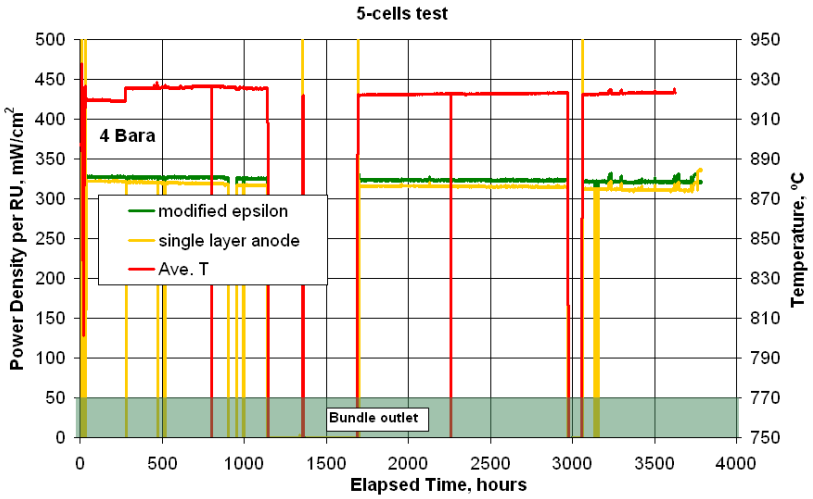

Figure 48. Durability comparison for 5 cell tests: modified epsilon and single layer anode for bundle outlet fuel at 925°C and 4 bar.

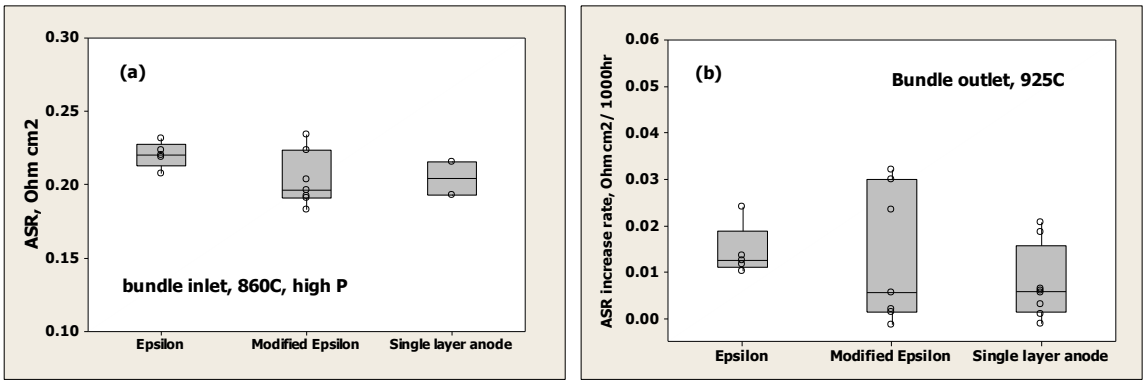

Figure 49. (a) Initial cell ASR at 860°C/high pressure and (b) Cell ASR increase rate for durability for different anode technology.

Promising cell ASR and durability results have been achieved for single layer anode through multiple subscale cell testing under aggressive system conditions (high temperature and high steam). Two longer term durability tests have been completed for single layer anode. Figure 50 is a single cell test with selected single layer anode composition tested for 3000hrs at 4 bar, 925°C (slightly outside of planned system block operation for accelerated testing) and bundle outlet fuel condition. The test experienced a problem related to the test rig that caused ASR increase (cathodic side due to moisture) for about 1000 hrs of testing. But, upon repair, cell ASR is recovered. Figure 51 is a pentacell (5-cell in series) test combined with PIC developed to match zeta anode, which accumulated total 7300 hours under aggressive conditions of 925°C and bundle outlet fuel composition. Compared to the previous epsilon bi-layer anode with ACC showing an ~0.01 ohm cm^2/1000hr degradation rate at same test condition for 8000hrs, the

single layer anode shows ~50% improvement in degradation rate during a similar test period. A key benefit of the single layer design is elimination of an ohmic degradation mechanism associated with the formation of a poor interface between the active anode and the ACC.

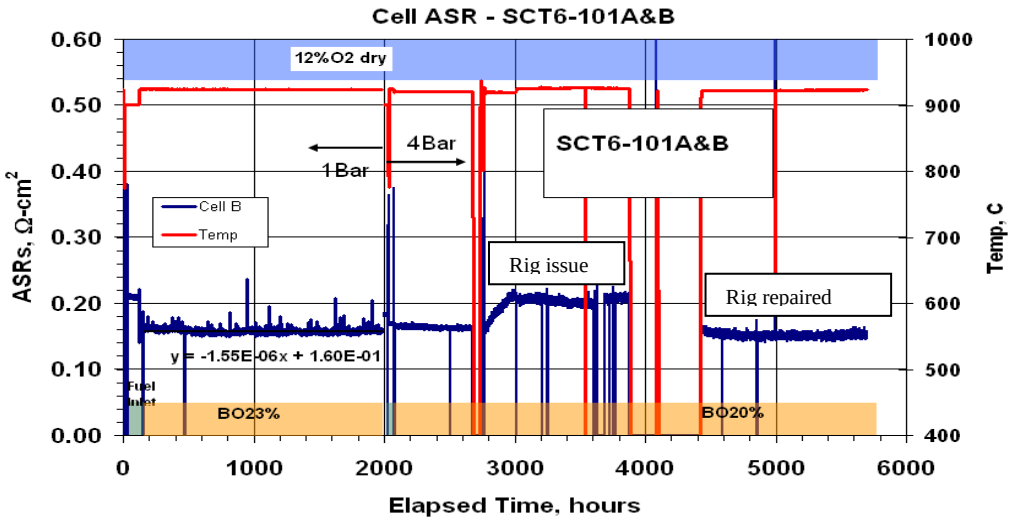

Figure 50. Durability result of single layer anode for 5000hrs (2000hrs at 925°C/1bar and 3000hrs at 925°C/4bar) at aggressive bundle outlet fuel condition.

After these longer term durability tests, post-test analysis revealed that the single layer anodes has a more uniform microstructure compared to epsilon bilayer anode. In addition, the single layer anode shows good adhesion with both electrolyte and porous anode barrier layer (PAB). Post-test SEM images for both cells are shown in Figure 52. It can be seen that both cells, 5000 hrs for single cell and 7000 hrs for pentacells, show similar microstructures. As observed in the images, the anode layer is fairly thin in this test article, which was made on purpose to avoid thermal stress issue resulting from thermal expansion mismatch between the substrate/electrolyte and anode. We have investigated the thickness effect of single layer anode on the performance. A pentacell (5-cell article) with a thicker single layer anode (higher conductance, lower ohmic resistance) has lower ASR which was achieved by employing a substrate with higher thermal expansion coefficient. In addition to using higher CTE substrates to lower the anode side ASR contribution (thicker anode provides higher conductance, or lower resistance), LGFCS has also explored the use of substrates with thinner walls. AC impedance analysis has shown the potential of up to 0.02 ohm-cm^2 ASR reduction resulted from lower fuel diffusional resistance.

Although similar degradation trends have been observed for both anode compositions up to ~8000hrs of testing time, it is expected that single layer anode will have lower degradation rate beyond 8000 hours because of the favorable microstructure stability observed in testing thus far to 7000 hours. Given the success of the single layer tests at single and 5-cell scale, the technology was scaled to bundle testing. Figure 53 shows 600 hours of short term testing, with the power degradation rate of the bundle at 0.5%/1000 hrs. During development of lower-cost single layer anode, CTE mismatch was well addressed and thermal stress was resolved for the full-scale printing.

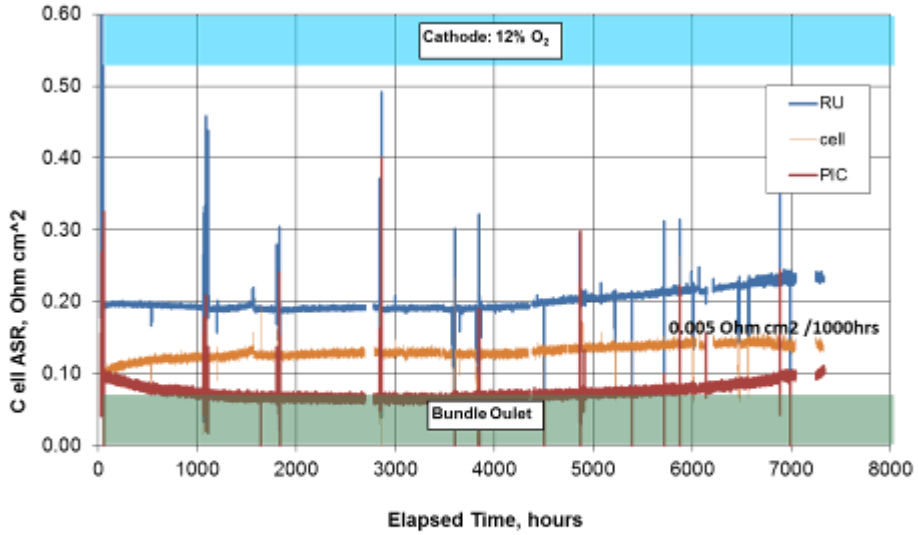

Figure 51. Promising durability result for single layer anode under aggressive testing condition

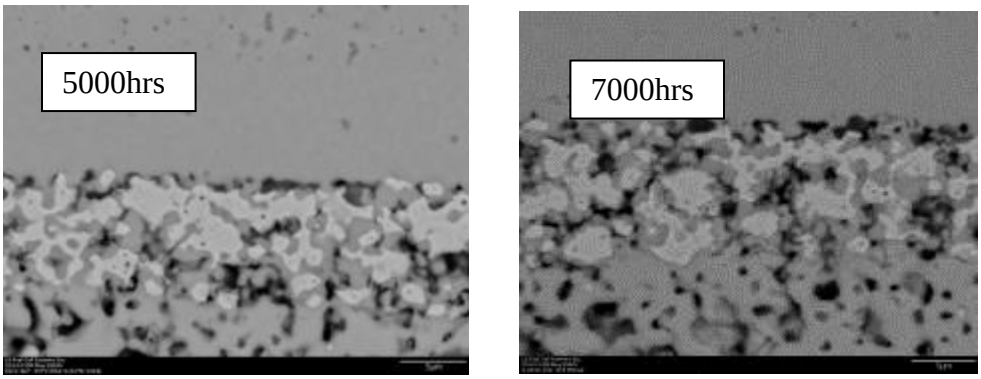

Figure 52. Post-test analysis of single layer anode (2000 hours at 925°C/1 bar and 3000 hours at 925°C/4 bar) all at bundle outlet conditions for aggressive testing

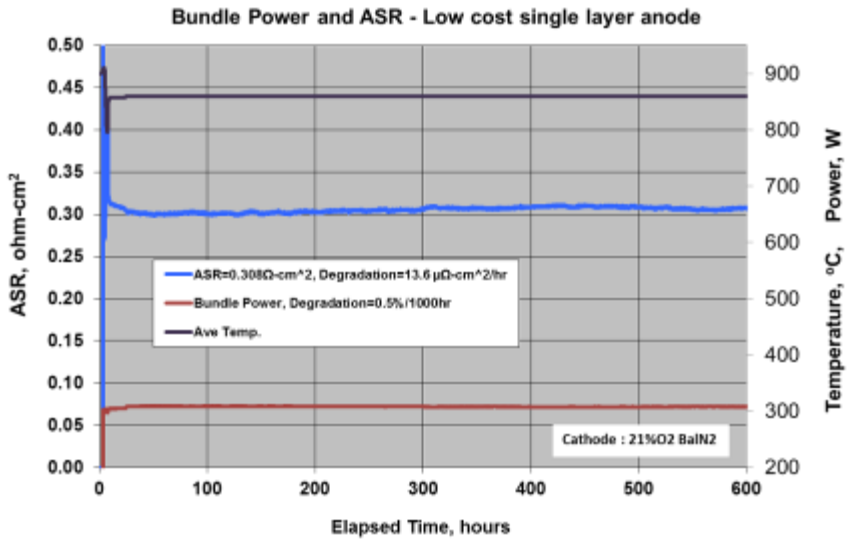

Figure 53. Power and ASR in bundle test for low cost single layer anode

Anode redox testing and development: During fuel cell system operation, emergency events may happen, which may shut off fuel flow and cause oxidation of anode side materials. When fuel cell system is re-started, anode needs to be reduced again. LGFCS employs an anode protection system for such events but a better understanding of the redox behavior of the current epsilon and next generation single layer anodes may provide more favorable, lower cost scenarios for normal system start-up/shutdown and emergency shutdowns. Figure 54 shows cell ASR and anode/ACC conductance change as a result of aggressive redox cycling by turning off fuel flow and switching to an oxidizing gas while holding the cell at 900°C. Cell ASR shows slight improvement after first redox cycle whereas small step change (increase) after 2nd and 3rd redox cycle, and then larger step change (increase) after 4th and 5th redox cycle AC impedance analysis confirmed DC data, as shown in Figure 55. There is significant ohmic ASR reduction after 1st redox cycle. Anode activation (3000~6000 Hz) increase attribute to cell ASR change starting from 3rd redox cycle. Microstructure analysis was performed after test and significant changes are observed. Future anode redox testing will be conducted under broader system operating conditions, and meanwhile anode compositions with better redox tolerant property is being developed.

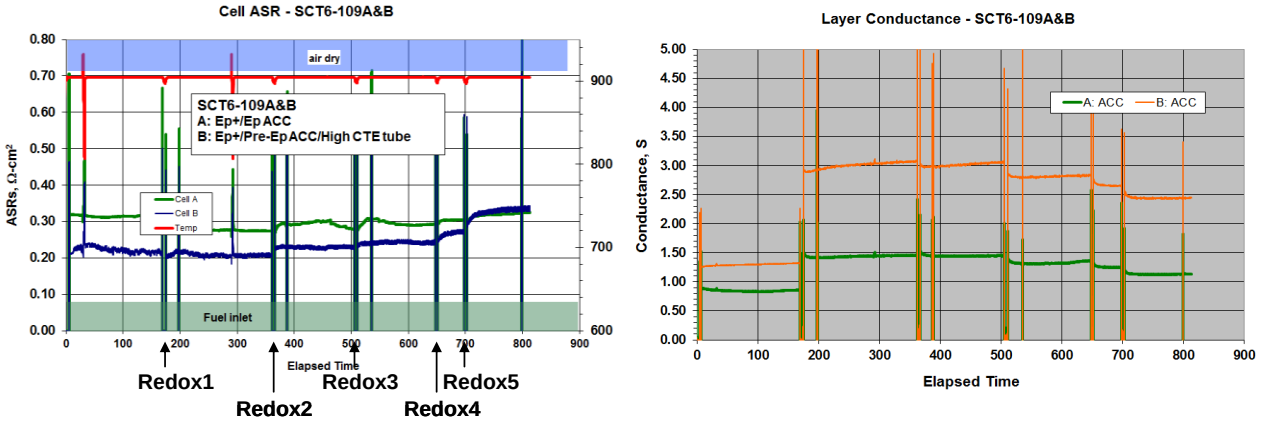

Figure 54. Redox behavior of epsilon anode: cell ASR (left), anode layer conductance (right)

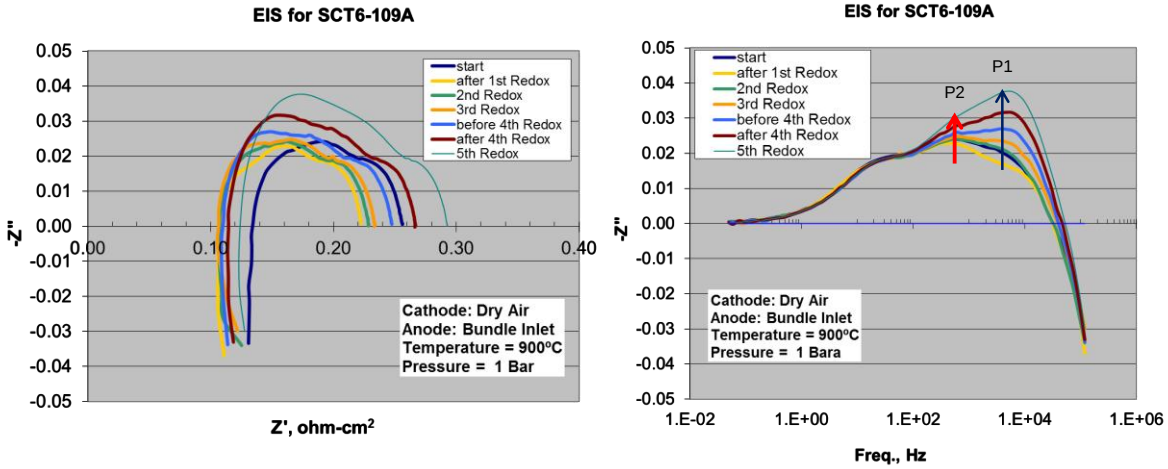

Figure 55. AC impedance after each redox cycle: Nyquist plot (left)and Bold plot (right)

Conclusion - The current standard epsilon anode materials are adequate for 5000hr operation time required for the SECA metric tests. We have demonstrated the standard epsilon anode performance with different test articles such as subscale cell (16,000hrs), pressurized bundle test (4,000hrs), and metric test with 2 strips-Block (2,200hrs) and 5 strips-Block test (3,000hrs). However, post-test analysis of 5 cell test article following 8000hours of testing at the most aggressive system conditions of and bundle outlet fuel (higher steam partial pressure and pO_2) shows considerable microstructure deterioration and evidence of depletion and re-distribution of metal component. Even though the epsilon anode materials demonstrated acceptable durability for 16000hrs at middle and low temperature, microstructure stability of anode side materials are still concern for commercial product with 3-5 year service life. Several designs and material combinations are being evaluated. Among which single layer anode technology shows promising potential for improved microstructure stability and longer term durability based on side-by-side accelerated testing with epsilon anode. A selected single layer anode demonstrated stable durability performance for 7,000hrs at aggressive bundle fuel at 925C at 4 bar) and post-test analysis showed more uniform microstructure. One of challenge area for single layer anode is CTE mismatch between anode and the substrate/electrolyte layer. Solutions were identified and demonstrated. Full tubes were printed and bundle level scale was tested with stable performance in short term durability. Anode protection scheme is being considered and explored for commercial fuel cell systems. Redox tolerant anode is ultimate material solution. In the near term or entrance-into-service product, an anode composition with improved redox tolerance (without showing noticeable performance degradation after multiple redox cycles) is desired.

Task 4.3 - Cathode Development

Approach: Cathode development efforts have focused on establishing an understanding of a lower-temperature range (775C-825^{o}C) moisture effect that adversely affects the cell ASR, and that does not appear to be long-term degradation issue but rather a short-term ASR increase/materials equilibration phenomenon. Activities have also involved screening of alternate LSM-based cathodes tolerant to ambient levels of moisture with an overall goal of the reduction in cathode polarization resistance to allow lower temperature stack operation as an approach for extending stack life. Extended testing to >16,000 has been performed to identify longer-term degradation mechanisms and screen optimized cathodes. Development of an improved LSM-based cathode has been the main thrust but LGFCS has also continued its investigation of the newer class of nickelate MEIC cathodes. Electrochemical screening tests are first conducted using cathode symmetrical button cells and single-cell substrate test articles with AC impedance analysis.

Discussion of results -The primary focus of the cathode development activities during Phase 1 was to deepen our understanding of the ASR contributions from the LGFCS standard LSM+YSZ composite cathode, especially at the low temperature and steam conditions expected in the local area of a block, to insure that the epsilon material sets meet the average stack ASR target within the range of stack temperature differentials expected for the system. When an early (pre-SECA) LGFCS system cycle included off-gas combustion of the remaining fuel into the cathode loop for thermal balancing, performance of the fuel cell was found to be affected by the high moisture content (~10%) of the cathode air. LGFCS therefore modified its system cycle to be a nominally "dry" cycle, with moisture present only from the ambient air and any fuel leakage. This was assumed to alleviate any ASR loss caused by moisture. However, testing protocols that then began to include ambient moisture levels (Figure 56) revealed that upon insertion of 1% moisture, the cell began to degrade, and the degradation rate increased upon changing the moisture level to 2% and then 3%. When the temperature was then ramped up from 775^{o}C to 800^{o}C, the degradation subsided. The conclusion was that moisture effect is more significant and noticeable at lower operating temperatures. This phenomenon was also observed and reported by other researchers and had been duplicated multiple of times by LGFCS. LGFCS observed complete and rapid recovery of ASR upon increasing temperature to 900^{o}C and removal of the moisture content.

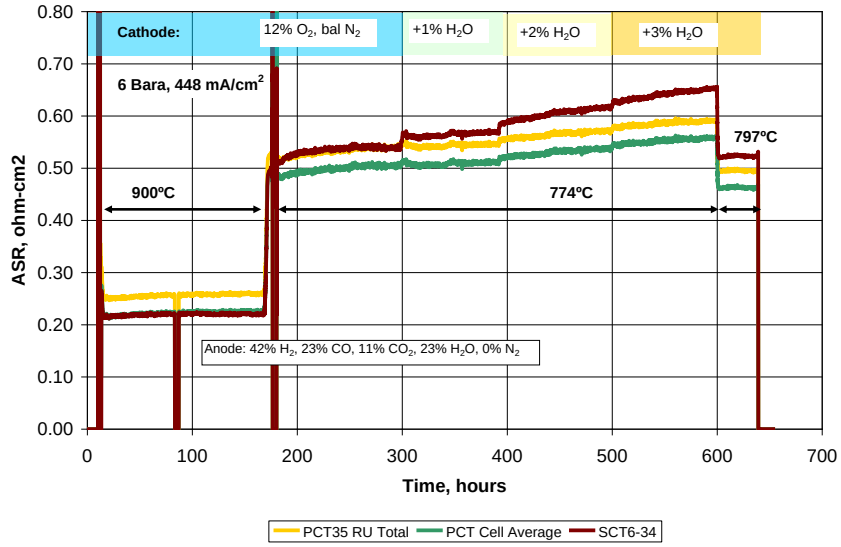

Figure 56. Moisture effect (1% to 3% moisture) on LSM-YSZ cathode at low temperatures

To seek an understanding of this cathode moisture issue, LGFCS has worked closely with Case Western Reserve University (CWRU) and performed detailed analysis by means of state of the art equipment. The Mn valence state was first determined using XPS and EELS/TEM for LSM powders aged at different conditions and for cells tested at low temperature with moisture. The overall finding was that the Mn valence state increased with decreasing temperatures, which may relate to an oxygen vacancy change, and a direct correlation between Mn valence state and moisture content was not observed. The extensive TEM examination of LSM+YSZ cathodes (as-fabricated, tested at low and high temperatures with moisture) revealed three significant findings. First, free MnO_x was identified in both as-fabricated and tested cathodes. However, the Mn valence state in MnO_x for cathodes tested at low temperatures and in moisture was higher than that observed for as-fabricated and high temperature-tested cells. Secondly, for cells tested at low temperatures and in moisture, the free MnO_x appears present in a greater amount at the cathode/electrolyte interface. Thirdly, silica contamination, 15-20 at%, was found in the MnO_x, but it is uncertain how much is from testing or inherent cathode/YSZ impurities (Figure 57). The influence of the

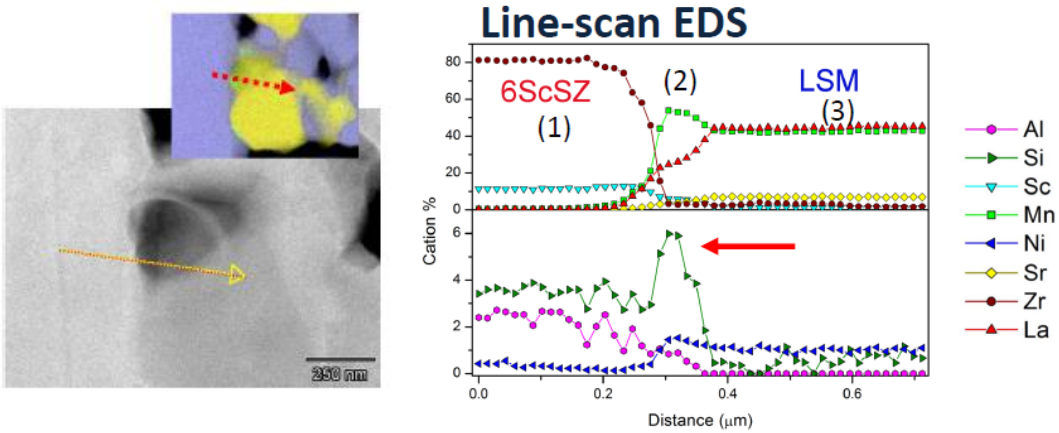

(a) Electrolyte/cathode interface **(b) EDS line scan: Si & Mn rich at interface**

Figure 57. TEM(a) and EDS(b) for LSM-YSZ cathode tested for 2000 hrs, 800°C with 1.2% steam

free, localized MnO_x and silica impurities on the moisture affect requires more study, as the rapid ASR changes on changing moisture and/or raising temperature need better understanding. The presence of free MnO_x is also a concern for Cr-related contamination as influencing $MnCr_2O_4$ formation and blocking active sites.

Thermodynamic calculations indicate Mn solubility is limited in LSM. During cathode processing at 1150°C in air, the maximum Mn solubility in LSM is ~50.4%. For the LGFCS A-site deficient cathode, the theoretical Mn content is higher than this solubility limit. During fuel cell operation, the Mn solubility is predicted to be even less given the local reduced oxygen partial pressure. The high A-site deficient LSM formulation was originally selected intending to avoid $La_2Zr_2O_7$ pyrochlore formation at the cathode/electrolyte interface. From TEM examination and thermodynamic calculation, high A-site deficient LSM formulation possibly introduces a degradation mechanism. While seeking an understanding of the moisture effect, LGFCS has also been screening alternate cathode compositions for moisture tolerance. Based on the literature, a change of ionic phase in LSM composite cathodes or optimization of cathode /electrolyte interface may improve its moisture tolerance. LGFCS first evaluated a LSM-ScSZ cathode and performed side-by-side test with the LGFCS standard cathode. As expected, the LSM-ScSZ cathode had a lower ASR due to the higher ionic conductivity of ScSZ (Figure 58). The cell having a LSM-ScSZ cathode had a lower degradation rate, 0.01 ohm-cm^2/1000 hours versus 0.03 ohm-cm^2/1000 hours for the standard LSM-YSZ cathode, at 775°C, 3% moisture, and 1 Bara. As previously observed, both cathodes were stable after ramping to 800°C. A hypothesis for the better moisture tolerance of the LSM-ScSZ cathode is a lower free MnOx content within the cathode as TEM analysis by CWRU has shown that Mn has much higher solubility limit in the specific ScSZ tested than the original YSZ ionic phase (4.2% versus 1.7%). Under the hypothesis that free MnOx is a factor in the cathode moisture effect at low temperature, LGFCS pursued LSM composite cathodes with reduced free MnOx content.

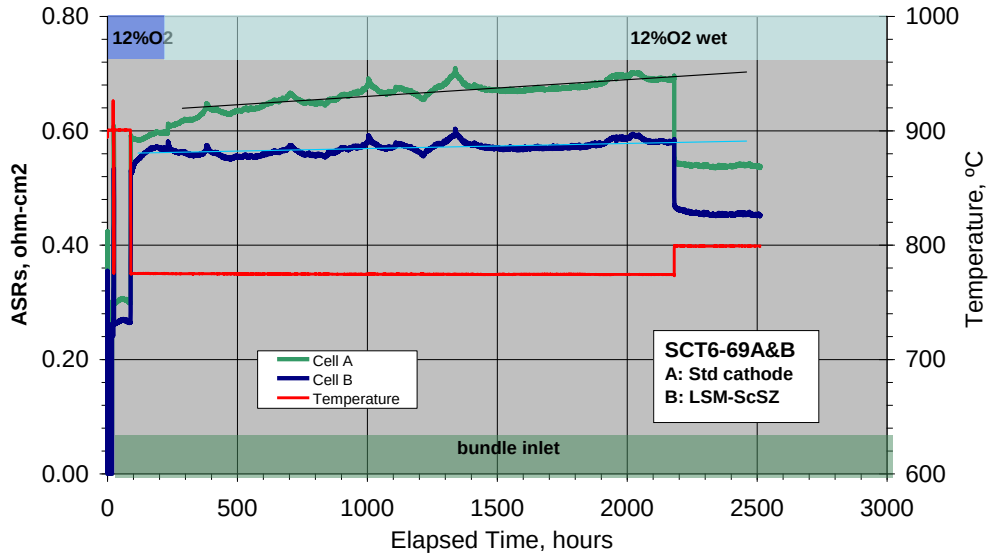

Figure 58. Durability of LSM cathode with 3% moisture

During Phase II, the impact of MnOx segregation was further investigated through long-term testing and mitigation approaches screened. Figure 59 showed the microstructure evolution of standard (epsilon) LSM+YSZ composite cathode at 800C with the testing up to 16,000 hours. In as-fabricated cells, free MnOx was generally uniformly distributed across the epsilon cathode. During testing, free MnOx started to migrate to the electrolyte interface and manifested in the image of 8000 hours. More MnOx accumulated to electrolyte interface when the testing had run to 16,000 hours.

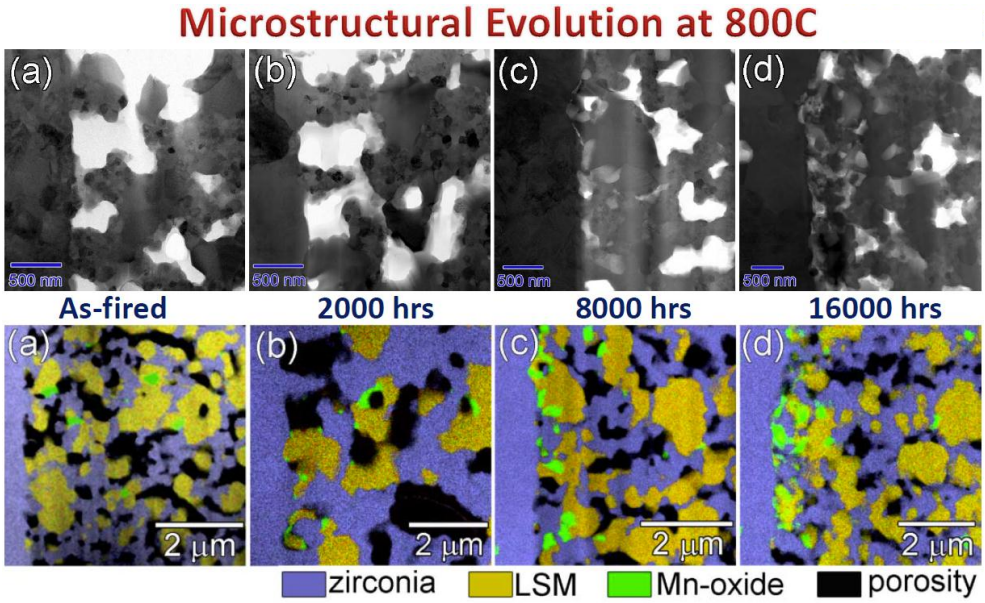

Figure 59. Subscale tube cell with epsilon cathode tested at 800C and various durations

Subsequent durability tests with a reference cell (held at OCV) printed nearby the active cell areas revealed free MnOx is distributed across the reference cell cathode after 5000 hours exposed to the testing air/fuel and temperature conditions whereas the active cell showed an accumulation on MnOx near the electrolyte (Figure 60). One hypothesis is that the electric field is a factor in the MnOx distribution. To mitigate free MnOx issue, cells and pellets prepared from different non-stoichiometric LSM and ionic phases were evaluated through aging and electrochemical testing, and post-TEM analysis. Longer-term tests with reference cells are required to expand the understanding and dependency of the MnOx degradation and transport mechanism.

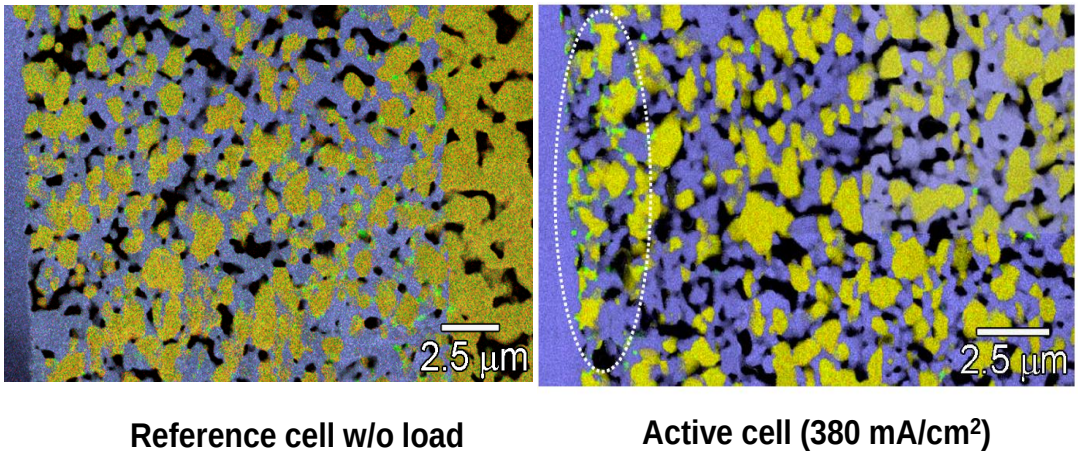

Figure 60. Subscale tube cell and reference cell TEM imagines after 5000 hours test at high temperature and pressure

Another degradation mechanism identified during Phase 2 program is the densification of LSM-based cathode (epsilon technology) after long term durability testing under simulated system conditions. Figure 61 show the post-test SEM and TEM images of PCT63B after being tested for 16,000 hours at 860°C, 6.4

bara, and diluted air with ~1% moisture. The densification and LSM grain coarsening only occurred near the electrolyte/cathode interface whereas the microstructure away from the interface did not show noticeable change compared to the as-fabricated cell. Cathode microstructural change or densification during operating may be one of the key degradation mechanism since the densified layer may reduce active triple phase boundaries (TPB) near the electrolyte interface (a critical region for catalytic reaction taking place) and also increase air diffusion resistance to the TPB.

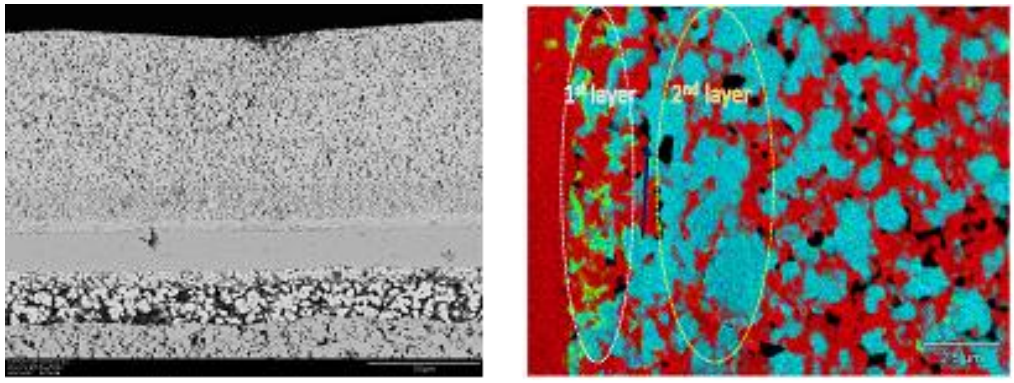

Figure 61. SEM and TEM images of subscale tube test at 860C under system simulated condition

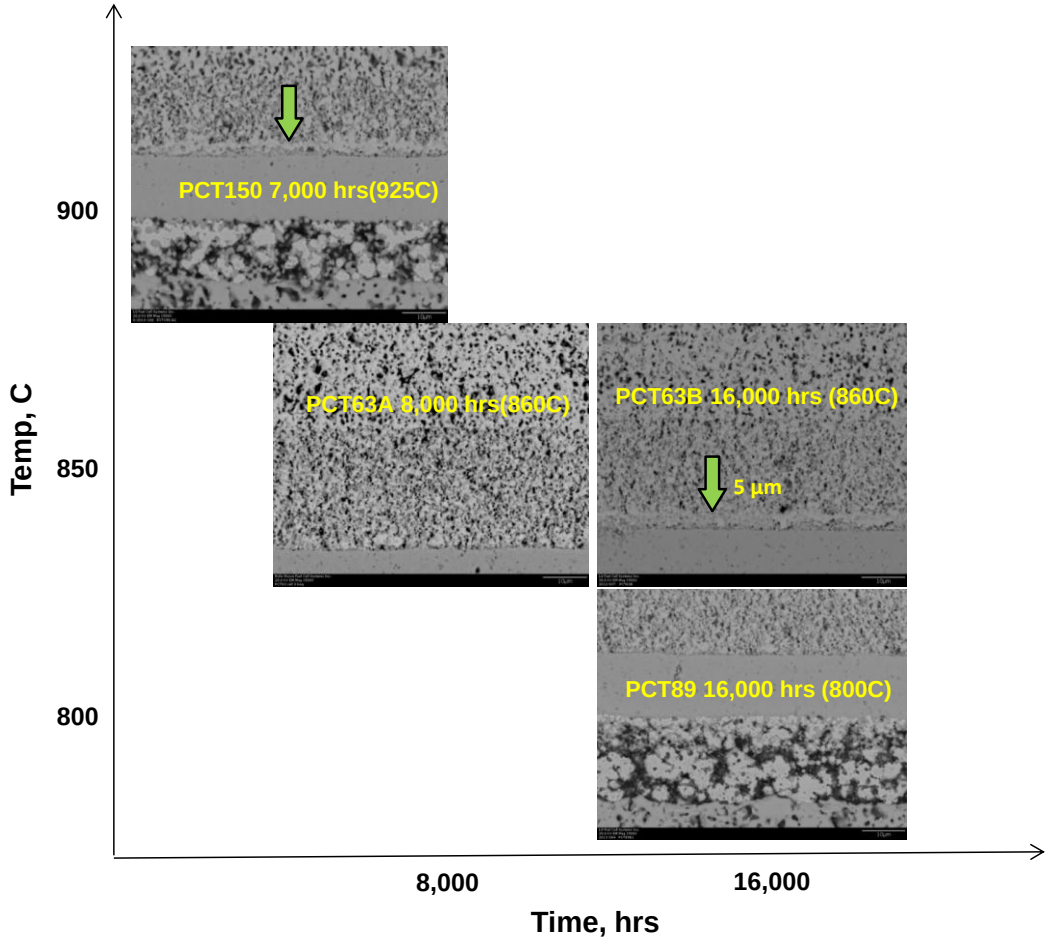

Figure 62. SEM images of subscale cells operated at different temperatures and durations under simulated system conditions

Further investigation found the formation of microstructure densification is closely related to testing temperature and time (Fig. 62). PCT63A, tested at 860°C and 4 bara for 8,000 hours, did not show cathode densification. No cathode densification was observed either for PCT89 which was tested at lower temperature of 800°C for 16,000 hours. However, such cathode densification was identified in PCT150 only after 7,000 hours of duration at 925°C. These results indicate both temperature and duration time are key factors affecting cathode degradation resulted from microstructure change. The cathode service life may be longer at lower operating temperatures.

The key activity for cathode development is to evaluate different cathode compositions to improve cathode microstructural stability. The challenge to evaluate new cathode materials to improve microstructural stability is that such a densification mechanism did not reveal itself until testing duration time is beyond 7,000~8000 hours depending on operating conditions. LGFCS developed an accelerated testing approach using cathode symmetrical button cells and have since transferred the approach to subscale cells. Under the accelerated testing conditions, cathode densification was repeated in as short as400 hours. Based on series of accelerated testing results, the thickness of densified cathode layer is associated with duration time when other testing conditions are fixed (Fig. 63) - the longer the duration time, the thicker the densified layer. Based on this relationship, cathode service life under real system conditions can be estimated. For example, 1200 hrs of testing under accelerated test conditions is equivalent to about 16,000 hrs of operation under system conditions. Candidates will be continually tested to determine their maximum service life based on accelerated testing.

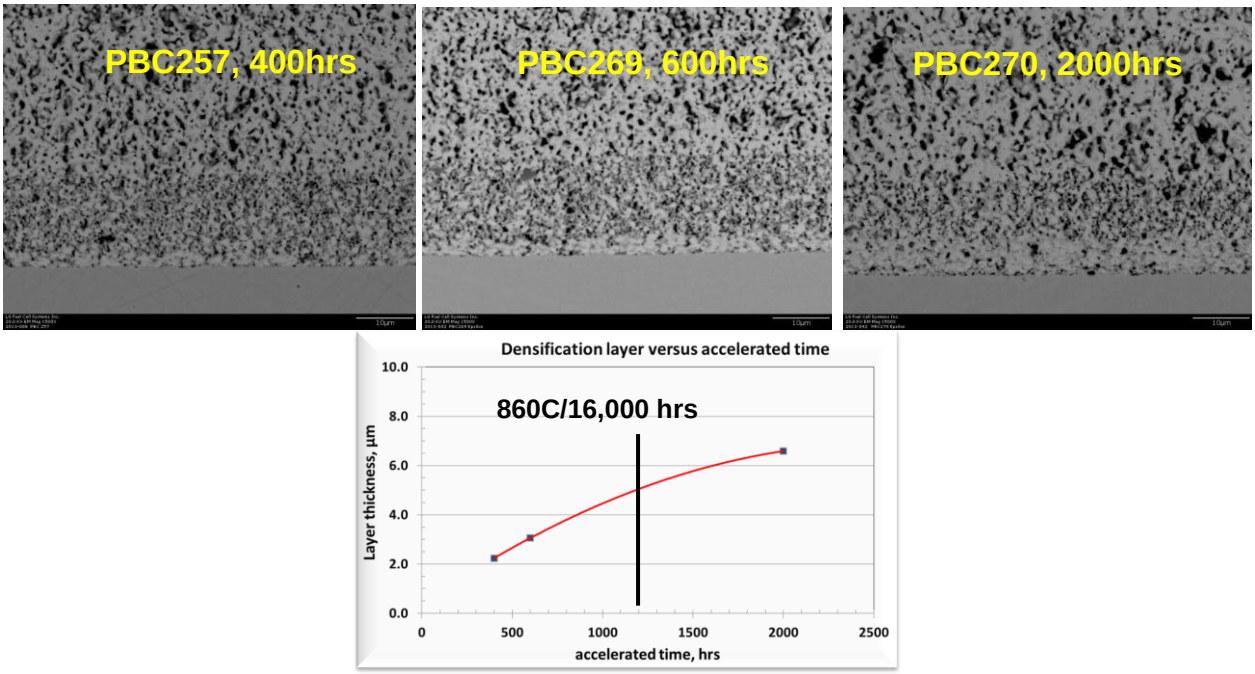

Figure 63. Epsilon cathode button cells SEM post-test analysis after accelerated tests and correlation plot between densification layer thickness and accelerated hours

The accelerated testing is an important tool in screening alternate cathodes for improved microstructure stability. Figure 64 shows two symmetrical cells, baseline vs. modified cathode, tested side-by-side under accelerated testing conditions. The modified cathode maintains a porous microstructure in contrast to the

baseline. To further validate this approach, a number of repeat tests have been accomplished in which the densification mechanism was well repeated.

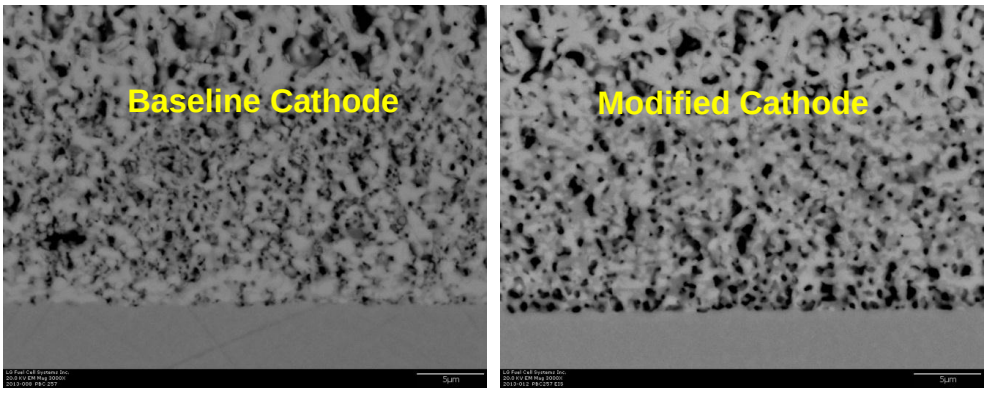

Fig. 64 SEM of symmetrical button cells after accelerated testing for 500 hours

Nickelate Cathodes: Since the LGFCS block is designed to operate at temperatures from 810°C to 910°C, there are benefits to lower stack block operating temperatures including reduction of fuel cell degradation mechanism caused by materials diffusion/migration and microstructure coarsening, and offering greater opportunities for the use of lower-cost balance of plant materials. However, LSM-based cathodes have high activation energy and its polarization increases significantly with decreasing temperatures. During the project periods, LGFCS has been investigating lower ASR cathode technologies to lower the block operating temperature for natural gas distributed power systems and/or improve the efficiency. This is a long-term goal for LGFCS's mature commercial product. LSCF is a widely accepted cathode for intermediate temperature SOFC stacks. However, its high CTE (~17 ppm/K) does not match that of the LGFCS substrate. Several trials were made for applying LSCF cathodes but cathode delamination and CCC selection for stability with the LCSF and CTE allowance was unsuccessful. The bar chart in Figure 65 compares polarization of different cathode materials at different temperatures. It can be seen that three different nickelate cathodes have much lower polarization than LSM and LSCF cathodes at 750°C.

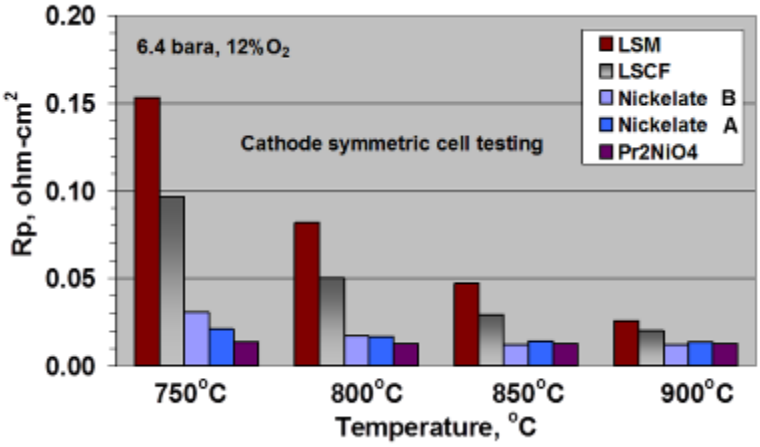

Figure 65 Comparison of cathode polarization.

The ASR benefits of the nickelate cathode is highlighted in Figure 66 with temperature sweeps being performed for single cells tested side-by-side in the same test rig. Two cells made from different nickelate

cathode compositions show lower average ASR at bundle mid-point temperature (860°C), 0.235 ohm-cm^2 vs. 0.32 ohm-cm^2 for LSM-based epsilon cathode at 1 bara.

Two primary challenges are being addressed for nickelate cathodes: (1) achieving phase stability during extended testing at block conditions and (2) optimizing the microstructure for improved triple point boundary density and contact with the ceria barrier layer. LGFCS has investigated in initial round of dopants that provided a degree of phase stability over straight Pr_2NiO_4 which for example decomposes quite readily into PrO_x, $PrNiO_x$ and NiO phases. Those doped nickelates are the Nickelate A and B shown in the bar graphs. A significant amount of testing at single-cell and 5-cell scale has been performed for those cathodes with favorable degradation trends as shown in Figure 67. However, post-test TEM analysis revealed that phase decomposition did exist, to a significant degree, even though ASR performance held up well. The goal is a nickelate with complete phase stability and therefore during the Phase 2 program the University of South Carolina (USC) was included as a subcontractor to investigate alternative dopants and doping levels to further enhance the phase stability. Nickelate studies by USC were focused on powder synthesis and phase analysis following ageing at 790°C and 870°C conditions,

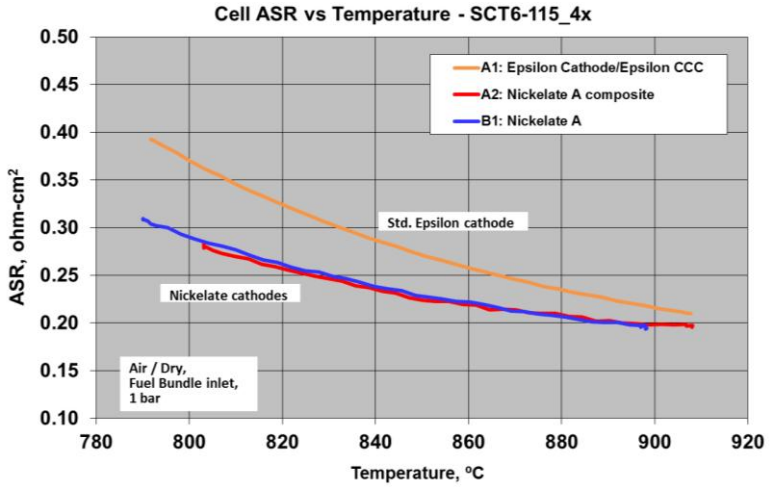

Figure 66. ASR benefits of nickelate cathodes over epsilon cell technology.

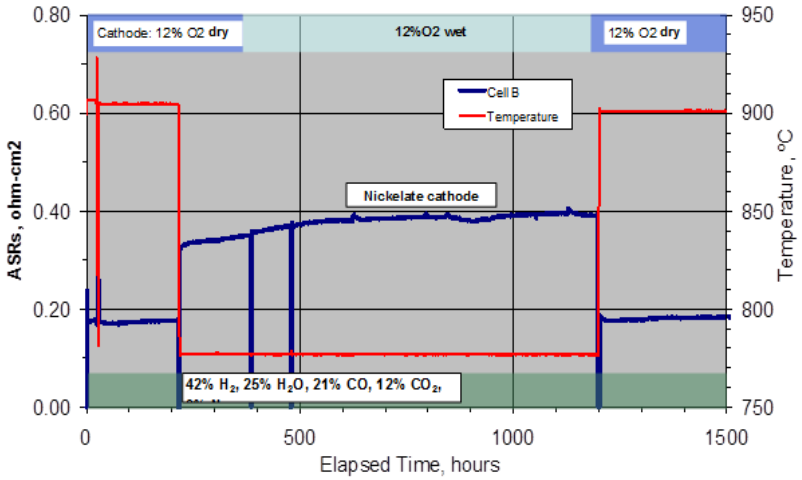

Figure 67. Early doped nickelate composition

representative of the anticipated temperature range for blocks incorporating nickelate cathodes, for 500 hours. Selected dopants identified by USC beyond those initially evaluated by LGFCS have improved the stability of this lower ASR class of cathodes, with no phase instability observed for a selected dopant at certain concentration levels. The identified compositions are beginning tested at LGFCS at the button cell and sub-scale level. Through the collaborative work with USC and the detailed TEM analysis of aged and electrochemically tested nickelate compositions by CWRU, we feel significant progress has made to understand the phase stability issues and solutions for the nickelates – these remain a promising class of cathodes for longer-term introduction given the large amount of durability testing and overall validation still required.

Historically, we've seen a poor interface between the nickelate cathode and the ceria barrier layer (Figure 68, left). Addition of a second phase (doped ceria) has resulted in improvement to the interface region (Figure 68, right). Subscale cell testing of nickelate composite cathodes showed some improvement in degradation versus the baseline epsilon LSM cathode at 800°C in the presence of moisture as shown in Figure 69 (left). Further, as shown in Figure 69 (right), comparing different nickelate and its composite cathodes, the compositional class A has lower ASR and degradation rate. Further optimization to improve degradation of nickelate A composite cathode is on-going. Promising results were achieved recently.

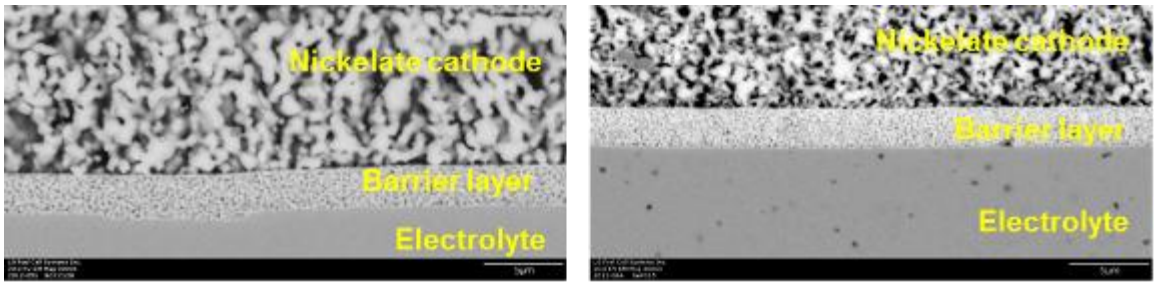

Figure 68. Improved nickelate cathode/doped ceria barrier interface, before (L) and after (R).

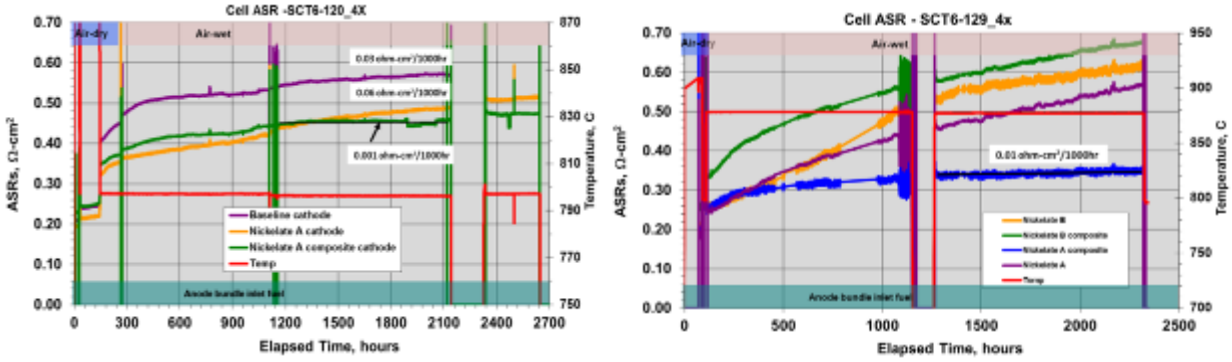

Figure 69. Nickelates vs epsilon LSM-based cathode durability at 800°C (left), nickelate and its composites durability at 870°C (right) with 3% cathode moisture.

Conclusion: LGFCS has reported that the degradation of the epsilon technology is dominated by cathode effects based on parametric AC impedance analysis, although anode degradation mechanisms also become significant at the high block temperatures and fuel outlet conditions. Key post-test analysis results of the standard cathode are the presence of the MnO_x phases and Mn-enrichment of zirconia surface and densification along the electrolyte. The key to selecting an optimized cathode for eventual entry-into-service products is relating reduced electrochemical degradation rates to lesser changes in the microstructure, phases and characteristics of surfaces in and around triple phase boundaries. Alternate

LSM cathode chemistries have shown less free MnOx and densification characteristics, and degradation rates, than the baseline epsilon cathode. The impact of Cr vapor species contamination from the balance of plant components is critical variable for including in the final screening of the cathode technology to meet the commercial degradation targets.

Nickelate cathodes remain a potential means for reducing the ASR and peak operating temperature of stacks and achieving the durability improvements necessary for eventual 5-year service life.

Task 5.1 – Subscale System Relevant Testing

Approach - At the start of the program it was important to establish the targets for cell performance (average ASR) and durability (degradation rate) to ensure efforts were properly directed at achieving outcomes which would result in a viable product technology. An effort was undertaken outside of the SECA phase I program that looked at the design space of cost and efficiency, and has targeted performance as defined by an average beginning-of-life ASR of 0.29 ohm-cm^2 and end-of-life ASR of 0.42 ohm-cm^2. This range of ASRs establishes the efficiency and stack requirement target for the fuel cell system product.

The degradation rate is a very important factor in the overall economics of a fuel cell system. With the above defined range of ASR for the life of the stack, the rate of ASR degradation can be determined to give a particular stack life. The use of an ASR degradation rate is preferable to a power degradation rate as it is more applicable to understanding how a system will operate in the field. Figure 70 below shows the effect of different degradation rate on plant operation. During the useful stack life, the plant will likely operate at a constant power level while efficiency is degraded. After the maximum average ASR is reached, further operation will require reducing the output power to maintain a constant heat release rate to balance the system operation. The SECA Phase I target of 2% power degradation per 1000 hours (assumed under constant current operation) is equivalent to an ASR degradation rate of 0.050 ohm-cm^2/1000 hours. At this rate, a plant could maintain constant power for less than 3000 hours. To achieve a 2 year stack life a rate of 0.008 ohm-cm^2/1000 hours is required, or to achieve a 5 year stack life a rate of 0.003 ohm-cm^2/1000 hours is required.

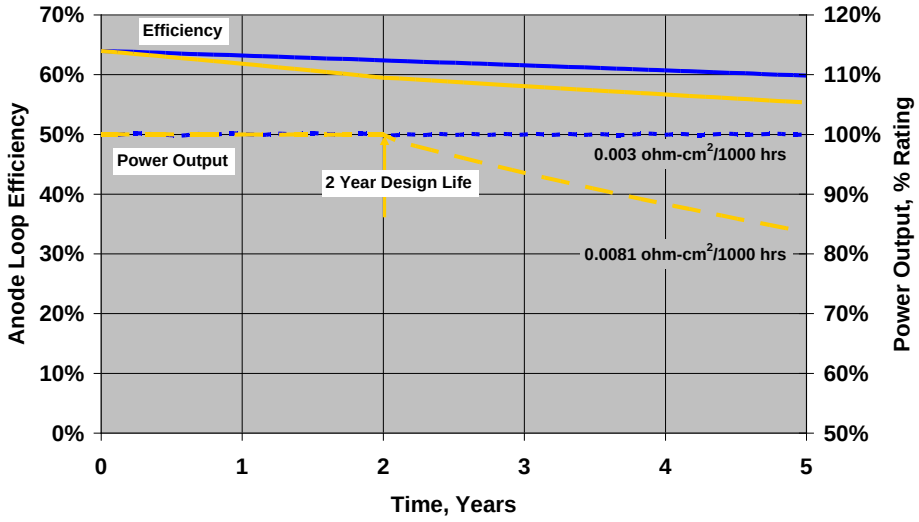

Figure 70. Plant operation for different degradation rates

The LGFCS technology plan is intended to progress from the current material set to a suitable entry-into-service (EIS) technology toward what is deemed a mature product (MP) technology based on performance and durability, including meeting the requirements for coal-based IGFC systems.
The majority of the durability database in Phases 1 and 2 has been based upon subscale five-cell samples, an example of which is shown in Figure 71, which allow for well controlled boundary conditions and the ability to make use of impedance analysis to investigate sources of degradation versus time. The sample is designed with anode and cathode voltage taps which can separate the voltages losses from the secondary interconnect (SIC, through which current flows to and from the tube), the primary interconnect (PIC, between cells), and the cells themselves. Tests have extended beyond 8,000 hours across the spectrum of temperatures experienced in operation, with some tests operating for over 16,000 hours. Many other tests were of shorter duration to allow interim post-test analysis.

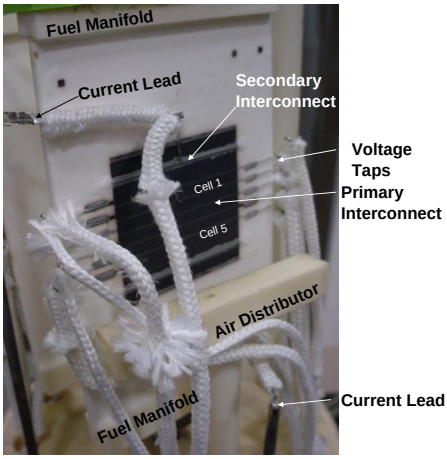

Figure 71. Five-cell sample with detailed voltage taps

Beyond 5-cell scale tests, the next size of scale for durability testing is 6-tube bundles. Two test platforms exist for testing single bundles; an atmospheric pressure test setup with dry air on the cathode, and a pressurized test stand with full capability to match system conditions (shown in Figure 72).

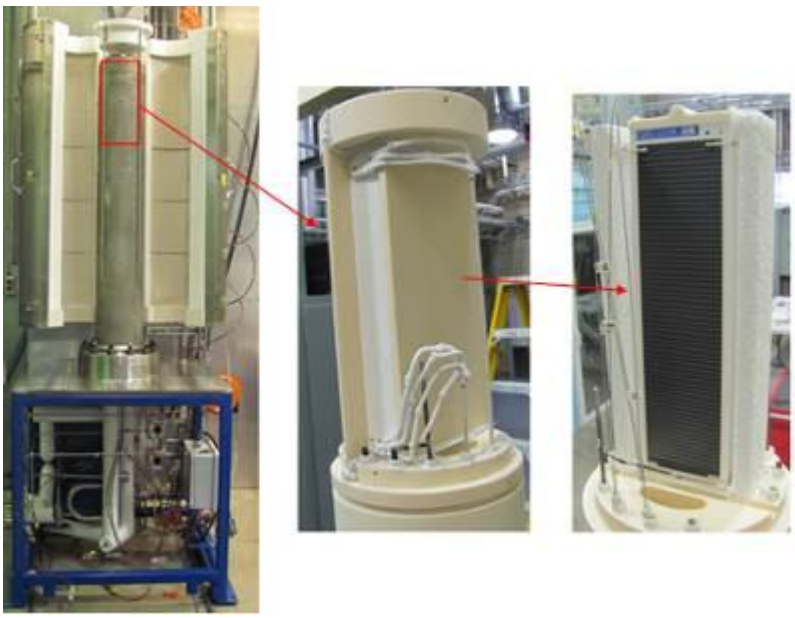

Figure 72. Pressurized bundle test stand for testing under fully system relevant conditions

A third platform which is used for durability is the atmospheric pressure triple bundle test (Fig. 73). This platform consists of three bundles in cathode flow series with independent fuel and electrical connections. Thus in this platform we get 60% of the cathode block conditions and the complete anode conditions.

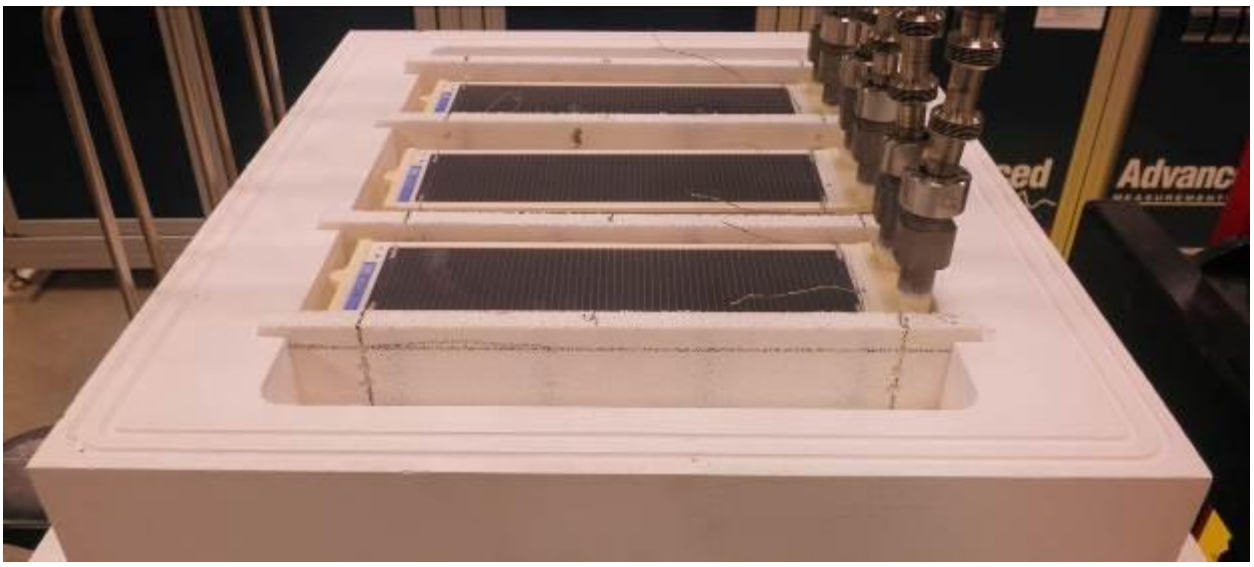

Figure 73. Atmospheric Pressure Triple Bundle Test Stand

It is important to note that the inherent scalability of the LGFCS technology lends itself to this approach. As the active area increases, or the number of cells are increased, the flows of current, fuel and (to a lesser extent) air are maintained. So by tracking the boundary conditions carefully the progression from smaller to larger is straightforward and predictable. This is demonstrated in Figure 74 which shows a progression of over 200x in active area results in a fairly tight cluster of results. In addition, the effect of pressure is also shown, which for this particular case resulted in a reduction in ASR of over 0.05 ohm-cm^2.

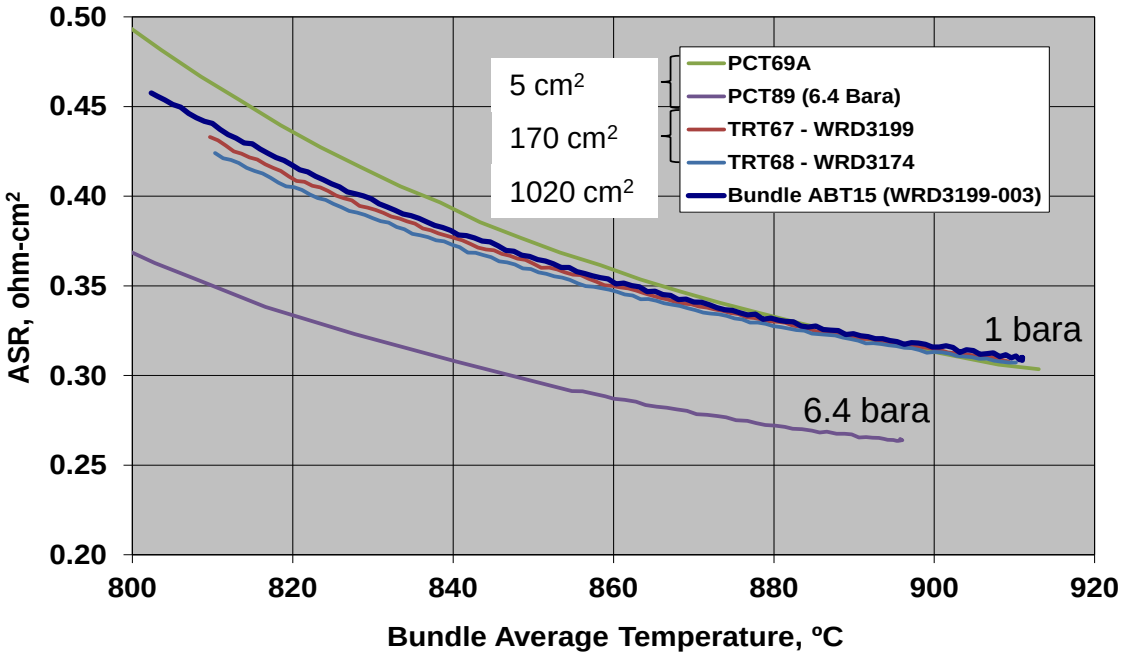

Figure 74. Comparison of 5-cell, tube, and bundle scales at 1 Bara, and the effect of pressure.

Results - The LGFCS system architecture develops a profile in which the parallel anode flow bundles experience a range cathode conditions from the inlet to the outlet of the block. At each strip, the anode side of each parallel bundle experiences the full range of fuel conditions at a given cathode condition. From this we define the four corners of the operating envelope including:

- Anode Inlet/Cathode Inlet
- Anode Outlet/Cathode Inlet
- Anode Inlet/Cathode Outlet
- Anode Outlet/Cathode Outlet

Durability performance was mapped across the four corners of the operating envelope using 5-cell, highly instrumented fuel cell tube samples under representative test conditions. Due to the high steam condition at the anode outlet, it was determined that this was the harshest condition on the anode side materials. The cathode side is a bit more complex. As discussed under Cathode Development (Subtask 4.3), there is a long period of stabilization (on the order of 1000 hours) at temperatures at the block inlet in which there is a rapid initial loss of performance followed by longer term low degradation. Performance is further degraded by the presence of cathode moisture. At higher temperature, the degradation rate was steady from the start of the test, but has shown to be higher than that experienced long-term at lower temperatures, especially for time frames of one to two years when cathode densification becomes an issue. Figure 75 shows the power density durability per repeat unit (RU), which is a cell plus primary interconnect, at three temperatures covering the operating range of a system block. In addition, the power trace from two 6-tube bundles tested at 860ºC for over 4000 hours are shown.

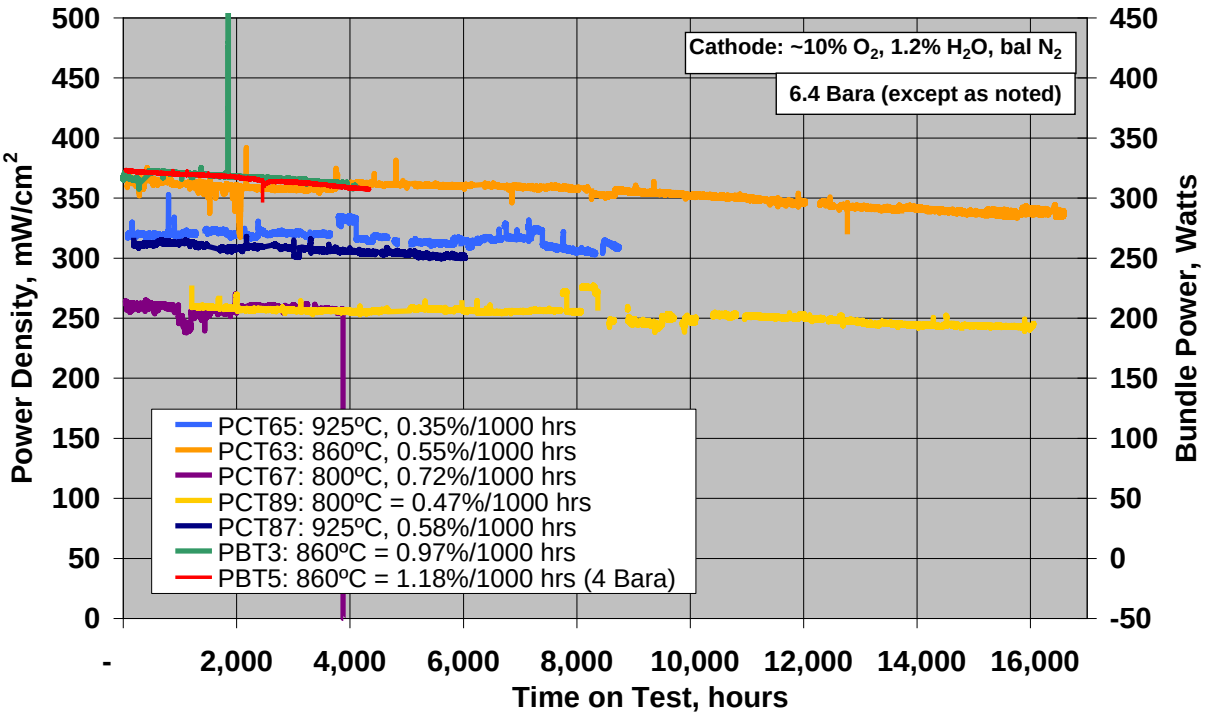

Figure 75 - Power density durability for 5-cell Samples over temperature envelope, and for two bundles at 860°C

Overall, the rate of degradation was much lower than the 2% power/1000 hour Phase 1 target, or 1.5%/1000 hour Phase 2 target. The rate of degradation for the bundles tested at the same pressure show

a slightly higher degradation than the 5-cell samples. There was an issue with PIC durability for bundles due to print defect which existed in these bundles but was later fixed. This will be discussed further later on in this section.

A map summarizing the durability testing over the operating envelope is shown in Figure 76. The green and red lines are a model generated ASR versus temperature curve which represent a starting ASR of 0.29 ohm-cm^2, and an end-of-life ASR of 0.42 ohm-cm^2, respectively. Data points are included from selected tests which show initial, final (or current), and projected ASR. The projections are based upon the final (or current) ASR and the degradation rate trend, cast forward to 2 years (~16,000 hours of operation). As shown, the higher degradation rates at the higher temperature range result in ASRs slightly outside of the projected band of stack life, while the low temperature end data is in range of the required performance. The projected stack life for the epsilon technology represented here is about 1-½ years.

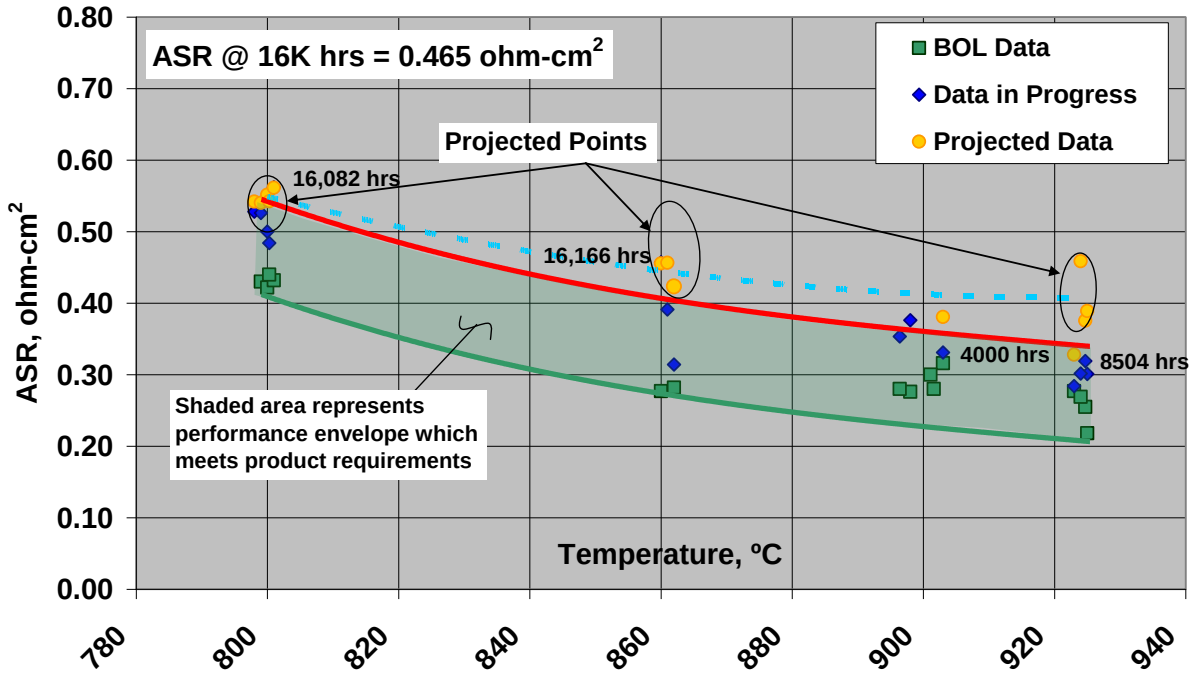

Figure 16. Map and projection of Phase 1 and 2 five-cell durability testing data

The process of improving the degradation performance requires developing an understanding of the sources of degradation. This understanding is acquired by:

- Steady-state data from detailed voltage taps
- AC Impedance Testing of cell performance versus time
- Post-test microstructural and material mapping

The breakdown of the contributions to degradation can be separated using the voltage taps into interconnect and active cell sources. The results of a long-term test performed at block average conditions of 860ºC and average anode/cathode compositions is shown in Figure 77 below. The degradation is primarily driven by the active cells, with a small contribution from the secondary interconnects (this is reflected in the "Tube" ASR) which is less than 0.001 ohm-cm^2/1000 hours. Note the impact of the SIC degradation over a full 60-cell tube will be further minimized. The primary interconnects are asymptotically improving during this time frame up to 8000 hours, and beginning to increase after 8000 hours. The mechanism of Ni transport from the ACC to the CCC side of the PIC is a

primary feature evidenced in the post-test analysis. While the durability was quite good over the two year test period, such issues will need to be further mitigated to achieve longer durability life, as was discussed in Section 4.1 above.

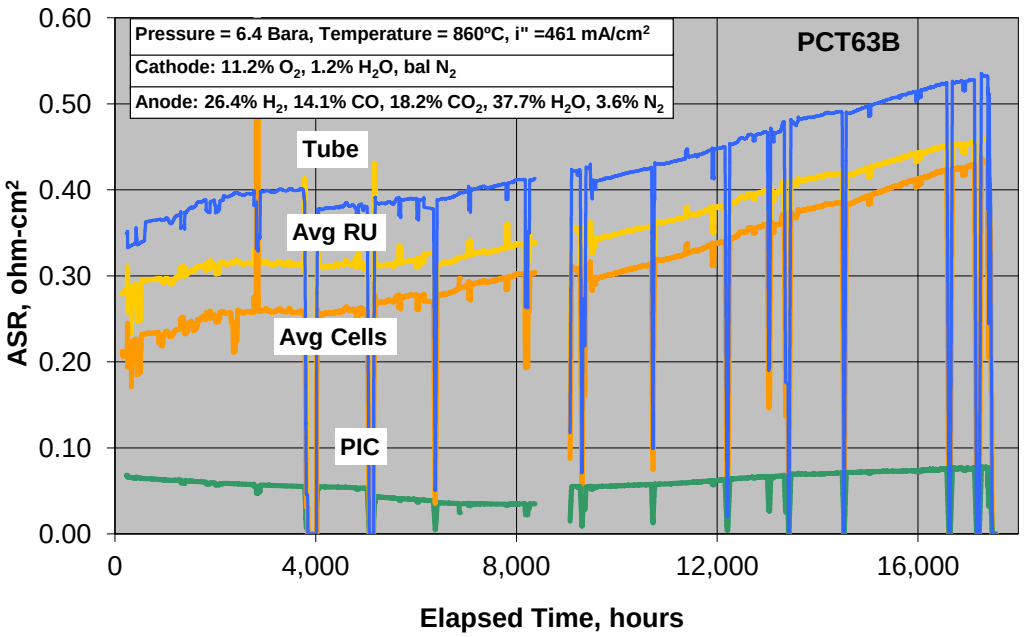

Figure 77. Five-Cell test showing component contributions to ASR degradation

While steady-state testing can give a breakdown of the major components of the losses, we need to further investigate where the changes are occurring in the cells themselves. Figure 9 shows two results demonstrating how AC impedance can be used to deconvolve the different components of the cell performance. First, 78(a) shows that by performing parametric variations of P_{O2} reveals that the middle peak is dominated by the cathode response, thus indicating that the degradation shown in Figure 78(b) may be due to the cathode activation changing. Second, the high frequency, left most x-axis intercept shows the ohmic resistance of the cell. In (b) we see that this is generally unchanged with exception of the first trace, which is likely a test artifact (not real). Such analysis allows focusing of efforts toward finding and improving the mechanisms affecting cathode behavior.

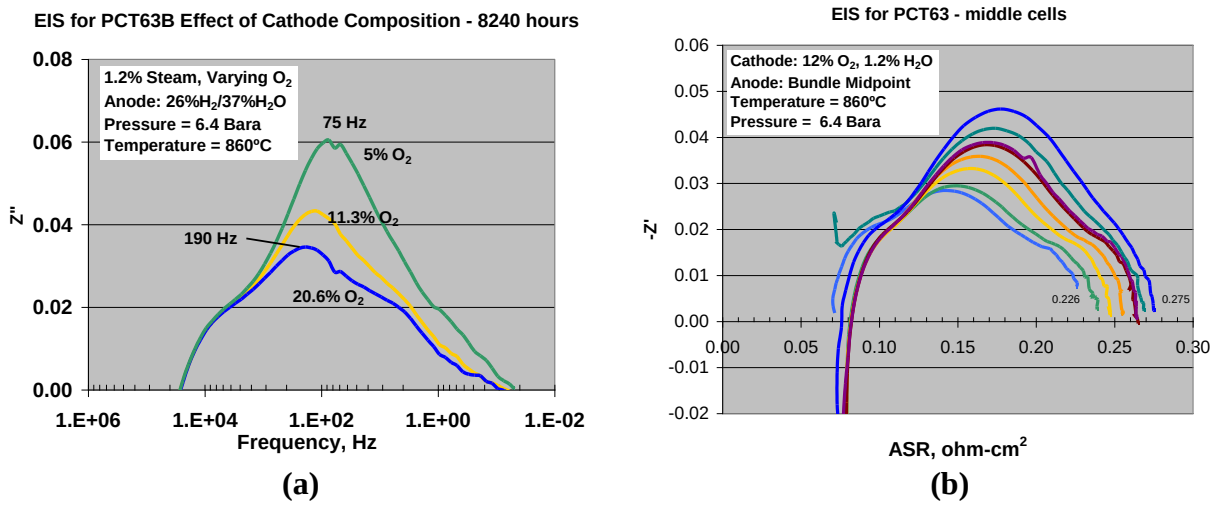

Figure 78. AC Impedance Results (a) Effect of PO2, (b) Effect of Time

In addition to deconvolving a single test, AC impedance can also help understand how degradation changes over different conditions. Figure 79 below shows the AC impedance trace of 3 tests, each run for at least 4000 hours at 800ºC, 860ºC, and 925ºC respectively. The three tests were taken to the same condition and AC impedance data acquired. The results show that the fundamental degradation is higher at 925ºC than at 860 or 800ºC, and that the cathode appears to dominate the degradation, although degradation in the higher frequency range (to the left-hand side) is also evident which may be attributable to anode degradation. The work to specify and mitigate the specific mechanisms was discussed in Sections 4.2 and 4.3 above.

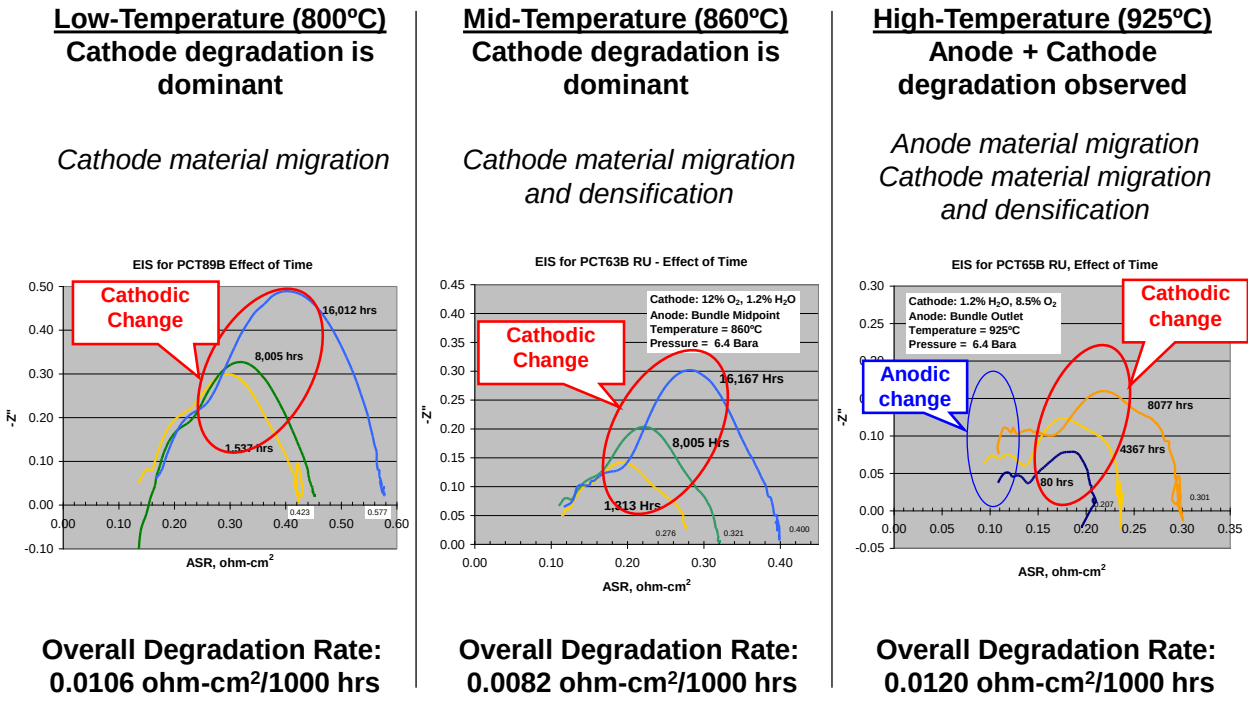

Figure 79. Identification of key degradation mechanisms over the operating temperature range

Testing of different cathode formulations at high and low temperature, and testing of improved anodes at high temperature and fuel utilization has progressed over the past two years. Impedance data is taken at approximately 1000 hour intervals. Using RC circuit modeling, resistance, capacitance, and Warburg elements are used to represent the impedance behavior. Estimates of degradation contributions can then be charted over the life of the test. An example is shown in Figure 80.

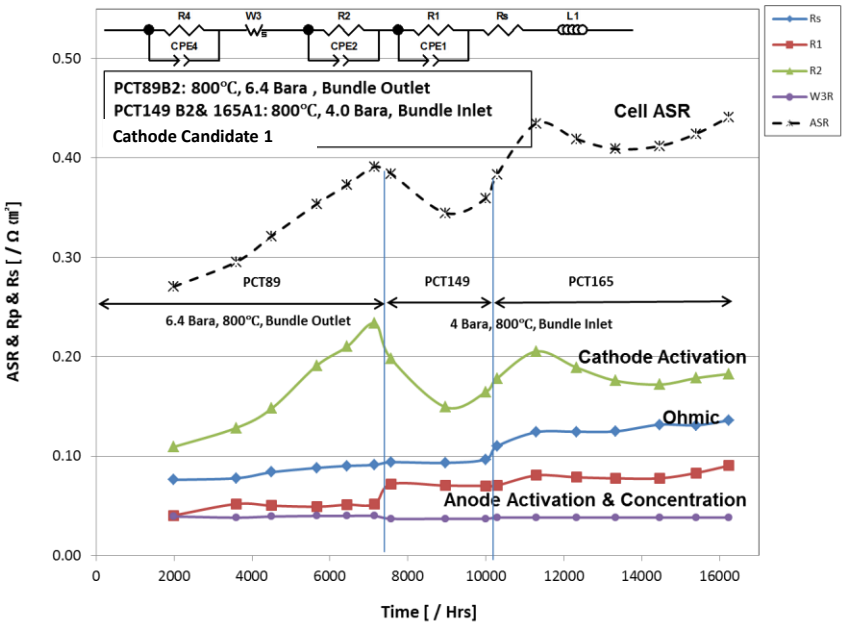

Figure 80. Example of assignment of degradation contributions over time using RQ modeling

The compilation of data long-term cathode testing at 800C is shown in Figure 81. This data shows a clear improvement in performance for the different candidate cathodes compared to the baseline cathode at this condition. The rate of degradation of the 4 cathodes are:

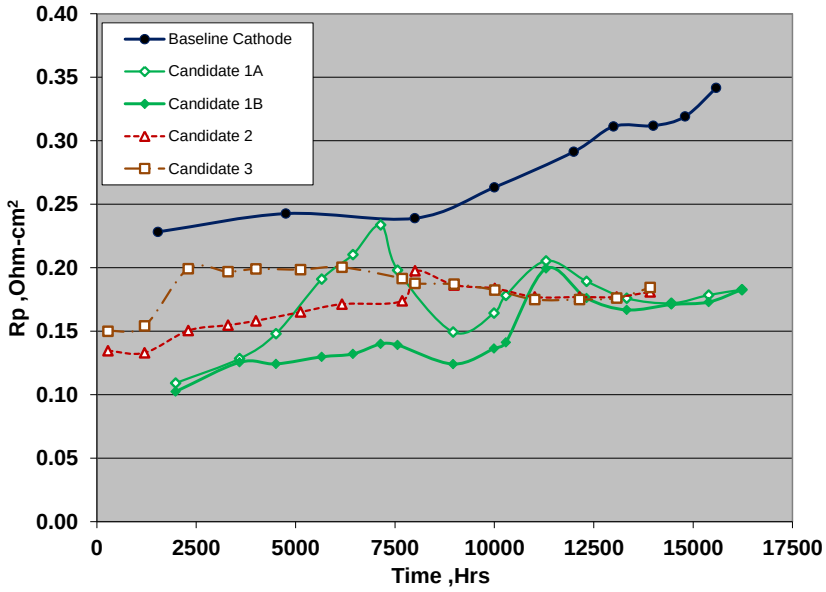

Baseline: 8.5 μΩ-cm^2/hr
Candidate 1: 5.7 μΩ-cm^2/hr
Candidate 2: 3.4 μΩ-cm^2/hr
Candidate 3: 2.5 μΩ-cm^2/hr

Figure 81. Comparison of cathode activation Rp change versus time for 4 cathodes at 800°C

Figure 82 shows a comparison of all of the degradation components for the test which ran 16,000 hours. The comparison shows that the cathode performance and durability are both improved for the cathode candidate 1 cells, although the overall degradation rate was similar for the two samples.

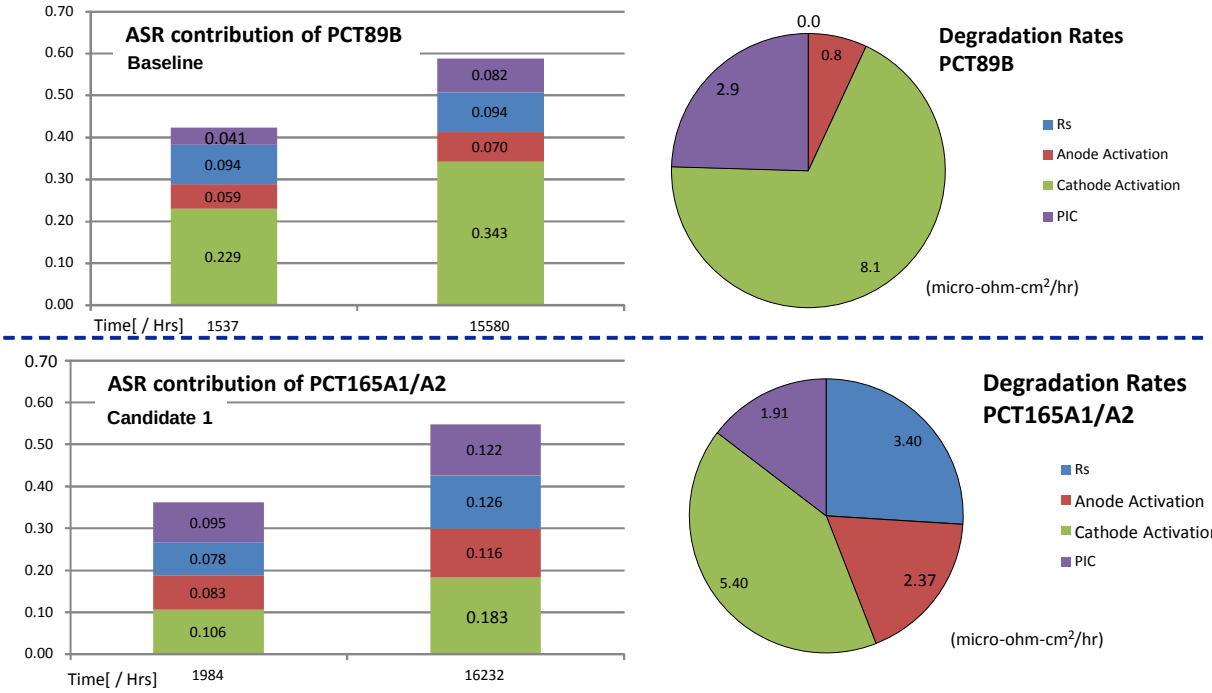

Figure 82 - Comparison of degradation contributions for two tests at 800ºC

Long-term cathode material studies at higher temperatures have shown less obvious benefit of the candidate cathodes in tests up to 8000 hours, as shown in Figure 83. When tested in a rig which included a chrome bearing preheat coil, the results are less promising. It has been determined, however, that the amount of Cr which is picked up by samples in this test setup is higher than what is expected to be seen in actual block hardware. Because of this, a new Cr testing protocol is being developed to provide a more realistic rate of Cr exposure. This is discussed further below.

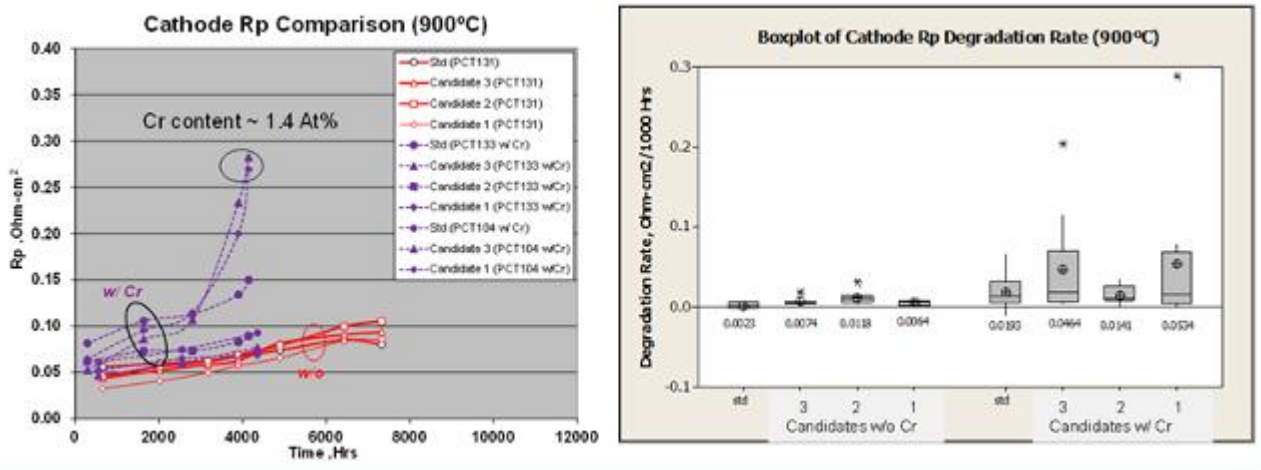

Figure 83. Comparison of cathode activation degradation at 900C with and without Cr present

Chrome Contaminant Testing: Early testing with chrome present on the cathode stream was not definitive as the chrome levels produced by the test rig in use are dependent upon temperature and time of exposure. For tests at temperatures less than 860ºC, and durations lasting 2000 hours or less there appeared to be no impact of Cr contamination on durability performance.

Subsequent testing at 900ºC with chrome in the cathode gas stream has been conducted for multiple cathode samples over 3 different test runs. The results are shown in Figure 84 with the cathode activation degradation plotted as a function of the chrome adsorption rate. The chrome rate was calculated based upon the chrome atomic percent measured at the cathode electrolyte interface post-test which was then divided by the time each test was on stream. The data does not correlate very well, possibly due to other variability in test samples.

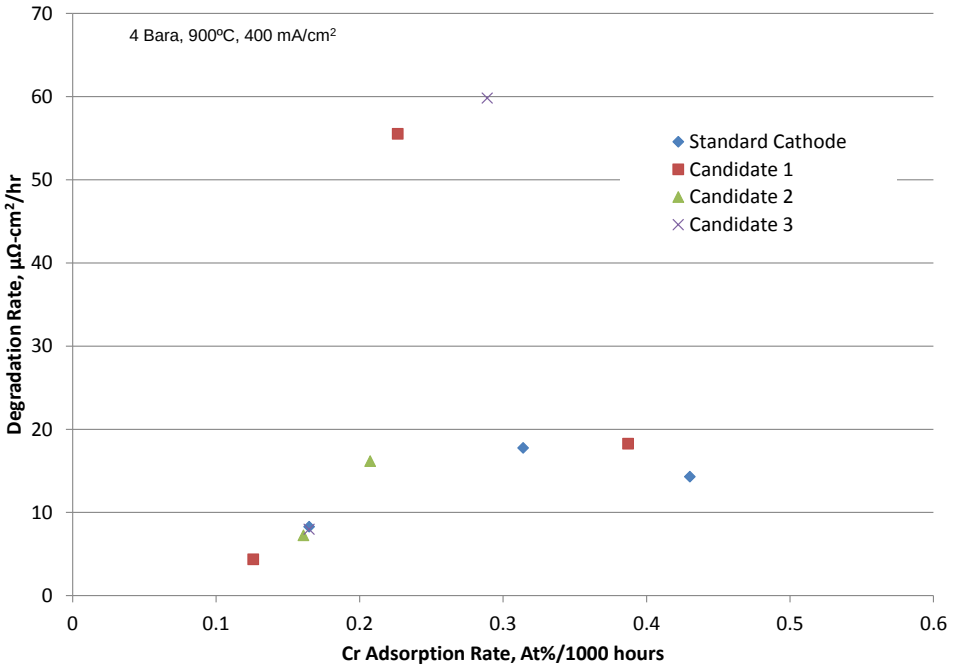

Figure 84. Comparison of cathode degradation rate versus Cr adsorption rate

Figure 85 shows the breakdown of the ASR contributions for a 7000 hour test of a sample with a single layer anode at 925C and bundle outlet conditions. This showed an overall degradation rate of only 5.5 micro-ohm-cm^2/hr (0.0055 ohm-cm^2/1000 hours), a rate commensurate with a 3-year life. Unfortunately this test ended prematurely due to a rig issue. However a bundle test is planned which will combine the improved cathode and anode technology together.

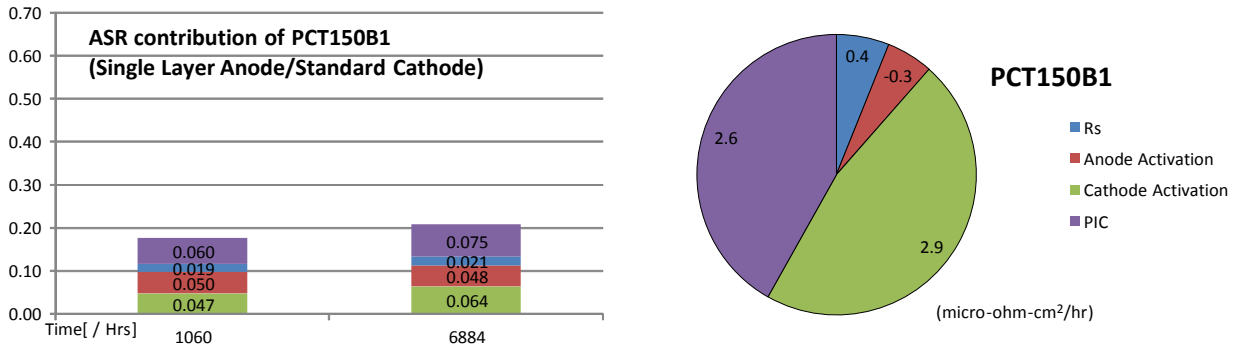

Figure 85. ASR contributions for a test at high temperature of a single layer anode for 7000 hours at 925ºC and bundle outlet fuel

Bundle Testing: Testing was also performed at bundle scale both at 1 atmosphere and 4 or 6.4 Bara pressure to compare degradation performance across scales. The initial performance comparison was very good, but as mentioned above, the degradation was somewhat higher at bundle scale, and even worse yet at 1 atmosphere compared to pressurized operation, as shown in Figure 86. The difference was traced to a PIC design change made for full-scale tubes to minimize CCC to CCC short during printing that led to an increased resistance across the PIC.

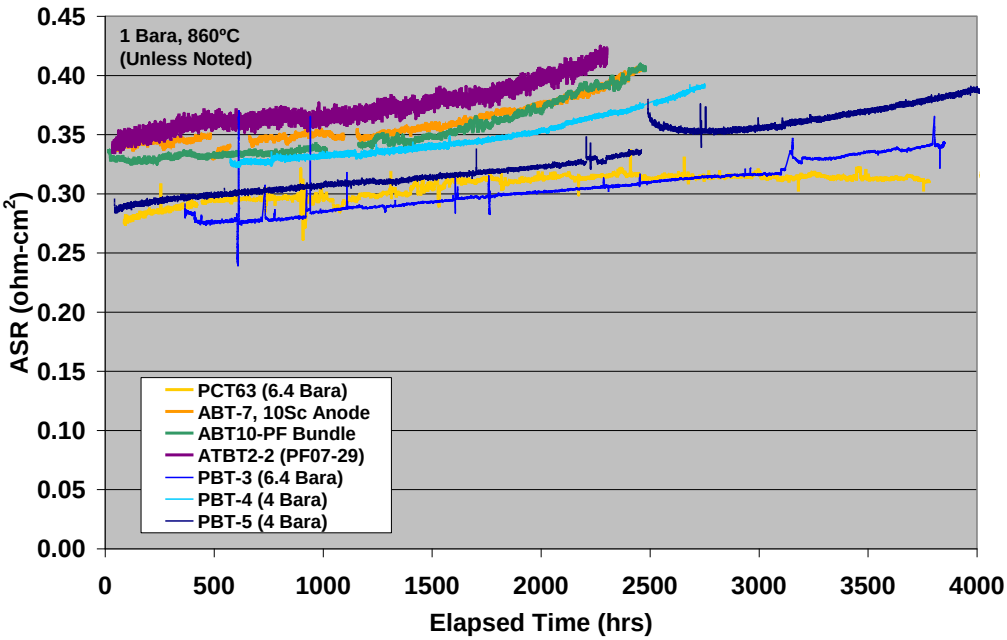

Figure 86 - Comparison of atmospheric and pressurized bundle tests

Triple Bundle Testing: Triple bundle durability tests offer the advantage of covering 3/5's of the cathode temperature range along with the full anode composition range in a single test article. Three bundles with candidate cathodes were tested for a period lasting more than 5000 hours. Figure 87 shows the initial V-I

curves and temperature sweeps for each of the bundles at the start of the test, demonstrating good repeatability of the manufactured articles.

Figure 88 shows the durability performance of the three bundles, for which the durability of the three bundles averaged about 7 micro-ohm-cm^2/hour. This rate would project to a life of greater than 2 years. Note that the coldest bundle having the highest rate of degradation is consistent with other tests over a similar time period. It is expected that the rate of degradation at the cooler end would become less over time as the bundle performance remains stable. Future testing will include improved anode and PIC along with selected candidate cathodes, which combined should enable durability approaching 3 years.

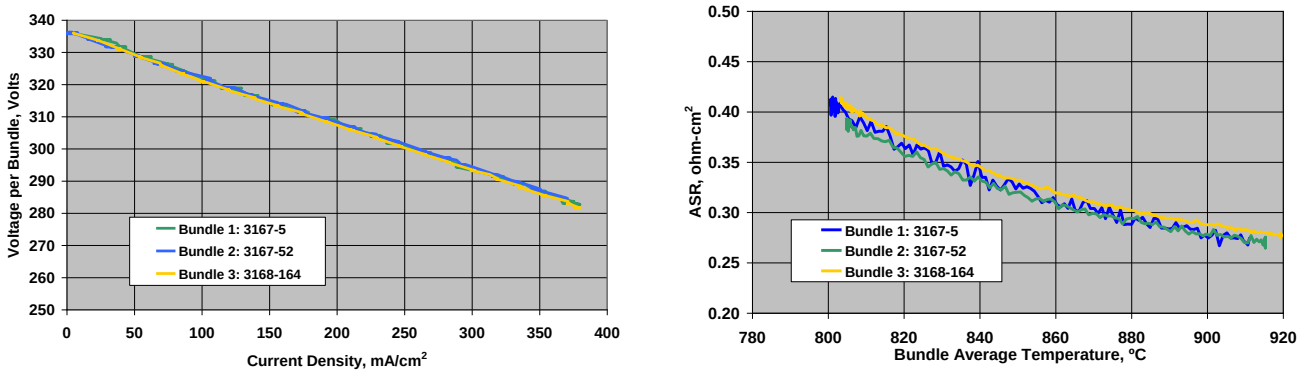

Figure 87 - Triple bundle test initial V-I curve and temperature sweep for each bundle

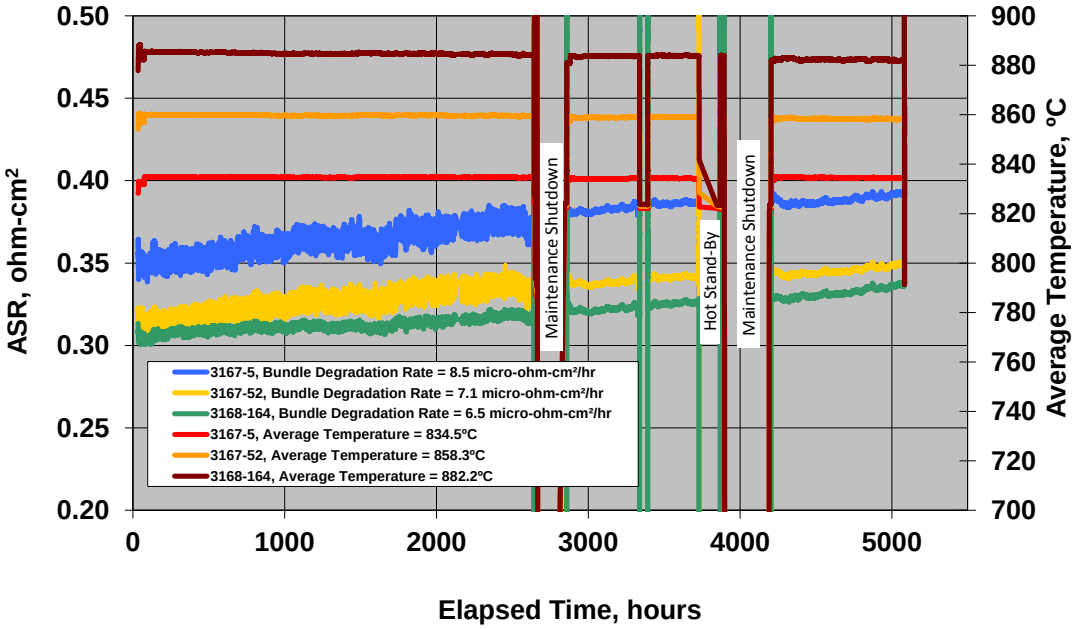

Figure 88. Durability test of triple bundle test with candidate cathodes for over 5000 hours.

Conclusions – LGFCS has developed an effective durability program relying on different scales of test samples to identify and understand key degradation mechanisms. The cell durability has increased as different degradation mechanisms have been identified and mitigated. The Phase 1 and 2 durability testing has shown that the technology developed over the past 5 years has gone from a projected durability of 1-½ years to greater than 2 years demonstrated at bundle scale and potentially 3 years at

penta-cell scale. Potential mechanisms have being identified and solutions to further improve long-term stability are being explored with the goal of extending service life ultimately to 5 years.

Task 5.2 – Stack Test Stand Preparation

Approach – The three block-scale tests scheduled under this program utilize pressurized test rigs originally developed outside of the SECA program. Three block test stands are present in Derby, UK and one in Canton, Ohio. The assembly of the pressurized block (stack) test stand in Canton was supported through an Ohio Department of Development program with cost share provided by LGFCS. The SECA program has supported design modifications of the stand from its original purpose of testing a distributed energy natural gas cycle to being able to simulate an IGFC system cycle and fuel composition and supported the acquisition of the necessary hardware for supplying a simulated coal syngas fuel as well as the commissioning of the test rig.

Results and Discussion –LGFCS currently does not run its stacks with on-cell reforming and relies on external steam reforming within the SOFC module. For the Phase 1 test in Canton, the external steam reformer was removed from the Canton block test stand internals to simplify it since one of the objectives for the block design was to make this test, as much as possible, strictly a stack test versus a combined stack plus systems test. The Phase I metric test was thus designed to be run with a single pass on the fuel side and the inlet fuel composition was representative of the post-reformer composition with an appropriate recycle ratio as designed for the MW-scale system. A key feature of the test stand was the Oxy-CPOX reactor. It used natural gas, carbon dioxide, steam, and oxygen to generate the natural gas or simulated coal syngas. The reactor's operation was designed to avoid any short-term, high oxygen partial pressure conditions that could oxidize the anode while enabling long-term operation of the catalyst in the Oxy-CPOX reactor. The operation of the Oxy-CPOX reactor was verified during mechanical commissioning during Phase 1.

The UK block test rig (Figure 89) used for the Phase II metric test matches the MW-scale system cycle, and is in fact termed a mini-tier rig as it matches the basic design features of the 250 kW pressurized tier but contains a single block being the repeat unit within the 250 kW tier. The UK block rig contain representative ejectors, reformers, heat exchanger, off-gas burner and insulation packages as that of planned 250 kW generator modules and as such contain a representative environment with respect to contaminants such as chromium and silica. The UK rigs for the SECA tests run on bulk methane rather than a natural gas feed. The Phase II program has the added requirement that the metric test be performed in a thermal self-sustaining manner. When testing at the single-block level the mini-tier does not include a turbogenerator so the recovery of off-gas combustor energy at the turbine, and subsequent pre-heating of ambient air by the compressor is not present. For testing at the single block level the portion of the off-gas combustor heat not transferred to the cathode air through the heat exchanger (just downstream of cathode air circulator) is discharged through the test rig exhaust pipe. The incoming cathode air is pre-heated using an electrical air heater. This is illustrated in Figure 89.

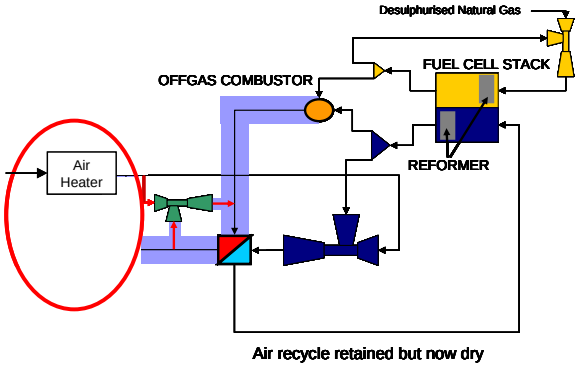

Figure 89. UK block test stand configuration with single block

In addition to making up for the absence of the heat of compression provided by the turbogenerator the electric air pre-heat requirement must also account for excessive heat losses from the test rig due to the relatively high pressure vessel surface area per block, and due to a high number of penetrations for instrumentation and experimental equipment compared to a full-scale product. Heat losses from the mini-tier have been estimated from data gathered during dry-cycle testing and is based on all mass flows into, and out of the mini-tier, and the thermal power of the off-gas burner and air heaters. Based on those data approximately 3.7kW are lost through the walls of the pressure vessel and penetrations. Due to the high heat loss for the mini-tiers an additional 2.04 kW of air preheating is required to maintain stack temperatures whilst offsetting the 3.7 kW lost through the pressure vessel walls and penetrations.

The equivalent heat loss from a full-scale generator module having a smaller vessel surface area per block, and fewer penetrations, is estimated to be approximately 1.6kW (roughly 2.1kW per block less than the losses in the mini-tier rig). Therefore in a full-scale generator module no additional preheating is required and the cycle is thermally self-sustaining.

Balance of plant chromium species mitigation: Although the LGFCS stack in all-ceramic, there is a significant amount of metallic balance of plant hardware that is a source of chromium contamination. A subcontract with the University of Connecticut explored chromium volatilization from the various alloys and coatings for consideration for balance of plant components. The objective is to screen alloys for their degree of chromium volatilization and the benefits of aluminized coatings. Figure 90 gives a sampling of the volatilization measurements made. The test methodology was first validated using chromium oxide powder and matching literature volatilization measurements. The benefit of alumina forming alloys was apparent, especially the Aluchrom alloys, but high quality pack cementation of vapor deposited alloys on other wise high chromium alloys was also shown to be very effective with volatilization rates even less than Aluchrom. An AFA alumina alloy (OC-4) developed at ORNL was also examined but the volatilization was significantly (~1 order) higher than that of Aluchrom.

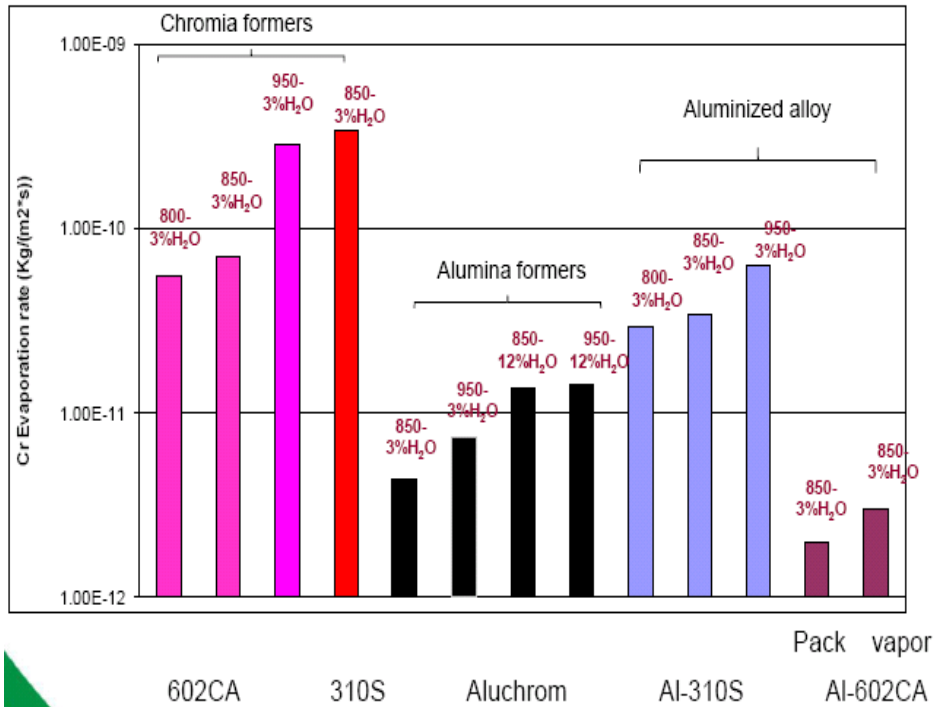

Figure 90. Chromium species release rates for select alloys/coatings

There was a slight difference in the block rigs used for the metric tests. The UK rigs was modified to what is termed an "open loop cycle" referring to the auxillary ejector for the OBG/heat exchanger loop and the cathode ejector secondary open to the rig tier volume. This results in the cathode loop at a higher pressure than the tier volume and leaks into the tier, minimizing the amount of tier surface exposed to the cathode flow and thus in theory the potential for less chromium volatile species passing through the active SOFC block. The Canton rig retained an original "closed loop cycle" in which the cathode flow was exposed to metallic surface of the tier and exterior surfaces of the block proving opportunities for greater chromium pickup, as well as silica from the tier insulation. The general configuration of the block for the Phase 1 test is shown in Figure 91. Because of this feature some chromium gettering features were added into the cathode inlet for the Phase 1 test and selected metallic surfaces were aluminized. UCONN supported the quality evaluation of the aluminized surfaces and confirmed the gettering efficacy of the materials selected for the block test.

Figure 91. Block configuration for "closed loop cycle" in which cathode air flows from the tier through the stacks

Conclusion – A total of two stack test stands have been modified for running SECA stack tests ranging in power output (NOC) between ~ 7.6 kW (2-strip) for Phase 1 and ~19 kW (5-strip) for Phase 2 using epsilon technology. These test rigs are representative of full system operation conditions and are thermally self-sustaining, meeting SECA Phase 2 requirements.

Task 5.3 - Stack Metric Testing

Approach – This task involves the execution of the block-scale metric tests. During the program period two block-scale test have been run: a the 2-strip (7.6 kW) Phase 1 test and a 5-strip (19 kW) Phase 2 test. Both test were run under a fuel representative of that for a distributed generation natural gas system with the Phase 1 test fed by a natural gas Oxy-CPOX reactor and the Phase 2 test using bulk methane. The tests were run under constant current conditions.

Results and Discussion –

Phase 1 Metric Test - The Phase 1 test was comprised of fewer strips than originally planned because of substrate supply issues occurring at the time from the sole vendor and yield issues upon initial reduction of the strips. The initial performance of the two strips was as expected (Table 8) based on a similarly pressurized bundle test. The durability results for the Phase 1 test comprised on the epsilon cell technology is shown in Figure 92.

Table 8. Performance comparison of Phase 1 metric test strips 2 and 3 to PBT4 bundle result

Test	PBT4	T1406 – S2	T1406 – S3
Avg Temp	860ºC	844ºC	870ºC
Power	321 W	318.2 W	320 W
ASR, Ω-cm²	0.315	0.364-0.375	0.308-0.331
Flams Out	24.5%	28.8%	25.8%

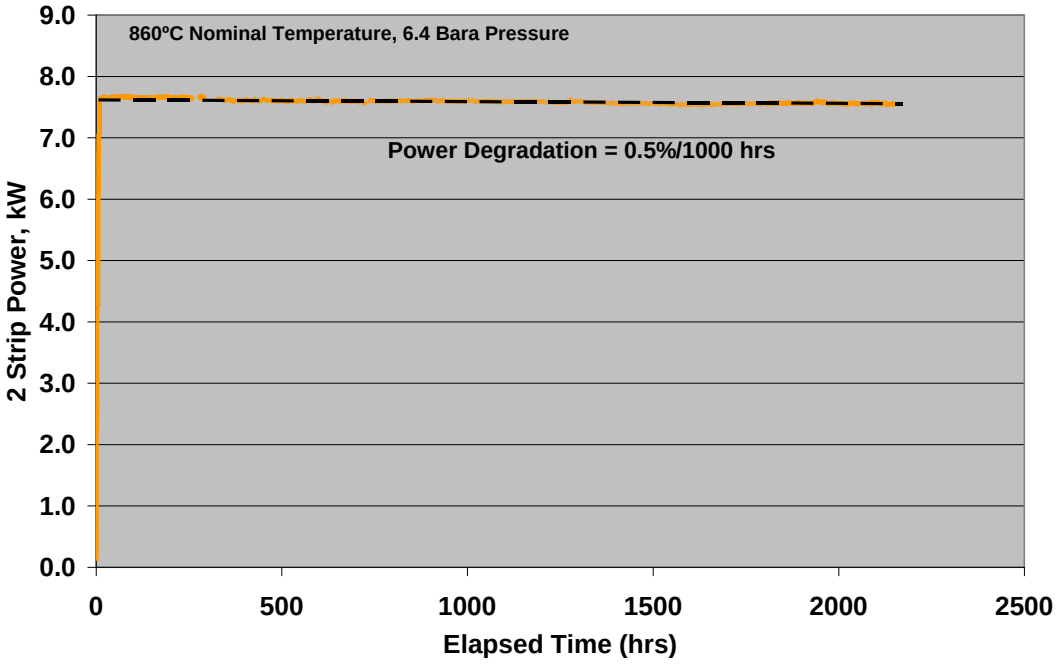

Figure 92. Durability result for the 2-strip Phase 1 test

The Phase 1 metric test ran smoothly until 2135 hours on load at which time a slight drop in power was observed; 120W out of 7420W combined for the 2 epsilon strips. Coincident with the drop in power was measurement of localized heating between the strips. The test was shutdown to diagnosis the problem. Post-test leakage measurement of the strips while still in the block box revealed damage to the strips. Upon removal from the block box some substrates were observed to have cracks. The damage appeared to have originated from a single location of strip 2, and resulted in some downstream damage to strip 3.

Root cause analysis was performed to determine the cause of the tube cracks. The prevailing theory is that a short circuit at a secondary interconnect (SIC) position occurred between adjacent tubes leading to local fuel consumption and heating causing a thermal stress state resulting in mechanical failure of a substrate based on the root cause conclusions from the initial Phase 2 test (see below). The SIC-to-SIC positioning for adjacent tubes has been redesigned to avoid this sort of failure in the future.

The degradation rate observed over the 2135 hours was promising in that the block test rig was operated with a high moisture content of 3-4% within the cathode as the result of the need for off-gas combustion of hydrogen to maintain the appropriate heat balance for the rig with the operation of only 2 strips. Such a high moisture can contribute to high chromium vapor species as well as silica species for the cycle configuration of the Canton rig. The getter strip did contain high capture of these species, but post—test analysis of cells from the test showed a chromium content measured at 0.43 at% on average across the cathode layers, somewhat elevated at the cathode-electrolyte interface.

Phase 2 Metric Test: The 5 epsilon strips for the Phase 2 were the first strips to undergo a pre-reduction cycle in a specialized test rig designed to measure voltage on all 12 bundles within a strip prior to committing the strips for build-up into a stack block. The rig also allows gas sampling at temperature with fuel flow to assess leakage/parasitic currents at the strip level. Historically, strips have been reduced within the stack block test rigs following the initial heating cycle. The strip pre-reduction rig now allows a quality check on the strips. This quality check would have caught the tertiary interconnect issue that caused the delay in the start of Phase 1 and 2 metric tests. Results for the minimum and maximum open

circuit voltages measured for each strip along with leakage rates are show in Table 9. All strips showed a low skew in OCV and low leakage rates.

Table 9. Results from pre-reduction of 5 strips supplied the Phase 2 metric test

Mfg #	ESR4R	ESR9	ESR10	ESR6R	ESR8R
T1314 (Phase 2)	Strip 1	Strip 2	Strip 3	Strip 4	Strip 5
Average OCV (Volts)	353.7	349.6	348.9	349.4	351.4
Max	357.5	353.7	352.2	352.9	354.8
Min	350.7	346.8	347.1	346.4	349.2
Max-Min	6.8	6.9	5.1	6.5	5.6
Post Test Leakage (sccm)	27	35	25	58	63

The Phase 2 test ran for 3043 hours under load (Figure 93). The first 335 hours were at less than design point because of mass flow controller and current limiter issues with the test rig. The constant current degradation rate was 1.1%/1000 hours, even with a known print defect that led to higher degradation of the primary interconnect region. The higher degradation rate than the 2-strip Phase 1 test is attributed to the greater temperature range present in a 5-strip test in combination with the materials migration associated with the print defect.

Post-test analysis of the Phase 2 test revealed chromium levels on average at 0.2 at%, somewhat lower than the shorter duration Phase 1 test. Chromium levels were slightly higher within strip position 1. LGFCS will be documenting chromium levels for block tests and seeking a correlation to degradation trends to guide block designs and chromium mitigation schemes and to accurately select preferred cathodes for entry-into-service systems. Post-test 4-point flexure testing of tubes from the Phase 1 and Phase 2 tests showed no evidence of strength reduction, providing further confidence in the MMA substrate material.

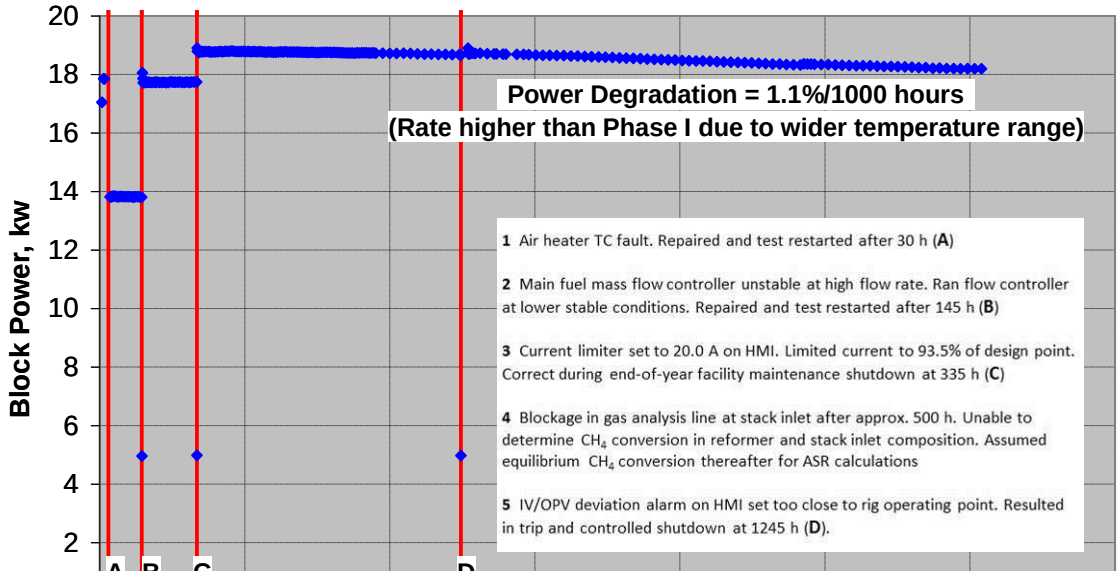

Figure 93. Cumulative power trends for the Phase 2 test

The print defect was discovered in a triple bundle test (ATBT2) running within a similar time period as the Phase 2 block test. The ASR degradation of the highest temperature bundle in that test is shown in Figure 94 - the printed substrates of that test were of the same vintage as the substrates built into the Phase 2 strips. Root cause analysis of the triple bundle test revealed the degradation mechanism and a single bundle test (ABT12) and a triple bundle test (ATBT3) were run at similar high temperatures to validate correction of the degradation source.

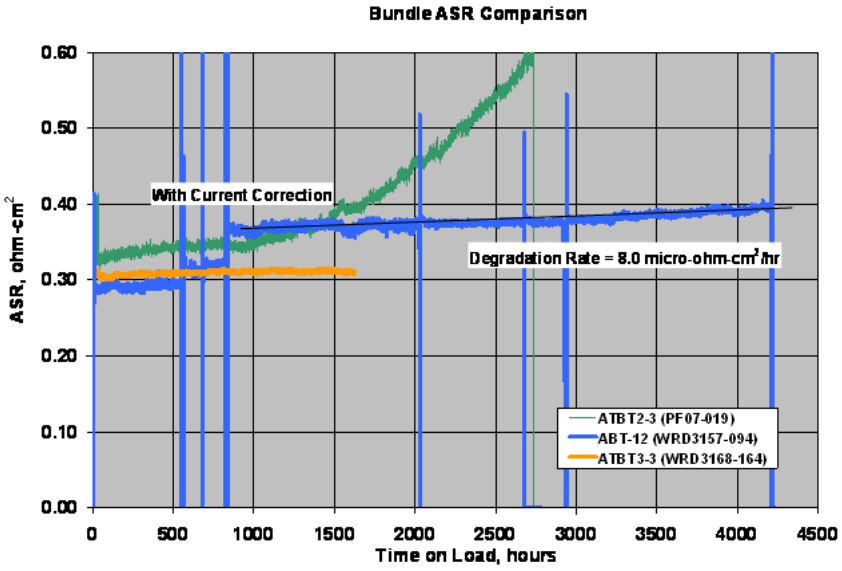

Figure 94. Bundle tests with and without the PIC degradation present in the Phase 2 block test.

Phase B Metric Test: An additional block test was added to the program with the program's extension. This test is a 4 strip test at ~15kW and the strips include selected alternate LSM cathodes distributed at half-strip level to compare the degradation of the various candidates at full scale and within the fully representative block environment with the associated contaminants. The quality of the strips was good based on pre-reduction results (Table 10). This test was delayed as a result of strip component supply for strip build and the requirement for root cause understanding of some residual cracks observed in a manufactured strip before committing all strips to a business critical and SECA program milestone test. Resolution of the strip residual crack occurrence was completed supported by detailed stress finite element analysis and the strip repaired. The test will be run under a follow-on program DE-FE0012077.

Table 10. Results from pre-reduction of 4 strips supplied the Phase 2B metric test

Mfg #	ESR11	ESR12	ESR13	ESR14
T1315 (Phase 2B)	Strip 1	Strip 2	Strip 3	Strip 4
Average OCV (Volts)	355.2	355.6	354.7	355.9
Max	356.6	357.2	356.7	358.7
Min	354.1	353.2	352.6	354.3
Max-Min	2.5	4	4.2	4.4
Post Test Leakage (sccm)	43	23	39	46

Conclusion – There have been some challenges in the execution of the block metric tests, but root cause analysis is pointing to electrical short circuits as the cause of substrate damage at the start of tests during the original LGFCS procedure of in-situ reduction of the strips within the test rigs (as a result of manufacturing issues) or in the case of the Phase 1 test after some period of test time. Additional analyses of the stack design have been performed and solutions have been implemented to reduce the risk of short circuits. SECA Phase 1 and Phase 2 degradation targets have been met. LGFCS has established a strip pre-reduction procedure that qualifies strips for inclusion into block tests, insuring absence of any short circuits and confirming meeting OCV specifications; such an approach is planned for commercial scale production. LGFCS is focused on the impact of chromium contaminants on the degradation rate of its future product and the block test stands serve has the most representative test bed for finalizing a selection of block materials and cathode composition to minimize chromium induced degradation.

Task 6.0 - Manufacturing

Approach – A new task was added in Phase II to cover the manufacturing activities. This includes strip print, build and repairs for metric block tests. Also covered are manufacturing optimization studies to reduce the number of print/fire operation.

Results and Discussion –

Strip manufacturing:

- This task supported the completion of the epsilon strips that were assembled into the Phase I metric test.
- Five epsilon strips were fabricated for the Phase II metric block test.
- Four epsilon strips were fabricated for the Phase 2B metric block test

Print/Fire Process Reductions:

- Eliminated one print and one firing cycle for the cathode side layers
- Eliminated one firing cycle for the fuel-side active layers
- Firing cycle time was reduced to 14 hour cycle to allow morning printing of tubes following a late afternoon start of a firing cycle.

The reduced firing cycle time was an important advance to insure no lost printing days. The process reductions steps demonstrated have been subsequently adopted in the current LGFCS manufacture prototype line based on achieving similar ASR values for the processed substrates (Figure 95). LGFCS has identified additional printing and firing cycles that could ultimately be eliminated with further process development, and such an effort has become part of the LGFCS internal program.

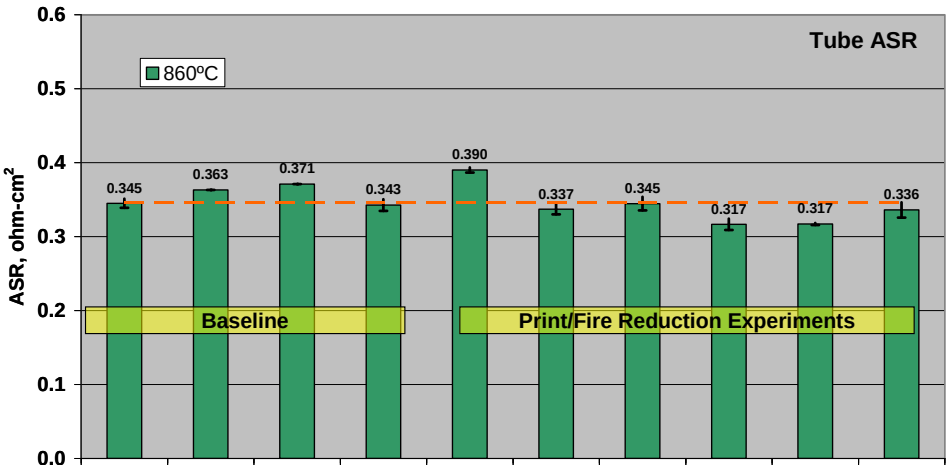

Figure 95. Similar substrate ASR with print/fire reduction processes

GRAPHICAL MATERIALS LIST

LIST OF ACRONYMS

ABT	Ambient Bundle Test
AC	Alternating Current
ACC	Anode Current Collector
ASR	Area Specific Resistance
ASTM	American Society for Testing and Materials
ATBT	Ambient Triple Bundle Test
ASU	Air Separation Unit
BOL	Beginning of Life
CCC	Cathode Current Collector
CFD	Computational Fluid Dynamics
CPOX	Catalytic Partial Oxidation
CRADA	Cooperative Research & Development Agreement
CRR	Constant Recycle Ratio
CTE	Coefficient of Thermal Expansion
CWRU	Case Western Reserve University
DC	Direct Current
DoE	Department of Energy
DOE	Department of Energy
DP	Differential Pressure
EDS	Energy Dispersive Spectroscopy
EELS	Electron Energy Loss Spectroscopy
EIS	Entry-Into-Service, Electrochemical Impedance Spectroscopy
FC	Fuel Cell
FCDM	Fundamental Differential Cell Model
FEA	Finite Element Analysis
FWP	Field Work Proposal
GC	Gas chromatography
GFI	Ground Fault Interruptor
HHV	Higher Heating Value
HMI	Human-Machine Interface
HX	Heat Exchanger
IGFC	Integrated Gasification and Fuel Cell
IGFCS	Integrated Gasification and Fuel Cell System
IP	Integrated Planar
LGFCS	LG Fuel Cell Systems
LSM	Lanthanum Strontium Manganese
LSCF	Lanthanum Strontium Cobalt Ferrite
MEIC	Mixed Electronic Ionic Conductor
MMA	Magnesia Magnesium Aluminate
MP	Mature Product
MOR	Modulus of Rupture
NASA	National Aeronautics & Space Administration
NETL	**National Energy Technology Laboratory**
NG	Natural Gas
NOC	Normal Operating Condition
OCV	Open Circuit Voltage
OGB	Off-Gas Burner
ORNL	Oak Ridge National Laboratory
PAB	Porous Anode Barrier

PBC	Pressurized Button Cell
PBT	Pressurized Bundle Cell
PCT	Penta-Cell test
PIC	Primary Interconnect
RC	Resistance-Capacitance
PMP	Project Management Plan
PNNL	Pacific Northwest National Laboratory
RRFCS	Rolls-Royce Fuel Cell Systems
RU	Repeat Unit
RUS	Resonant Ultrasound Spectroscopy
RTI	Research Triangle Institute
SBTS	Stack Block Test Stand
SCADA	Supervisory Control and Data Acquisition
SCG	Slow Crack Growth
ScSZ	Scandia stabilized Zirconia
SECA	Solid State Energy Conversion Alliance
SEM	Scanning Electron Microscope
SIC	Secondary Interconnect
SOFC	Solid Oxide Fuel Cell
TEM	Transmission Electron Microscope
TPB	Three Phase Boundary
TRT	Tube Run Test
TSF	Technology Scale Factor
UCONN	University of Connecticut
U_f	Fuel Cell Utilization
UK	United Kingdom
USC	University of South Carolina
VI	Voltage-current
Vop	Operating Voltage
XRD	X-ray Diffraction